Measurement of the Charge-Changing Cross Section of ^{120}Sn at Relativistic Energies

Messung des charge-changing Wirkungsquerschnitts von ^{120}Sn bei relativistischen Energien
Zur Erlangung des Grades eines Doktors der Naturwissenschaften (Dr. rer. nat.)
Genehmigte Dissertation von Ashton Marie Falduto aus Kenosha, United States of America
Tag der Einreichung: 11. April 2023, Tag der Prüfung: 17. Mai 2023

1. Gutachten: Prof. Dr. Thomas Aumann
2. Gutachten: Prof. Dr. Alexandre Obertelli
Darmstadt, Technische Universität Darmstadt – D17

TECHNISCHE UNIVERSITÄT DARMSTADT

Fachbereich Physik
Institut fuer Kernphysik
Experimentelle Kernstrukturphysik

Measurement of the Charge-Changing Cross Section of ^{120}Sn at Relativistic Energies
Messung des charge-changing Wirkungsquerschnitts von ^{120}Sn bei relativistischen Energien

Accepted doctoral thesis by Ashton Marie Falduto

Date of submission: 11. April 2023
Date of thesis defense: 17. Mai 2023

Darmstadt, Technische Universität Darmstadt – D17

Bitte zitieren Sie dieses Dokument als:
URN: urn:nbn:de:tuda-tuprints-273624
URL: http://tuprints.ulb.tu-darmstadt.de/27362
Jahr der Veröffentlichung auf TUprints: 2024

Dieses Dokument wird bereitgestellt von tuprints,
E-Publishing-Service der TU Darmstadt
http://tuprints.ulb.tu-darmstadt.de
tuprints@ulb.tu-darmstadt.de

Abstract

The knowledge of the equation of state (EOS) for neutron-rich matter is fundamental for understanding properties of, *e.g.*, neutron stars, core-collapse supernova, and neutron-rich nuclei. Deriving experimental constraints for the EOS is thus of utmost importance. The parameter for the slope of the symmetry energy at saturation density (L), in the EOS for asymmetric nuclear matter has not yet been sufficiently constrained experimentally. One variable that has been proven to be highly sensitive to L is the neutron-skin thickness, which is the difference between the nuclear root-mean-square (rms) obtained using the density distributions of neutrons and protons in a nucleus. It has been shown that through an accurate measurement of the total neutron-removal cross section, the value of L can be constrained.

The R3B setup has been upgraded to now include the neutron detector NeuLAND and the GLAD dipole magnet alongside our tracking setup, which will allow measurements with high momentum resolution and large acceptance. This will allow us to get the accuracy required for constraining L. With this setup, accurate measurements of the total reaction, charge-changing, and neutron-removal cross sections are possible. A first measurement for ^{120}Sn has already been completed using the FAIR phase 0 R^{3}B setup at GSI and will be presented here. First results for the charge-changing cross section are also presented along with an outlook for future experiments.

Zusammenfassung

Die Kenntnis der nuklearen Zustandsgleichung für neutronenreiche Materie ist grundlegend für das Verständnis der Eigenschaften von Neutronensternen, Kernkollaps-Supernovae, neutronenreichen Atomkernen und vielen weiteren Bereichen der Physik. Die Einschränkung der nuklearen Zustandsgleichung durch experimentelle Daten ist daher von besonderer Wichtigkeit. Insbesondere der Steigungsparameter L der Symmetrie-Energie bei Sättigungsdichte ist bislang experimentell nur sehr schwach eingegrenzt. Eine sehr bedeutende experimentell zugängliche Größe ist die Neutronenhautdicke von Kernen, da diese stark mit L korreliert ist. Sie wird beschrieben durch die Differenz der quadratischen Mittel der Dichteverteilungen von Neutronen und Protonen im Kern. Es konnte gezeigt werden, dass präzise Messungen von totalen Neutronenseparationswirkungsquerschnitten gut geeignet sind um den Wert des Parameters L weiter einzugrenzen.

Der experimentelle Aufbau R3B wurde aufgerüstet und beinhaltet neben den vorhandenen Komponenten zur Rekonstruktion von Teilchenbahnen nun den Neutronendetektor NeuLAND und den Dipolmagneten GLAD, was Experimente mit hoher Impulsauflösung bei gleichzeitig hoher Akzeptanz möglich macht. Hierdurch wird die nötige Genauigkeit erreicht um die Einschränkung des L-Parameters zu erlauben. Mit diesem Aufbau können nun Messungen von totalen sowie Landungsänderungs- und Neutronenseparationswirkungsquerschnitten durchgeführt werden. In dieser Arbeit wird eine solche Messung für Zinn-120 vorgestellt, welche mit dem FAIR Phase 0 R3B Aufbau durchgeführt wurde. Es werden erste Ergebnisse für den Ladungsänderungswirkungsquerschnitt präsentiert und ein Ausblick auf zukünftige Experimente aufgezeigt.

Contents

1. Introduction

As of late, understanding the properties of core-collapse supernovae, neutron stars, and neutron star mergers has been a big discussion for nuclear physics [LP04; Web05]. Neutron stars (NS) are of great interest because NS-NS mergers are amongst the leading theories for the location of the formation of nuclei heavier than iron, especially neutron-rich nuclei. They are most usually created through the core collapse supernova explosion of a giant star [OS21]. The core of the star will collapse once energy production ends after the core has burnt completely to iron. Protons and electrons will be pushed tighter together and form neutrons and neutrinos. This process is mediated by the weak force and can be written as:

$$p + e^{-} \rightarrow n + \nu_e. \tag{1.1}$$

Neutrinos are able to easily escape the contracting core, but the neutrons will collect closer together until their overall density is equivalent to an atomic nucleus. A typical neutron star will have a mass of 1.4 solar masses and a radius of 10 km. A schematic of a neutron star can be seen in Fig. 1.1. The outer crust is a sea of electrons at low densities and nuclei, the inner crust to outer core becomes increasingly more neutron rich, and the inner core is supranuclear densities of neutrons where the particles are squeezed together more tightly than atomic nuclei. It is generally accepted that the mass of neutron stars are comprised of about 95% neutrons and 5% protons and electrons [Wat+16].

In order to understand these phenomena, an Equation of State (EoS) for neutron-rich matter is needed [Lat12; HPY07; Heb+13]. The EoS parameterizes the energy in infinite nuclear matter as a function of its density, and is constrained on the basis of astrophysical observations and properties of atomic nuclei. A quantity that turns out to be highly sensitive to the asymmetry of the EoS is the neutron skin thickness. The neutron skin thickness is defined as the difference between the nuclear root-mean-square (rms) obtained using the density distributions of neutrons and protons in the nucleus [TD19]. An outer layer of neutrons will form on the surface of neutron-rich nuclei and will be described in more detail in Sec. 1.3.1. Therefore, it is essential to study the properties of nuclei

away from the valley of stability to have a full picture of astrophysical processes as asymmetrical matter has not been as extensively investigated as symmetrical matter.

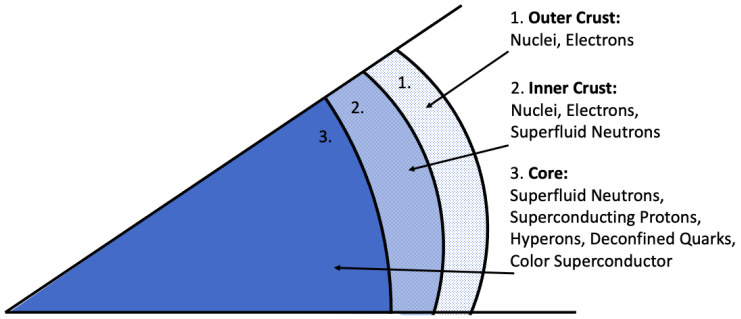

Figure 1.1.: Structure of a neutron star shown schematically. The outer crust (1.) of the neutron star is mostly loose nuclei and electrons. The inner crust (2.) begins to become more neutron dense as they leak out of ions at densities of about $4 \cdot 10^{11}\,\mathrm{g/cm^3}$, which is also where neutron degeneracy starts to play a role. At the core (3.), the densities are around $2 \cdot 10^{14}\,\mathrm{g/cm^3}$, and the nuclei will dissolve completely. Here, the densities reach several times the saturation density [Wat+16].

1.1. Fundamentals of Nuclear Structure

Depending on the number of protons and neutrons in an atomic nucleus, nuclei will either be stable or unstable. Stable nuclei have infinite lifetimes, and therefore do not spontaneously undergo radioactive decay. Of the over 3,000 currently known isotopes, only about 300 are stable. Some numbers of protons and neutrons yield particularly stable nuclei, which are referred to as magic nuclei [HJS49; May49]. The experimentally observed magic numbers are 2, 8, 20, 28, 50, 82, and 126. Isotopes can either be singly-magic or doubly-magic, depending on if one or both the protons or neutrons are a magic number. Atomic theory using a shell model provided great insight into the complicated detail of atomic structure. Therefore, nuclear physicists created the nuclear shell model as a way to solve the problem of nuclear structure in hopes of similar success clarifying the properties of nuclei [KH88]. This model uses the Pauli exclusion principle to explain how protons and neutrons populate energy levels in a spherical harmonic potential. It breaks the nucleus down into orbits and shells, and these magic numbers occur when either a shell for protons or neutrons have been completely filled. Nuclei with a filled shell have a larger gap in energy to the next shell, and are therefore particularly stable. The order of filling the first shells can be seen in Fig. 1.2.

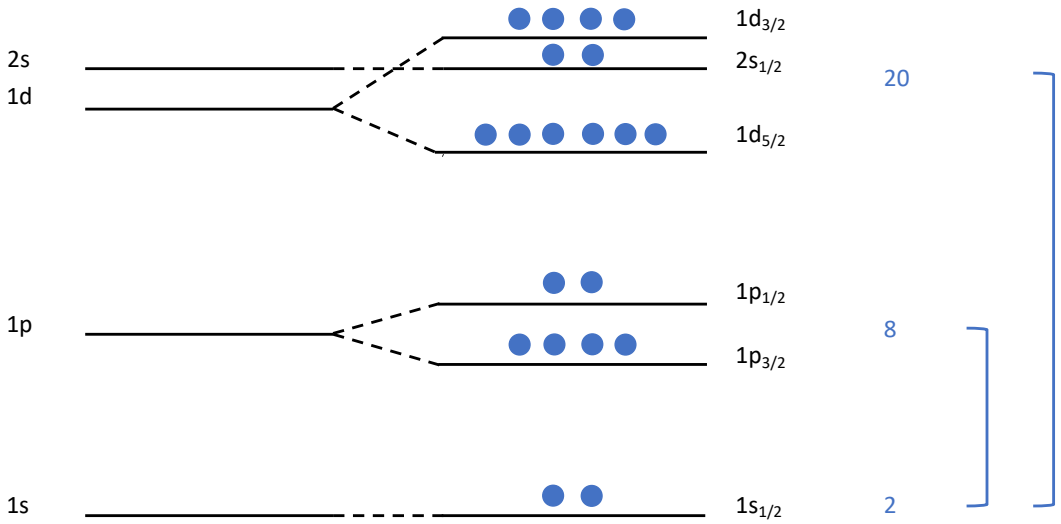

Figure 1.2.: The first three major shells of the nuclear shell model. On the left side, no spin-orbit interaction is used for the energy level and on the right side, the energy levels are broken down into sub-shells based on the spin-orbit interaction. The number to the right of an energy level is the degeneracy. The magic numbers are reproduced as each major shell is filled.

Using nuclei with either proton or neutron magic numbers can be of great experimental value. Oxygen with a proton number of Z=8 is studied in great detail near the neutron drip line. The neutron drip line is the neutron edge of the chart of nuclides [NND], and is the maximum number of neutrons an element can have bound. This edge can be seen in Fig. 1.3. Calcium is the next element with a proton magic number at 20. It is studied with particular interest because it has the doubly magic Z=20 and neutron number N=20, which is also the highest mass Z=N stable isotope. Calcium also has the neutron-rich doubly magic Z=20 and N=28, and although ^{48}Ca is not technically stable, it is extremely long lived and naturally occurring. The heaviest stable doubly magic isotope is ^{208}Pb, which is neutron-rich and stable, making it very useful in experiments. The element with the highest number of stable isotopes, magic or otherwise, is tin (Z=50). Tin has ten stable isotopes; ^{112}Sn, $^{114\text{-}120}$Sn, ^{122}Sn, and ^{124}Sn. ^{126}Sn is not stable, but has a long lifetime of about 10^5 years. It also has two doubly magic isotopes; ^{100}Sn on the neutron-deficient side, and ^{132}Sn on the neutron-rich side. All isotopes of tin between ^{100}Sn and ^{132}Sn have been observed experimentally. The diversity of these different tin isotopes allows for a unique environment to study nuclear structure.

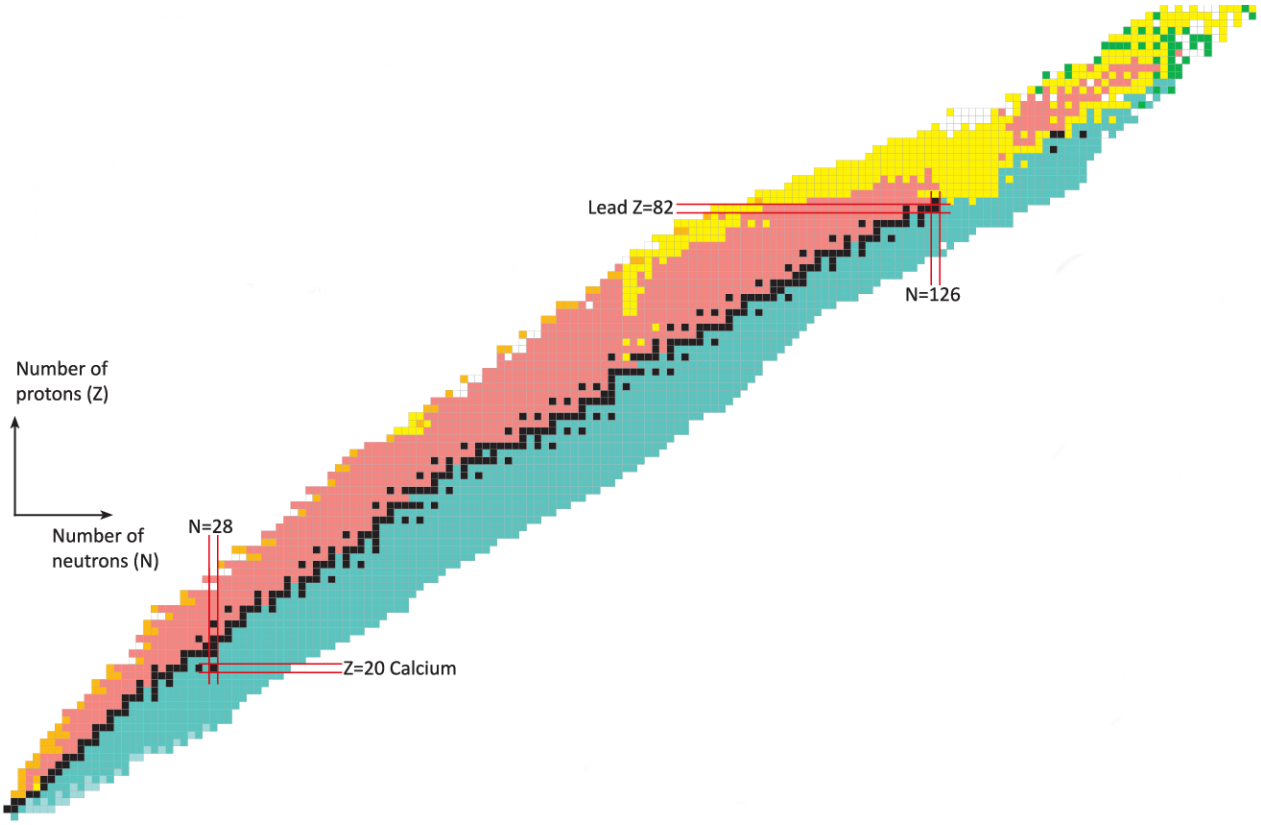

Figure 1.3.: Chart of nuclides. All isotopes that have been discovered as of 2018. Neutron number is on the x-axis and proton number is on the y-axis. Some magic numbers are highlighted by the red boxes. The colors indicate the type of decay the isotope undergoes: pink squares by β^+, turquoise squares by β^-, and yellow squares by α to name a few. Black squares represent stable isotopes. As an element with a given Z acquires or removes neutrons, it approaches either the proton or neutron drip line, which is the limit for how few or many neutrons are required to keep the nuclei bound. Image is from [SMD19].

For stable light nuclei, there tends to be an equal number of protons and neutrons in the nuclei. As nuclei become heavier, more neutrons than protons are needed for the nuclei to be stable. This is due to the fact that as more protons are added, the repulsive force from the Coulomb interaction becomes stronger. Adding in neutrons, since they do not repel each other nor do they need to overcome the Coulomb interaction, allows the nucleus to become larger and allows the protons more space. As more neutrons are added to these stable nuclei, different structural effects will begin to appear. In Fig. 1.4, it can be seen as nuclei become asymmetric with a slightly higher neutron-to-proton ratio, they begin to form a layer of neutrons on the surface called the neutron skin [Tan+92]. If even more neutrons are added, and nuclei get closer to the neutron drip line and are less tightly bound, nuclei can form a neutron halo in specific cases in light nuclei [HJ87].

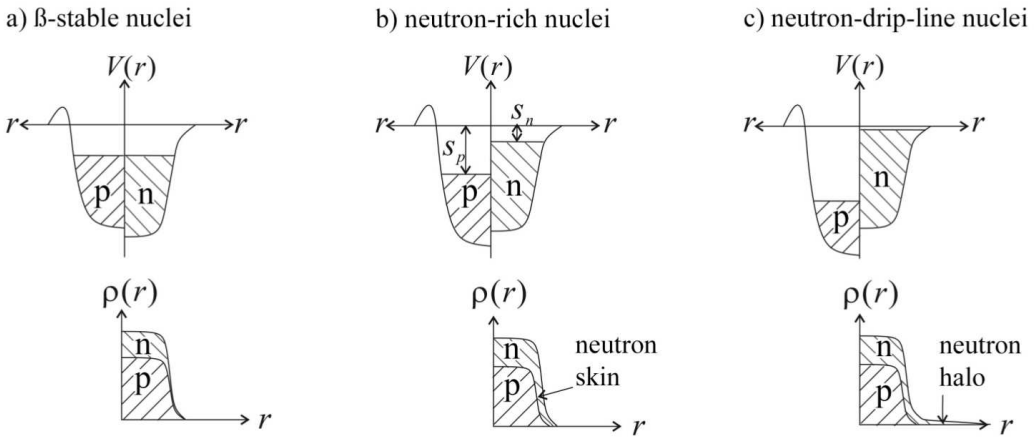

Figure 1.4.: TOP: The change of the mean field potential and BOTTOM: density profiles from nuclei that are β stable (a) to neutron-rich nuclei (b) and to very neutron-rich nuclei near the neutron is drip line (c) is shown. The upper panel shows how changing the ratio of protons and neutrons can create a significant difference of Fermi energies between protons and neutrons. This difference causes the formation of a thick neutron skin seen in (b), and when the one neutron separation energy nears zero, a neutron halo structure is created due to the effect of quantum tunneling (c). Image is taken from [AN13]

1.2. The Nuclear Equation of State

The work below is derived from [Sch17; Hor19; OS21]. An Equation of State (EoS) is a thermodynamic equation which relates state variables under a given set of physical conditions. There are different approaches to try to understand the nuclear EOS. In recent years, progress has been made in one method using Chiral Effective Field Theory (ChEFT) at the TU Darmstadt nuclear physics theory department [HS10]. ChEFT is a systematic approach for understanding the interactions between nucleons. Using the symmetries of quantum chromodynamics (QCD), ChEFT allows for the systematic expansion of nuclear forces at low energies and the extraction of systematic uncertainties for observables [Gre+20]. However, ChEFT has intrinsic breakdown scales that are still being established and using many-body interactions when computing. It is generally geared towards lighter nuclei, although recently chiral low-resolution interactions that can describe up to ^{208}Pb have been developed [AHS24]. More information on ChEFT and nuclear forces can be found in [ME11].

The approach described below for the nuclear EOS comes from the relativistic mean-field theory, which is able to describe the ground state properties of nuclei across the entire periodic table. Since the mean-field theory breaks many-body problems down into an effective one-body problem, there is considerably less computational cost needed. The important variables to describe nuclear matter

in the nuclear EoS are the density of the atomic nucleus known as the nuclear density, pressure, and temperature. The nuclear EoS marks the energy per nucleon in nuclear matter and is commonly written in the Taylor expansion of $E(\rho, \delta)$ around δ at $\delta = 0$

$$E(\rho, \delta) = E(\rho, 0) + \frac{1}{2}\frac{\partial^2 E(\rho, \delta)}{\partial \delta^2}\bigg|_{\delta=0} \delta^2 + \mathcal{O}(\delta^4) \tag{1.2}$$

where E(ρ,0) is the energy per nucleon in symmetric matter at δ=0 and δ is the relative neutron-proton asymmetry

$$\delta = \frac{N - Z}{A}. \tag{1.3}$$

However, if protons and neutrons are assumed to have equal mass, then terms of odd order vanish due to isospin invariance and Eq. 1.2 can be written as

$$E(\rho, \delta) = E(\rho, 0) + S(\rho)\delta^2 + \mathcal{O}(\delta^4), \tag{1.4}$$

where the first term $E(\rho, 0)$ corresponds to the EoS for symmetric matter and the second term $S(\rho)$ is defined as

$$S(\rho) = \frac{1}{2}\frac{\partial^2 E(\rho, \delta)}{\partial \delta^2}\bigg|_{\delta=0} \tag{1.5}$$

and is referred to as the symmetry energy and contains all the isospin dependence. In Fig. 1.5, the difference between symmetrical matter and pure neutron matter can be seen at saturation density ρ_0 and random density ρ'. The density-shift parameter is defined as

$$\epsilon = \frac{\rho - \rho_0}{3\rho_0} \tag{1.6}$$

where ρ_0 is the density at saturation energy. Then, the EoS of symmetric matter can be rewritten as

$$E(\rho, 0) \approx E(\rho, 0) + \frac{1}{2}K_0\epsilon^2 \tag{1.7}$$

where K_0 is the incompressibility of symmetric matter and is defined as

$$K_0 = 9\rho_0^2\frac{\partial^2 E(\rho, 0)}{\partial \rho_0^2}\bigg|_{\rho=\rho_0} \tag{1.8}$$

Expanding the symmetry energy to

$$S(\rho) \approx J + L\epsilon + \frac{1}{2}K_{\text{sym}}\epsilon^2, \tag{1.9}$$

Eq. 1.4 can be rewritten as

$$E(\rho,\delta) \approx E(\rho,0) + \frac{1}{2}K_0\epsilon^2 + (J + L\epsilon + \frac{1}{2}K_{\text{sym}}\epsilon^2)\delta^2 \tag{1.10}$$

with the parameters defined as

$$J = S(\rho_0) \tag{1.11}$$

$$L = 3\rho_0 \frac{\partial S(\rho)}{\partial \rho}\bigg|_{\rho=\rho_0} \tag{1.12}$$

$$K_{\text{sym}} = 9\rho_0^2 \frac{\partial^2 S(\rho)}{\partial \rho^2}\bigg|_{\rho=\rho_0} \tag{1.13}$$

The parameters in the asymmetrical part of the EoS are J, which is the symmetry energy at saturation density, L, which is the slope of the symmetry energy at saturation density, and K_{sym}, which is the incompressibility (or curvature) of the symmetry energy at saturation density.

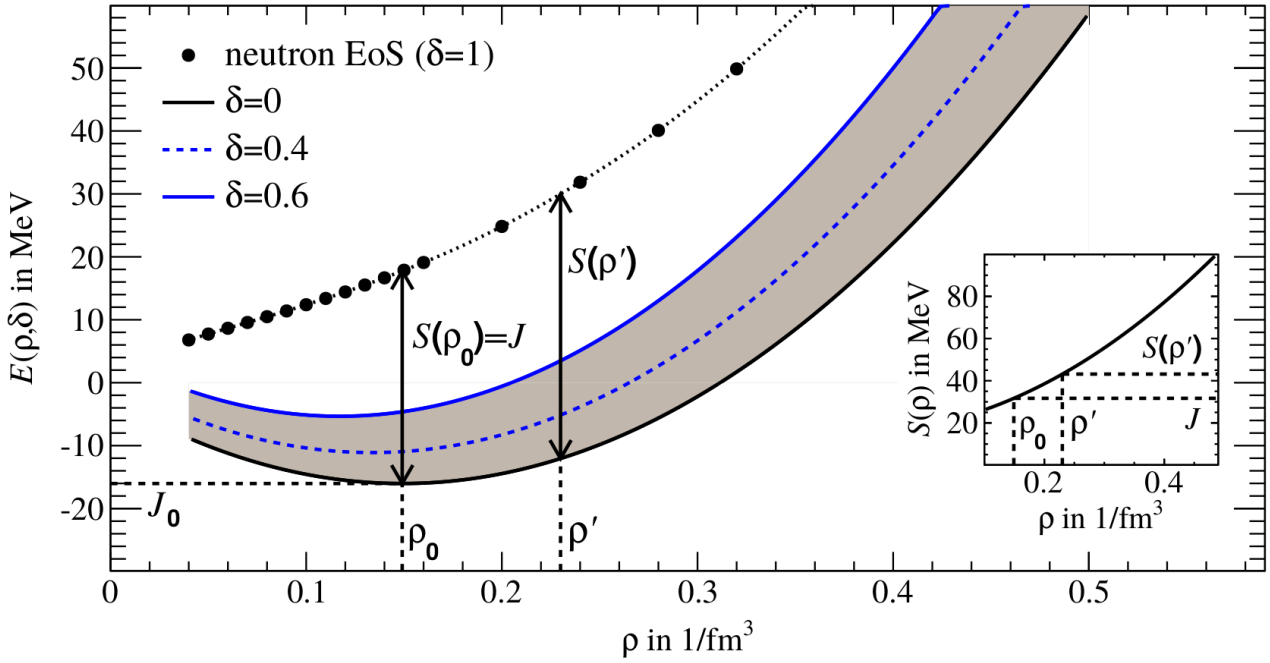

Figure 1.5.: The EoS of nuclear matter as a function of the density, ρ. Black points are the neutron EoS (δ=1) as found in [Gan+14]. The solid curves come from different asymmetry parameters δ for the nuclear EoS based on the relativistic mean-field model DD2 [Typ+10]. The gray band shows the difference between δ=0 and $\delta = 0.6$ with the additional example of δ=0.4 depicted as the clue dashed line. The corresponding symmetry energy $S(\rho)$ is shown. Imagine comes from [Sch17].

The symmetry energy at saturation density, J, between 30 and 35 MeV is fairly well constrained experimentally [Tsa+12; Lat12]. However, the slope at saturation density, L, is poorly constrained experimentally, as can be seen in Fig. 1.6. At saturation density, the different Skyrme interactions, which will be covered in more detail in the following section, all converge at roughly J=30 MeV. However, at the saturation density, the slopes become very different. There are many experimental methods working to constrain the L parameter as it is highly sensitive to the parametrization of the nuclear interaction model and can provide insights into the EoS. Two observables that can potentially provide constraints on L are the dipole polarizabilty and the neutron skin thickness [Aum+17]. The following sections will explain these observables in more detail and the experiments being carried out to measure them.

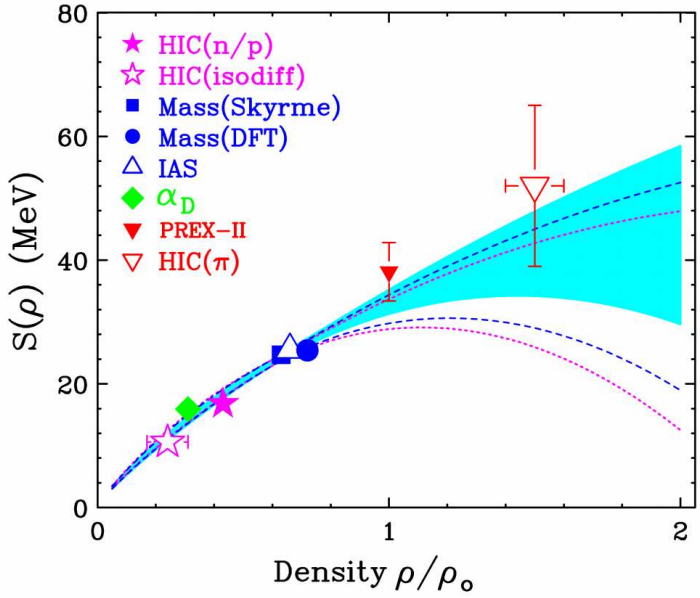

Figure 1.6.: Density dependence of the symmetry energy. The area shaded in cyan shows the 1σ contour from fitting S(ρ). The dotted curves represent the upper and lower bounds of the fits without PREX2 and pion results, while the dashed curves include PREX2 but no pion results. Image is taken from [LT22].

1.3. Theoretical Approaches

Nuclear structure can be explained through many different theoretical approaches. An overview to these approaches can be found in [BHR03] and [SH15]. While medium-mass and heavy nuclei can technically be computed with *ab initio* methods, most interactions developed considerably overbind nuclei [Bin+14]. The models focused on here are many-body models, such as the nuclear shell model or mean-field models, that are based on effective nuclear interactions and adjusted to reproduce the

properties of finite nuclei. The nuclear shell model is most appropriate for light and medium mass nuclei, while the mean-field models are used across the chart of nuclides and make use of Energy Density Functionals (EDF). Both approaches come directly from the outcome of nucleon-nucleon interactions [OS21]. These approaches are phenomenological and pragmatic; the functional forms of the Hamiltonian with spin and isospin degree of freedom are selected and determine parameters under constraints from experimental data. The parameters can be, but are not limited to, the binding energy of nuclear matter, the RMS radii, or quantities extracted from data such as symmetry energy.

Typical variants used for EDF are Gogny forces [DG80] and Skryme functionals [VB72], which are Hartree-Fock models, or relativistic mean-field models [Wal75]. Gogny forces are not addressed in this work and therefore not further discussed. Skyrme functionals are an an effective interaction with two-body or three-body forces; and they either start from parameterization of a potential from which the energy-density will be derived, or they directly parameterize the energy-density functional without needing to link to the two-body force. Over the years, many Skyrme functionals with additional terms to the parameterization have been published that allow for adjustments for interactions. However, it is noted that most Skyrme interactions do not pair correlations properly in nuclei, so an additional pairing interaction is added in the Hartree-Fock-Bogolyubov calculations. A more in-depth description of Skyrme functionals can be found in [SR07]. Relativistic mean-field models include the nucleonic and mesonic degrees of freedom in a relativistic formalism [Dut+14]. The coupling constants of the mesons with nucleons are treated as free parameters that can be adjusted to produce empirical saturation properties of nuclear matter, particularly at the nuclear saturation point. More information on relativistic mean-field theory can be found in [Rei89; TW99]. The best way to test these models is through experimental observations. One quantity that is particularly sensitive to the density dependence of the EoS is the neutron-skin thickness, which will be described in more detail in the following section.

1.3.1. Neutron Skin

The neutron skin thickness is one quantity that has been noted to be very sensitive to density dependence in the nuclear EoS. Neutron skin is defined as the outer layer of neutrons that forms on neutron-rich nuclei. The neutron skin is characterized by its thickness, which is defined by the difference between the neutron and proton root mean square (RMS) radius:

$$\Delta r_{np} = \langle r_n^2 \rangle^{1/2} - \langle r_p^2 \rangle^{1/2} \tag{1.14}$$

It was first noted by Brown [Bro00] that there is a linear correlation between the derivative of the EoS and the neutron skin thickness through the use of many Skyrme Hartree-Fock models, and then later again by Typel [TB01] for relativistic models. The strong correlation can be seen in Fig. 1.7.

Roca-Maza [Roc+11] theorized that parity-violating electron scattering (PVES) could be used as a means to determine neutron skin thickness. The correlation between L and Δr_{np} for nonrelativistic and relativistic models can be seen in Fig. 1.8. This and the other methods that have been used to probe the measurements of the observables that are directly sensitive to the symmetry energy will be discussed in the following sections.

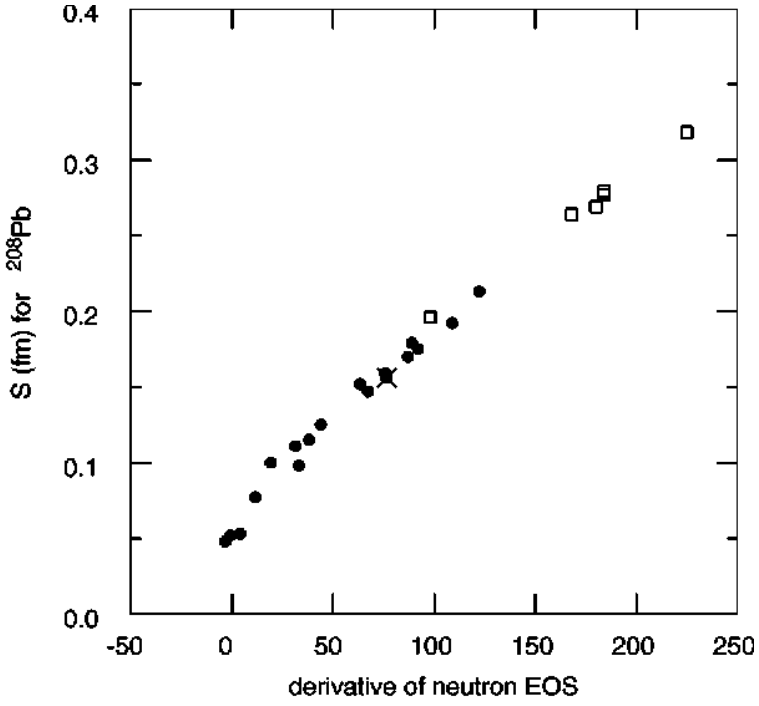

Figure 1.7.: The derivative of the EoS at ρ_0=0.10 neutrons/fm^3 vs the S value in ^{208}Pb for 18 different Skyrme parameter sets (with filled circles) and for 6 relativistic models (with squares). A strong correlation can clearly be seen. Image is taken from [TB01].

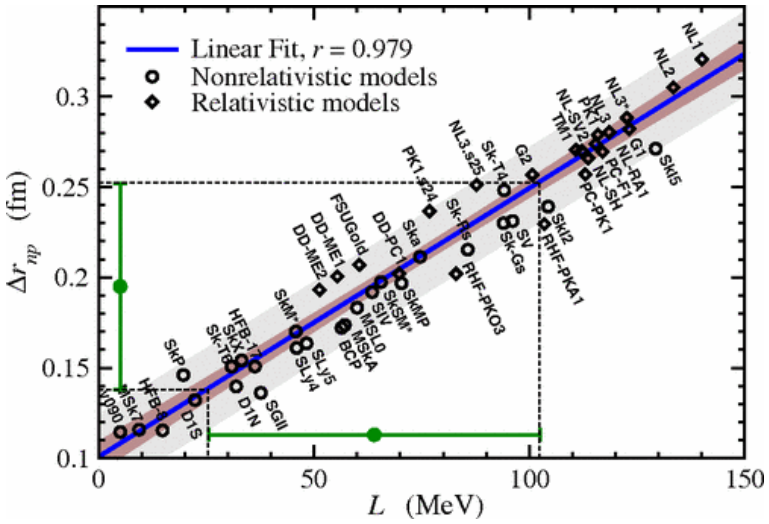

Figure 1.8.: Shows the correlation between the neutron skin of ^{208}Pb and L. The circles and diamonds are different nuclear energy density functionals; circles are non-relativistic and diamonds are relativistic. The linear fit is $\Delta r_{np} = 0.101 + 0.00147L$. Image is taken from [Roc+11].

1.4. Experimental Methods to Constrain L

1.4.1. Charge and Matter Radii

The charge radius, $\langle r_p^2 \rangle^{1/2}$, is the measurement of the proton distribution in a nucleus, while the matter radius is the measurement the neutron RMS radius, $\langle r_n^2 \rangle^{1/2}$. Charge distribution has been extensively studied through electron elastic scattering. So far, this method is only limited to studying stable nuclei and is not easily applied to radioactive nuclei. Electron scattering is one of the objective probes to study hadronic structure [DDD87]. This is because the electromagnetic forces are well known and relatively weak compared to the forces responsible for the structure. Laser spectroscopy is also a well established method to study the charge radii [AM13]. Precise measurements of the atomic isotopic shift allow the extraction of the change in the nuclear charge radius from one isotope to another. For multi-electron systems, this technique only allows for relative measurements, which typically are referenced to a well-known stable charge radius determined with electron scattering or muonic atoms.

Another method which is currently used to constrain L is mirror nuclei using the differences in their charge radii. The differences in the charge radii of mirror nuclei are shown to be proportional to the derivative of the neutron equation of state and the symmetry energy at nuclear matter saturation density [Bro17]. Mirror nuclei are two nuclei with opposite proton and neutron numbers, such as

^{54}Ni and ^{54}Fe. This is particularly helpful if the target nuclei is unstable, but the mirror nuclei is not. With the assumption of perfect charge symmetry, the neutron RMS radius will be equal to the proton RMS radii in its mirrored nucleus, which can then be used to determine the neutron skin thickness. The charge symmetry is distorted by the Coulomb interaction, which can be calculated. The uncertainty can fortunately be calculated and is found to be of a magnitude smaller than the Coulomb effects, and therefore negligible [Bro17].

Using 48 Skyrme functionals, Brown was able to show a strong correlation between the neutron skin thickness of neutron-rich nuclei and L from mirror nuclei [Bro17]. It was found that when using ^{56}Ni $(N = Z)$, the neutron skin is not determined by L, but it is actually correlated to the symmetry energy at a density of 0.10 nucleons/fm^3. The charge radius is correlated with $|N - Z| \times L$ and the neutron skin depends on both $|N - Z| \times L$ and the symmetry energy. As $|N - Z|$ becomes larger and nuclei become more neutron rich, the conclusion is that the L dependence dominates the neutron skin. A recent experiment at The National Superconducting Cyclotron Laboratory (NSCL) at Michigan State University applied the mirror charge radii formalism to ^{54}Ni and ^{54}Fe [Pin+21]. The results found a correlation between the charge radii and L, with a range of $L = 20 - 70$ MeV. This was consistent with L from the gravitational wave GW170817 [Abb+17] and a previous experiment using ^{36}Ca and ^{36}S and suggests a "soft" EoS, which has smaller pressures, is easily compressed, and produces stars of smaller radii [KSF97]. However, this result is inconsistent with the PREX-2 experiment, which will be introduced in more detail in the following. PREX-2 had indicated a "stiff" EoS, which has larger pressures, cannot be compressed, and predicts neutron stars with larger radii. More experiments with mirror nuclei in different mass regions would allow a tighter limit on L.

While determining a charge radius has a few established methods, determining the matter radius is an even more challenging task. The following methods described relate only to measurements conducted using stable nuclei. One method to measure the matter radii is proton elastic scattering (p,p). Proton elastic scattering is advantageous because it can be applied to stable nuclei and also short-lived nuclei in inverse kinematics. This method is able to reach uncertainties as low as 0.1 fm, which- beyond statistical limitations- come mostly from the interaction potential [OS21]. If the elastic scattering data is combined with measurements of the charge distribution of the nucleus, it can be used to determine the neutron distribution, and also the neutron skin thickness in neutron-rich nuclei. Some experiments that using ^{208}Pb are [Bat+89; CKH03; Zen+09] and can be referred to for more information.

An experimental campaign conducted at Thomas Jefferson National Accelerator Facility (JLab) sought to measure the neutron radius using ^{208}Pb from parity-violation asymmetry measurements of electron elastic scattering. Electromagnetism conserves parity, so any non-zero value for the parity violating asymmetry must be coming from weak interaction through the exchange of the Z boson [SP16]. The advantage of using PVES is that quarks will have different charges when interacting with the Z boson instead of photons. The weak charge of the neutron is much larger than

the weak charge of the proton for the Z boson, making PVES much more sensitive to the neutron distribution. The first Pb Radius Experiment (PREX) in 2011 found the difference between neutron and proton distributions $R_n - R_p = 0.33^{+0.16}_{-0.16}$ fm [Abr+12]. This experimental campaign suffered from low statistics, so a second experiment, PREX-2, was carried out recently [Sou+11] and found $R_n - R_p = 0.283^{+0.071}_{-0.071}$ fm [Ree+21]. The follow up experiment also included a measurement for the neutron skin thickness of ^{48}Ca, CREX [Mam+]. This experiment has also run, but does not have published data yet.

1.4.2. Electric Dipole Polarizability

The EoS parameters can also be investigated by looking at the response of a nucleus to an electric field. Essentially, protons and neutrons can be displaced in the nucleus due to the introduction of an electric field, which is balanced by the symmetry energy acting as a restoring force. The interaction of nuclei with an electric field leads to the population of nuclear excited states, many of which contribute to the Giant Dipole Resonance (GDR) in nuclei [TCV08]. The isovector giant dipole resonance (IVGDR) is the collective nuclear mode defined as out of phase motion of protons and neutrons that causes an isospin imbalance. The changes in the isospin symmetry are described by the symmetry energy. The symmetry energy contributes to the restoring force for the vibration, and therefore strongly influences the excitation energies that can be easily excited by an electric field [LS82]. When an electric field is applied, a dipole moment is induced in the nucleus, and chance of this effect is described by the dipole polarizability α_D:

$$\vec{p} = \alpha_D \vec{E}. \tag{1.15}$$

The dipole polarizability shows promise to constrain L as it is an inversely weighted sum of the transition strength and is very sensitive to low-lying E1 strength,

$$\alpha_D = \frac{\hbar c}{2\pi^2} \int_0^\infty \frac{\sigma(E)}{E^2} dE. \tag{1.16}$$

In neutron rich nuclei, an enhancement to the α_D is expected due to the existence of a neutron skin. It is then possible for the vibrations of the neutron skin to occur against the isospin-symmetric core. Low energy states that are easily excited by electric dipole radiation then appear. These low energy states can contribute as much as 25% of the dipole polarizability [Tsa+12]. This smaller peak appears below the GDR energy and is referred to as the Pygmy Dipole Response (PDR) [Aum19].

The strong correlation between dipole polarizability and the neutron skin thickness can be seen in Fig. 1.9.

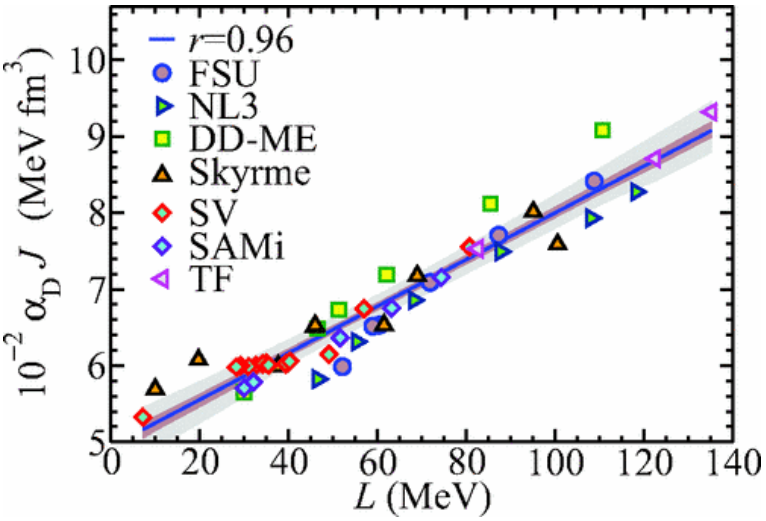

Figure 1.9.: The slope of the symmetry energy at saturation density, L, versus α_D for ^{208}Pb predicted by different energy density functionals. The dipole polarizability is multiplied by the symmetry energy at saturation density, J, and a clear correlation between the two observables can be seen. Image is taken from [Roc+13].

There have been many experimental attempts to study the dipole response. Real-photon absorption and scattering experiments can be done using stable nuclei, but difficult with short-lived nuclei. An alternative for short-lived nuclei is heavy-ion induced electromagnetic excitation at relativistic beam energies, also known as virtual-photon scattering. The projectile passes through a Lorentz contracted field of a high-Z target, causing an excitation that can be described as a virtual photon absorption. This process is able to reach excitation energies up to around 20 MeV and covers the GDR region, which lies around 15 MeV [BB88]. Some other experimental methods used to extract the dipole polarizability are using polarized proton inelastic scattering (p,p') at very forward angles [Tam+11] and excitation of the GDR via inelastic α scattering (α, $\alpha'\gamma$) [Kra94].

The IVGDR is not measured directly by experiments, but rather by the cross section distribution over the excitation energy range it was derived from, called Coulomb excitation. Coulomb excitation experiments are ideal because they can be done in inverse kinematics, i.e. an exotic beam with a stable target. This allows for the study of less stable, more neutron-rich nuclei. Coulomb excitation experiments conducted at the R^{3}B setup at GSI[1] resulted in the first measurement of the dipole response for ^{130}Sn and ^{132}Sn. This measurement covered the GDR energy region as well as the PDR and was able to deduce neutron-skin thicknesses. More information can be found in [Adr+05; Kli+07]. The first measurement of the dipole polarizability for an unstable, neutron-rich nucleus, ^{68}Ni was completed at GSI by Rossi et al [Ros+13]. More recently, a Coulomb dissociation measurement along the Sn isotopic chain ($^{124\text{-}134}$Sn) was also completed at GSI. Using the input from EDFs in the

[1]The R^{3}B setup at GSI will be introduced in Ch. 3.

form of B(E1) values to calculate the integrated Coulomb excitation cross sections (σ_C) and α_D, it was found that a good correlation exists between σ_C and α_D at high beam energies. Therefore, σ_C is a good probe for the symmetry energy parameters while being easier to experimentally determine than α_D. The most precise result came from ^{132}Sn for L=62 MeV as an upper limit for the symmetry energy [Hor19].

1.4.3. Total Reaction Cross Sections

Another method to measure the size of nuclei is through the total reaction cross section. One very important discovery that came from this method was the discovery of the halo nuclei [Tan+92]. Over the years, this method has been used numerous times. A list of previously measured interaction and reaction cross sections, along with the extracted matter radii, before 2001 can be found in [Oza+01]. The experimental campaign from the previous section also measured nuclear reactions along the Sn isotopic chain. The analysis of this data was done by F. Schindler and presented in her thesis [Sch17]. The work presented in this thesis is a continuation of that work, but with an experiment done using the tin isotope ^{120}Sn. Total reaction cross sections, which can be broken down into the sum of charge-changing and neutron-removal cross sections, was the preferred method due to many advantages. For the theoretical input, only the density and the parameters from the Glauber Theory, which will be explained more below and in the following chapter, are needed. For the experiment, GSI is uniquely equipped to handle the necessary beam energies and setup required to preform this measurement, which is described in more detail in Ch. 3. The method itself is also extremely robust. The analysis uses the transmission method; it is only looking for surviving particles. The charge-changing cross section is advantageous to study because charge-radii are very well known. This gives a reliable, quantitative input for the Glauber model to test with known quantities. The correlation from the results can be used to determine if theory explains the measured values. This will be discussed more in Sec. 5.4.1.

While this experiment is very similar to the previous, there are some key differences along with the changed isotope. The original experiment had a trigger scheme focused on detecting GDR events, while the main focus of this experiment was measuring the reaction cross section. To not lose statistics, this time the trigger scheme did not downscale the unreacted beam particles, as this is needed for accurate calculations. The setup also had many advancements in the years between the experiments. One large update was the first use of of the new large acceptance spectrometer GLAD. GLAD has a maximum bending angle of 40°which ensures an acceptance of nearly 100%. More information on GLAD can be found in Sec. 3.2. The detectors in the setup were also upgraded with newer models, such as the Position Sensitive Pin Diode silicon, fiber, and Time of Flight detectors. More information on all detectors can be found in Sec. 3.3. Another advancement was made in neutron detection. A new neutron detector NeuLAND was used in this campaign, which had 8

double planes at the time. NeuLAND is not relevant to the work presented in this thesis, but is important to the experiment as a whole. The Glauber Model does not take the collective excitation into account. For accurate measurements, this part must be subtracted from the neutron removal cross section, which is described below. The larger acceptance of NeuLAND allows for a more precise measurement. More information can be found on NeuLAND in Sec. 3.3.6. With the advancements of of the setup, it is possible to measure more precise cross sections than the previous experiment.

The interaction cross section is calculated from the nuclear interaction of a beam particle and a target nucleus. The cross section is the probability that a reaction between the beam and target will occur and can give insights to nuclear quantities such as the matter radii-, and indirectly, the neutron skin. To get to the total reaction cross section, the inelastic cross section also needs to be taken into account:

$$\sigma_R = \sigma_I + \sigma_{\text{inel}} \tag{1.17}$$

where σ_R is the total reaction cross section, σ_I is the interaction cross section, and σ_{inel} is the inelastic cross section, which means any reaction that does not involve a change in neutron or proton number. When the neutron or proton number changes, this is part of the interaction cross section and can be split into the neutron-removal cross section, $\sigma_{\Delta N}$, and the charge-changing cross section, $\sigma_{\Delta Z}$. These measured cross sections need to be compared to mean-field theory in order to extract the relation to L, which is done using reaction models based on Glauber multiple-scattering theory. This theory relates the total reaction cross section and the RMS radius. Reaction probabilities are modeled as a function of the distance between the incoming beam and target nuclei, which is known as the impact parameter, and is most commonly depicted in a straight-line trajectory. With the condition the nuclear-induced reaction comes from the overlap of both nuclei, the input for the calculation is the projectile and target densities. The nucleon-nucleon interaction probability is included from the free nucleon-nucleon interaction cross section. The total reaction cross section $\sigma_{\Delta R}$ is obtained when the total reaction probability is integrated over the impact parameter. If the target density is well known, the projectile density distribution can be adjusted to obtain an experimental cross section [Sch17]. The Glauber model will be described in more detail in the following chapter.

In Fig. 1.10, a simplified illustration of the Glauber model using a reaction between beam and target can be seen. Depending on where the collision occurs, protons and neutrons can be ejected. The closer this collision happens to the core of the nuclei, the more likely it is for both protons and neutrons to be knocked out and this probability is calculated with the charge-changing cross section and is related to the proton distribution radii, r_p. When nuclei become very neutron-rich and the neutron skin forms, it becomes more likely that the projectile only interacts with the neutron skin and thus only knock out neutrons. The probability of this is calculated with neutron-removal cross section, and is related to the neutron distribution radii, r_n. Since the neutron skin thickness is

calculated from $\Delta r_{np} = \langle r_n^2 \rangle^{1/2} - \langle r_p^2 \rangle^{1/2}$, measuring the neutron-removal cross section is a promising method to probe the neutron skin thickness.

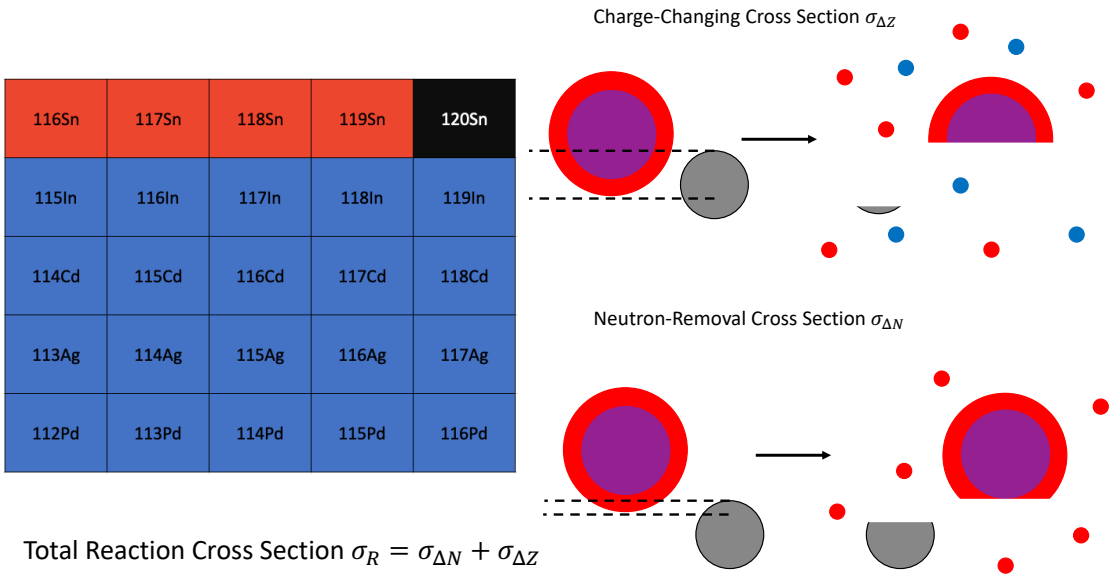

Figure 1.10.: LEFT: Table depicting the possible decays of the ^{120}Sn (black) projectile after interacting with a target. Red squares show the possible daughter nuclei if only neutrons are removed ($\sigma_{\Delta N}$), blue squares show the possible daughter nuclei if at least one proton is removed ($\sigma_{\Delta Z}$). RIGHT: A simple illustration of $\sigma_{\Delta Z}$ (top) and $\sigma_{\Delta N}$ (bottom). The purple circle in the center in the nuclei depicts the area with protons and neutrons, the larger red circle depicts the neutron skin. Depending where the projectile interacts with the target, it is possible for both protons (blue) and neutrons (red) to be ejected, which is $\sigma_{\Delta Z}$. If only neutrons are ejected, it is $\sigma_{\Delta N}$. The total reaction cross section comes from adding these quantities together, σ_R=$\sigma_{\Delta Z}$+$\sigma_{\Delta N}$.

2. Theoretical Background

2.1. The Glauber Model

The model used to explain reaction theories was first developed by Roy J. Glauber in 1959 as a way to explain quantum collisions and is refereed to as the Glauber model [Gla59]. The basis for all models is the eikonal approximation. The Glauber model is critical for predicting the scattering of particles at high energies and assumes the projectile will pass through the target with a straight-line trajectory until its reaction vertex. Generally, Glauber models will treat all possible nucleon-nucleon interactions between the target and projectile with multiple-scattering models. The Glauber model is used to determine the total cross section through the use of proton and neutron densities, and will use nucleon-nucleon cross sections as input [HRB91; Ray79; Abu+08]. An overview of the Glauber model will be presented in this chapter. The two applications of the Glauber model presented here are the Probability Approach (PA) and the Eikonal Optical Limit (EOL). The PA is focused on classical nucleon-nucleon interactions and the EOL is derived from quantum mechanics to describe nucleon-nucleon interaction. For a more detailed description of the Glauber model, please refer to *Introduction to Nuclear Reactions* written by C. Bertulani [BD19] or the PhD thesis of F. Schindler [Sch17].

2.1.1. Reaction Cross Sections

A small introduction to reaction cross sections was given in Ch. 1.4.3. Here, cross sections will be described in more detail. The total cross section can be defined as

$$\sigma_T = \sigma_{el} + \sigma_{inel} + \sigma_I \tag{2.1}$$

where the different cross sections that make up the total cross section are defined as:

- σ_{el} is the total elastic cross section. No nucleon is removed and the projectile stays in the ground state.

- σ_{inel} is the total inelastic cross section. No nucleon is removed but the projectile is excited to a bound state.
- σ_I is the total interaction cross section. At least one nucleon is removed from the projectile.

The total reaction cross section is when a change occurs to the projectile, and is therefore defined as

$$\sigma_R = \sigma_{inel} + \sigma_I \tag{2.2}$$

which allows the total cross section to be written as

$$\sigma_T = \sigma_{el} + \sigma_R. \tag{2.3}$$

For high beam energies, the contribution for σ_{inel} is very small. This is further reduced in a nucleus-nucleus reaction due to Pauli blocking, as possible states to transition into are filled with other nucleons, and the Pauli principle forbids the excitation of the nucleus to certain bound states. Therefore the total reaction cross section can be approximated as

$$\sigma_R \approx \sigma_I \tag{2.4}$$

As discussed briefly in Ch. 1.4.3, the interaction cross section is defined as

$$\sigma_I = \sigma_{\Delta Z} + \sigma_{\Delta N} \tag{2.5}$$

where $\sigma_{\Delta Z}$ is the total charge-changing cross section and has at least one proton removed from the projectile and $\sigma_{\Delta N}$ is the total neutron removal cross section and at least one neutron is removed from the projectile, but the charge number remains the same. The approximation in Eq. 2.4 makes it possible to compare theory and experimental since the difference between the total reaction cross sections and total interaction cross sections is very small at high energies, proven by the Glauber model [OYS92].

2.1.2. Probability Approach

A schematic of a nucleon-nucleon interaction that can help visualize the variables used in the following equations can be seen in Fig. 2.1. A projectile moves towards a target and collides with some amount of overlap. When the collision occurs, one or many nucleons are removed and create a pre-fragment. The pre-fragment will be excited and more nucleons will evaporate, leaving behind the final fragment. The probability a projectile nucleon will be found in the region of $d\vec{s}dz_P$ is given by

$$p(\vec{s}, z_P) = \rho_P(\vec{s}, z_P) \cdot d\vec{s}dz_P \tag{2.6}$$

where

$$\int \rho_P(\vec{s}Z_P)d\vec{s}dz_P = 1 \tag{2.7}$$

T is known as the thickness function and is the probability that a nucleon is located in a certain area. The thickness functions for finding a nucleon at position $\vec{s}$ or $\vec{s} - \vec{b}$ are defined as

$$T_P(\vec{s}) = \int \rho_P(\vec{s}, z_P)dz_P \tag{2.8}$$

$$T_T(\vec{s} - \vec{b}) = \int \rho_T(\vec{s} - \vec{b}, z_T)dz_T \tag{2.9}$$

The overlap function between these two is then defined as

$$T_{PT}(\vec{b}) = \int T_P(\vec{s}) \cdot T_T(\vec{s} - \vec{b}))d\vec{s}. \tag{2.10}$$

The overlap function is the probability that a projectile and target nucleon will be found in an overlapping area at impact parameter $\vec{b}$. The interaction probability is found by multiplying Eq. 2.10 by the nucleon-nucleon interaction cross section, σ_{NN}, which gives

$$p_{NN}(\vec{b} = \sigma_{NN}T_{PT}(\vec{b}). \tag{2.11}$$

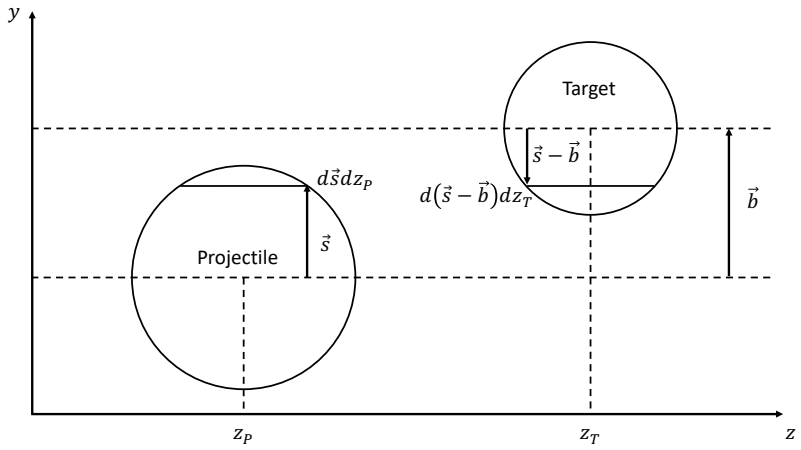

Figure 2.1.: A schematic drawing of a nucleon-nucleon collision. After the projectile hits the target, a pre-fragment will form. The pre-fragment will be excited, which will lead to more nucleons evaporating and resulting in the final fragment.

Instead of solving the multiple-scattering problem exactly, only the probabilities of the individual nucleon-nucleon interactions in a nucleus-nucleus collision are taken into account. For example, the probability of exactly n nucleon-nucleon primary interactions in a nucleus-nucleus collision at impact parameter $\vec{b}$ out of $A_P \cdot A_T$ possibilities is defined as

$$p(n, \vec{b}) = \binom{A_P A_T}{n} [P_{NN}(\vec{b})]^n [1 - p_{NN}(\vec{b})]^{A_P A_T - n} \tag{2.12}$$

where the first term is the number of combinations to select n nucleon-nucleon pairs out of $A_P A_T$ possibilities, the second term is the probability that exactly n nucleon-nucleon interactions will happen, and the third term is the probability that $A_P A_T - n$ would miss. This then leads into the optical limit of the probability approach framework. The total interaction probability at impact parameter $\vec{b}$ is defined as

$$P(\vec{b}) = \sum_{n=1}^{A_P A_T} P(n, \vec{b}) \tag{2.13}$$

and after some derivation steps, Eq. 2.13 can be written as;

$$= 1 - (1 - p_{NN}(\vec{b}))^{A_P A_T}. \tag{2.14}$$

The total reaction cross section, σ_R can then be derived by integrating Eq. 2.14 over $\vec{b}$

$$= \int d\vec{b}[1 - (1 - p_{NN}(\vec{b}))^{A_P A_T}]. \tag{2.15}$$

The fact that this calculation is possible over specific reaction channels makes the probability approach a powerful framework. The counter part of Eq. 2.14 is looked at in the following section, the Eikonal Optical Limit, where it is not possible to calculate reaction processes over a specific number of nucleons.

2.1.3. Eikonal Optical Limit

To calculate all possible nucleon-nucleon interactions between a projectile and a target, additional approximations are added to the calculations to make integrating over large systems simpler. These approximations are known as the optical-limit representation of the theory. This causes a large simplification of the framework and also reduces the output of information from the calculation.

The eikonal optical limit starts with the quantum mechanics scattering problem of a plane wave from a short-range potential $V(\vec{r})$ [BD19] that can be formulated using the time-independent

Schrodinger equation

$$H\psi_{\vec{k}}(\vec{r}) = E\psi_{\vec{k}}(\vec{r}) \tag{2.16}$$

with the Hamiltonian

$$H = -\frac{\hbar^2}{2\mu}\vec{\nabla}^2 + V(\vec{r}) \tag{2.17}$$

The end goal is to find a solution $\psi_{\vec{k}}(\vec{r})$ that fulfills Eq. 2.16 under specified boundary conditions for stationary charges with energy eigenvalues

$$E = \frac{k^2\hbar^2}{2\mu} \tag{2.18}$$

where k is the wave number and μ is the reduced mass. The solution to the Schrodinger equation can be written as a distortion of a plane-wave

$$\psi_{\vec{k}}(\vec{r}) = \phi_{\vec{k}}(\vec{r}) + \psi^{sc}_{\vec{k}}(\vec{r}) \tag{2.19}$$

where $\phi_{\vec{k}}(\vec{r})$ is the oncoming wave plane, and $\psi^{sc}_{\vec{k}}(\vec{r})$ is asymptotically an outgoing spherical wave caused by scattering. As $r \to \infty$,

$$\psi^{sc}_{\vec{k}}(\vec{r}) \to f(\Omega)\frac{e^{ikr}}{r} \tag{2.20}$$

needs to be fulfilled, where $f(\Omega) = f(\theta, \varphi)$ is the scattering amplitude and has all the information regarding the orientation and the strength of the scattering process. From here, a central potential is assumed, which leads to a reduced angular dependence of the scattering amplitude, $f(\Omega) = f(\theta)$. Eq. 2.16 can then be written as

$$\psi_{\vec{k}}(\vec{r}) \to A\left(e^{i\vec{k}\cdot\vec{r}} + f(\theta)\frac{e^{ikr}}{r}\right). \tag{2.21}$$

where A is a normalization constant.

For the full derivation of the Schrodinger equation, please refer to the thesis of F. Schindler [Sch17]. Only the most important parts of the derivation will be discussed from here.

The solution of the Schrodinger equation can be further analyzed by changing to the Dirac notation [BD19]

$$H|\psi_{\vec{k}}\rangle = E|\psi_{\vec{k}}\rangle \tag{2.22}$$

with the normalization $\langle\psi_{\vec{k'}}|\psi_{\vec{k}}\rangle = \delta(\vec{k} - \vec{k'})$ of the state $|\psi_{\vec{k}}\rangle$. Implementing Green's operators leads to an integral representation of the Schrodinger equation and is known as the Lippmann-Schwinger equation. When the asymptotic solution is combined with Eq. 2.21, the normalization constant

$A = 1/(2\pi)^{3/2}$ is found, as well as the scattering amplitude, which can be written as

$$f(\theta) = -2\pi^2 \left(\frac{2\mu}{\hbar^2}\right) \langle \phi_{\vec{k'}} | V(\vec{r}) | \psi_{\vec{k}} \rangle = -2\pi^2 \left(\frac{2\mu}{\hbar^2}\right) \int \phi^*_{\vec{k'}}(\vec{r}) V(\vec{r}) d\vec{r} \tag{2.23}$$

The absolute square of the scattering amplitude is the differential elastic cross section written as

$$\left(\frac{d\sigma_{el}}{d\Omega}\right) = |f(\theta)|^2 \tag{2.24}$$

and the total cross section according to optical theorem is then

$$\sigma_T = \frac{4\pi}{k} Im[f(\theta = 0)]. \tag{2.25}$$

The Eikonal Wave Function

According to the eikonal approximation, a projectile will pass the target with a straight-line trajectory. To define the cross section equations, the derivation of the Schrodinger equation moves to cylindrical coordinates $\vec{r} = (\rho \cos\varphi, \rho \sin\varphi, z) = (\vec{b}, z)$ where z is the beam direction and the solution $\psi_{\vec{k}}(\vec{r})$ is now expressed as

$$\psi_{\vec{k}}(\vec{r} = e^{ikz} \phi(\vec{b}, z) \tag{2.26}$$

where e^{ikz} is a plane wave travelling in the beam direction z and $\phi(\vec{b}, z)$ is the distortion caused by the potential $V(\vec{r})$. Using the Laplace operator in cylindrical coordinates, the Schrodinger equation becomes:

$$e^{ikz} \vec{\nabla}^2_{\vec{b}} \phi(\vec{b}, z) + 2ike^{ikz} \frac{\partial \phi(\vec{b}, z)}{\partial z} + e^{ikz} \frac{\partial^2 \phi(\vec{b}, z)}{\partial z^2} - \frac{2\mu}{\hbar^2} V(\vec{r}) e^{ikz} \phi(\vec{b}, z) = 0. \tag{2.27}$$

The first and third term of Eq. 2.27 are due to the fact that the potential $\phi(\vec{b}, z)$ varies slowly, so the formula can be simplified to

$$\frac{\partial \phi(\vec{r})}{\partial z} + \frac{i\mu}{\hbar^2 k} V(\vec{r}) \phi(\vec{r}) = 0 \tag{2.28}$$

and the Schrodinger equation is now a first-order differential equation for $\phi(\vec{r})$. If the potential is far away, the incoming plane-wave propagates undistorted. The distortion of a plane-wave is expressed as an integral of the scattering potential along the beam direction. Because of this, the equation only holds when the projectile crosses the target with a straight-line trajectory. The eikonal wave function is defined to be

$$\psi_{\vec{k}}(\vec{r}) = e^{ikz + i\chi(\vec{b}, z)}. \tag{2.29}$$

Next, the elastic scattering amplitude in the eikonal approximation is derived as

$$f_{el}(\theta) = -\frac{ik}{2\pi}\int d\vec{b}e^{i\vec{q}\cdot\vec{b}}(e^{i\chi(\vec{b})}-1) \tag{2.30}$$

and the total elastic cross section can be written as

$$\sigma_{el} = \int |e^{i\chi(\vec{b})}-1|^2 d\vec{b}. \tag{2.31}$$

The total cross section from Eq. 2.25 is derived from Eq. 2.30 at zero momentum transfer $(\theta = 0)$

$$\sigma_T = 2\int \left(1 - Re\left[e^{i\chi(\vec{b})}\right]\right) d\vec{b} \tag{2.32}$$

and the total reaction cross section can be written as

$$\sigma_R = \sigma_T - \sigma_{el} = \int \left(1 - |e^{i\chi}(\vec{b})|^2\right) d\vec{b}. \tag{2.33}$$

The scattering matrix is defined as $S(\vec{b}) \equiv e^{i\chi(\vec{b})}$, so the cross sections can be written as:

$$\sigma_{el} = \int |1 - s(\vec{b})|^2 d\vec{b} \tag{2.34}$$

$$\sigma_T = 2\int (1 - Re[s(\vec{b})]) d\vec{b} \tag{2.35}$$

$$\sigma_R = \int (1 - |S(\vec{b})|^2) d\vec{b}. \tag{2.36}$$

Scattering Potential

The cross section solutions are dependent on the specified scattering potential. Coulomb potential is disregarded in the following case since the focus is on nuclear reactions. For the nuclear part, optical potentials based on the many-body scattering theory are considered. For Glauber calculations in the eikonal approximation, only the first order of the parametrization will be used. The interaction does not depend on the spin and many-body nucleon-nucleon correlations are ignored. The potential is dependent on the ground state nucleon density distribution ρ and the free nucleon-nucleon interaction cross section is included from the transition matrix element t. This is what is known as the $t\rho\rho$ approximation [HRB91]. If a proton is considered as the nucleon in the interaction between a single nucleon and a target nucleon, the first order optical potential is written as

$$V_{opt}(\vec{r}) = t_{np}\rho_n(\vec{r}) + t_{nn}\rho_p(\vec{r}) \tag{2.37}$$

where p is the the proton property and n is the neutron property. Combining with Eq. 2.23, the transition matrix elements t_{pi} can be expressed as a function of the proton-nucleon scattering amplitude $f_{pi}(\theta)$

$$t_{pi} = -\frac{\hbar^2}{2\mu}\frac{1}{2\pi^2}f_{pi}(\theta) \tag{2.38}$$

Using the scattering amplitude at zero momentum transfer and the transition element for $\theta = 0$ is

$$t_{pi} = -\frac{\hbar^2 k}{2\mu}\frac{1}{(2\pi)^3}\sigma_{pi}(\alpha_{pi} + i) \tag{2.39}$$

where σ_{pi} is the free proton-nucleon cross section. $\frac{1}{(2\pi)^3}$ is the square of the wave function ϕ normalization. If this factor is set to 1 and $\rho = |\phi|^2$ is normalized to 1, Eq. 2.39 becomes

$$t_{pi} = -\frac{\hbar^2 k}{2\mu}\sigma_{pi}(\alpha_{pi} + i) \tag{2.40}$$

and Eq. 2.37 becomes

$$V(\vec{r}) = \left(-\frac{\hbar^2 k}{2\mu}\big(\sigma_{pn}\alpha_{pn}\rho_n(\vec{r}) + \sigma_{pp}\alpha_{pp}\rho_p(\vec{r})\big)\right) + i\left(-\frac{\hbar^2 k}{2\mu}\big(\sigma_{pn}\rho_n(\vec{r}) + \sigma_{pp}\rho(\vec{r})\big)\right). \tag{2.41}$$

Using $V(\vec{r})$ to write the eikonal phase

$$|S(\vec{b})|^2 = |e^{i\chi(\vec{b})}|^2 = exp\left(\frac{2\mu}{\hbar^2 k}\int_{-\infty}^{\infty} Im[V(\vec{r})]dz'\right), \tag{2.42}$$

Eq. 2.36 becomes free of parameter α and the real part of the optical potential. Focusing on the total reaction cross section, the isospin averaged transition element is used to extend the imaginary part of $V(\vec{r})$ to a nucleus-nucleus potential

$$t_{NN} = \frac{Z_p N_T + Z_T N_p}{A_p A_T}t_{pn} + \frac{Z_p Z_T + N_p N_T}{A_p A_T}t_{pp} \tag{2.43}$$

$$= -i\frac{\hbar^2 k}{2\mu}\left[\frac{Z_p N_T + Z_T N_p}{A_p A_T}\sigma_{pn} + \frac{Z_p Z_T + N_p N_T}{A_p A_T}\sigma_{pp}\right] = -i\frac{\hbar^2 k}{2\mu}\sigma_{NN} \tag{2.44}$$

where N, Z, and A are the neutron, proton, and mass numbers for the projectile and target nuclei. Replacing the single particle densities in Eq. 2.41 with an integral over the nuclear density distributions $\rho_p(\vec{r})$ and $\rho_T(\vec{r})$ normalized according to the mass number leads to an optical representation of

$$S(\vec{b}) = exp\left[-\frac{\sigma_{NN}}{2}\int dz'\int d\vec{r}\rho_p(\vec{r})\rho_T(\vec{r} - \vec{b})\right] \tag{2.45}$$

where $\vec{b}$ is the impact parameter and S becomes a function of $\vec{b}$.

2.1.4. Charge-Changing Cross Sections in the PA and EOL Models

Since the analysis presented in this thesis was only done for the charge-changing cross section, the total-reaction and neutron-removal cross sections will no longer be discussed unless in relation to the charge-changing cross section. The charge-changing cross section can be defined in the following way

$$\tilde{\sigma}_{\Delta Z} \quad \rightarrow \quad Z_i \neq Z_f \quad N_i = N_f \tag{2.46}$$

$$\tilde{\sigma}_{\Delta Z \Delta N} \quad \rightarrow \quad Z_i \neq Z_f \quad N_i \neq N_f \tag{2.47}$$

where i is the number of incoming and f is the final number of projectile protons Z or neutrons N. The charge-changing cross section can then be written as

$$\sigma_{\Delta Z} = \tilde{\sigma}_{\Delta Z} + \tilde{\sigma}_{\Delta Z \Delta N} \tag{2.48}$$

The projectile density is the sum of the proton p and neutron density distribution in a nucleus

$$\rho_P = \rho_P^p + \rho_P^n \tag{2.49}$$

where ρ_P^p and ρ_P^n are normalized to Z and N, respectively. Continuing,

$$\sigma = 2\pi \int db\, bP(b) = 2\pi \int db\, b(1 - |S(b)|)^2 \tag{2.50}$$

where $P(b)$ is the reaction probability and $|S(b)|^2$ is the survival probability. $|S_p|^2$ and $|S_n|^2$ are then defined as the proton and neutron survival probabilities, so the combined probabilities for the reaction processes are

$$\tilde{P}_{\Delta Z} = (1 - |S_p|^2)|S_n|^2 \tag{2.51}$$

$$\tilde{P}_{\Delta Z \Delta N} = (1 - |S_p|^2)(1 - |S_n|^2) \tag{2.52}$$

Combining Equations 2.51 and 2.52, the charge-changing probability is found

$$P_{\Delta Z} = \tilde{P}_{\Delta Z} + \tilde{P}_{\Delta Z \Delta N} = 1 - |S_p|^2 \tag{2.53}$$

Charge-Changing Cross Section in the PA Model

The probability model is useful because it allows for the a detailed analysis of single reaction channels. It was previously derived that the probability of a projectile nucleon A_P will react with target nucleon

A_T is

$$P_N(\vec{b}) = 1 - \left(1 - (P_{NN}(\vec{b})\right)^{A_P A_T} \tag{2.54}$$

where

$$P_{NN}(\vec{b}) = \frac{\sigma}{A_P A_T} \int dx \int dy \int \rho_P dz \int \rho_T dz' \tag{2.55}$$

Eq. 2.54 can be rewritten as

$$P_N = 1 - |S|^2 \tag{2.56}$$

where the probability of a projectile proton reacting with the target is written as

$$P_p = 1 - |S_p|^2 \tag{2.57}$$

with

$$|S_p|^2 = (1 - P_{pN})^{Z_P A_T} \tag{2.58}$$

and

$$P_{pN} = \frac{\sigma}{Z_P A_P} \int dx \int dy \int \rho_P^p dz \int \rho_T dz' \tag{2.59}$$

Combining with Eq. 2.50 gives the charge changing cross section in the probability approach model

$$\sigma_{\Delta Z}^{PA} = 2\pi \int b \left(1 - \left[1 - \frac{\sigma}{Z_P A_T} \int dx \int dy \int \rho_P^p dz \int \rho_T dz'\right]^{Z_P A_T}\right) db. \tag{2.60}$$

Charge-Changing Cross Section in the EOL

The equation for the reaction cross section of at least one projectile nucleon removed can be deduced from Eq. 2.36.

$$\sigma_I = 2\pi \int bP(b)db = 2\pi \int b(1 - |s(b)|^2)db \tag{2.61}$$

where

$$|S|^2 = exp\left[- \sigma \int dx \int dy \int \rho_P dz \int \rho_T dz' \right] \tag{2.62}$$

is the nucleon survival probability. Replacing the total density ρ_P with proton specific density $-rho_P^p$, the charge-changing cross section in the EOL model is found to be

$$\sigma_{\Delta Z}^{eol} = 2\pi \int b \left(1 - exp\left[- \sigma \int dx \int dy \int \rho_P^p dz \int \rho_T dz' \right]\right) db. \tag{2.63}$$

2.2. Calculations with the Glauber Model

The Glauber model has been used to calculate the charge-changing, neutron-removal, and total reaction cross sections for ^{12}C and these results will be presented below. There is a lot of data available on the charge distribution for ^{12}C, which makes this a good test subject to test the reaction theory on. The work in this thesis focuses on the charge-changing cross section for ^{120}Sn, and these results will also be presented.

2.2.1. ^{12}C+^{12}C Calculations

Experimental information on the charge radius of ^{12}C can be derived from electron scattering experiments and muonic x-ray spectroscopy. Charge information for ^{12}C via muonic x-ray spectroscopy can be found in [Off+91]. The density distributions are used to calculate cross sections in the Glauber Model for the reaction ^{12}C+^{12}C. These cross sections as a function of energy can be seen in Fig. 2.2. Experimental data comes from [Tak+09] for the energy range of 100-400 MeV/nucleon, [MNN90] for 790 MeV/nucleon, and [Oza+01] for 950 MeV/nucleon. The total reaction cross section is calculated using the density distributions and the nucleon-nucleon cross section as seen in the top part of Fig. 2.2. The calculated cross sections overestimate the experimental values for energies larger than 20 MeV. Much of this deviation can be explained when Pauli blocking and Coulomb deflection are taken into account, which can be seen by the red dots. The deviations below 400 MeV/nucleon are not further investigated because effects beyond the eikonal approach play a large role.

It can be seen in Fig. 2.2 that experimental data is missing between the key range of 400-800 MeV/nucleon. An experiment to fill in the missing energies was done directly before the experiment presented in this thesis. The data analysis and cross section calculations are currently being completed by L. Ponnath. Once these calculations are completed, the reliability of the Glauber method can be better known.

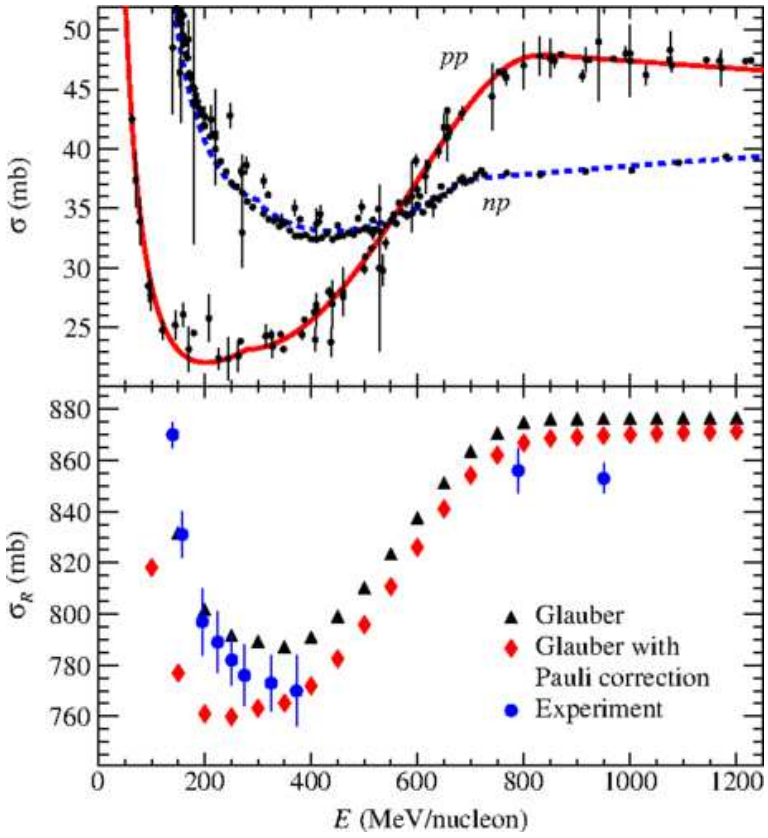

Figure 2.2.: (Top) Nucleon-nucleon and (Bottom) total reaction cross sections for ^{12}C on ^{12}C as a function of beam energy. Black triangles show parameter free eikonal calculations in the optical limit, while the red diamonds show calculation including the effect of Pauli Blocking. Blue dots are experimental data (100-400 MeV/nucleon [Tak+09], 790 MeV/nucleon [MNN90], and 950 MeV/nucleon [Oza+01]) and it is noticeable that data is missing between 400 MeV/nucleon and 800 MeV/nucleon. Calculations are done with the EOL model and image is taken from [Aum+17].

2.2.2. Sn Cross Section Calculations

The calculations presented here come from the DD2 interaction, which was developed by S. Typel [Typ+10]. DD2 is a modification to the DD approach that used experimental nucleon masses [Typ05]. Isovector parameters were optimized by fitting nuclear properties such as mass and radii in [Typ14]. Values from here are used to study the dependence between the neutron skin thickness and the symmetry energy slope parameter L. The L parameter was varied from 25 MeV (DD2^{--}) to 100 MeV (DD2^{+++}). All the symmetry energy slope parameters for L and symmetry energy coefficients for J used can be found in Tab. 2.1.

Parametrization	J (MeV)	L (MeV)
1 DD2^{+++}	35.34	100.00
2 DD2^{++}	34.12	85.00
3 DD2^{+}	32.98	70.00
4 DD2	31.67	55.04
5 DD2^{-}	30.09	40.00
6 DD2^{--}	28.22	25.00

Table 2.1.: Symmetry energy coefficients for J and symmetry energy slope parameters for L used in different DD2 parameterizations [Typ14].

The predicted values for the neutron skin thickness Δr_{np} and corresponding neutron removal cross section $\sigma_{\Delta N}$ for $^{124\text{-}134}$Sn using the DD2 interaction can be seen in Fig. 2.3. The range of the neutron skin for ^{132}Sn ranges from 0.15-0.34 fm. This leads to a corresponding range in the total reaction cross section from 2550-2610 mb, which is 2.5%. However, when looking at the neutron-removal cross section, the range is from 460-540 mb, which is a 20% difference. Thus, the neutron-removal cross section has high potential to tightly constrain L and is also less sensitive to imperfections of the reaction theory [Aum+17].

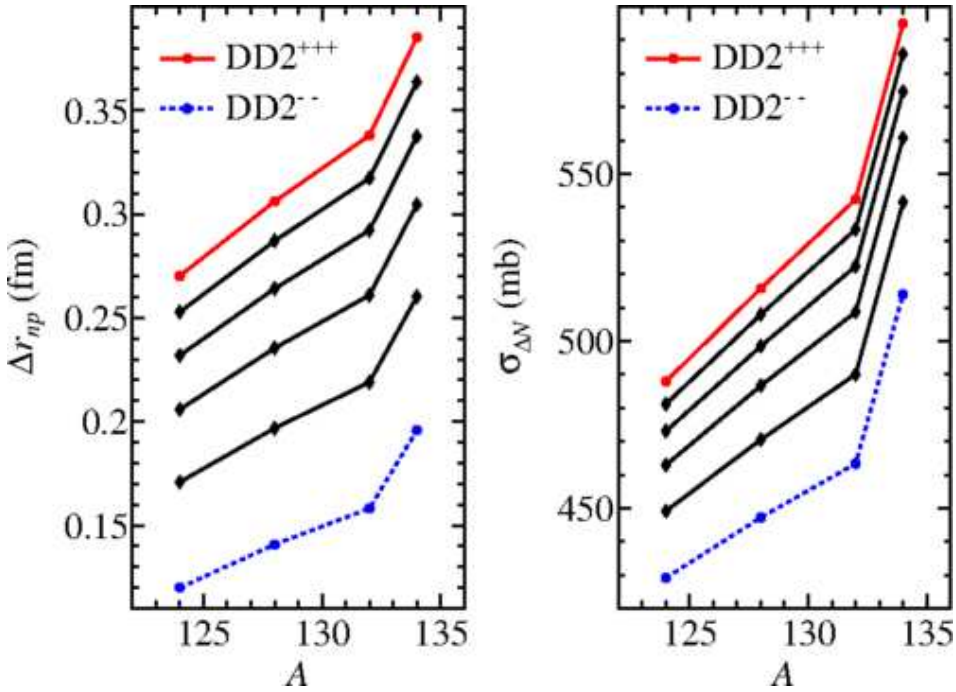

Figure 2.3.: Predicted values for the Neutron-skin thickness Δr_{np} (Left) and the corresponding neutron-removal cross section $\sigma_{\Delta N}$ (Right) calculated with the relativistic mean-field theory using variations of the DD2 interaction. L has been systematically varied between 25 MeV (DD2^{--}) and 100 MeV (DD2^{+++}) [Typ14]. Image is taken from [Aum+17].

In Fig. 2.4, the correlation between the L values used in the DD2 interaction, and the neutron-removal cross section (top) and the neutron skin thickness (bottom). The red diamonds represent ^{124}Sn and the blue dots represent ^{132}Sn. L has a change of ± 5 MeV in this interaction and a change of ± 0.01 fm in the calculated neutron skin thickness for ^{124}Sn. This leads to a change of ± 5 mb in the neutron-removal cross section, or ± 1 %. So, if the neutron-removal cross section can be determined with 1 % accuracy both experimentally and theoretically, the theoretical limit for L could be reached. A 2 % accuracy is necessary to reach the 10 MeV constraint on L limited by the model dependence, as estimated by X. Roca-Maza [Roc+11]. And since the dependence of the cross section on L becomes larger as nuclei become more neutron-rich, these nuclei can provide a higher sensitivity.

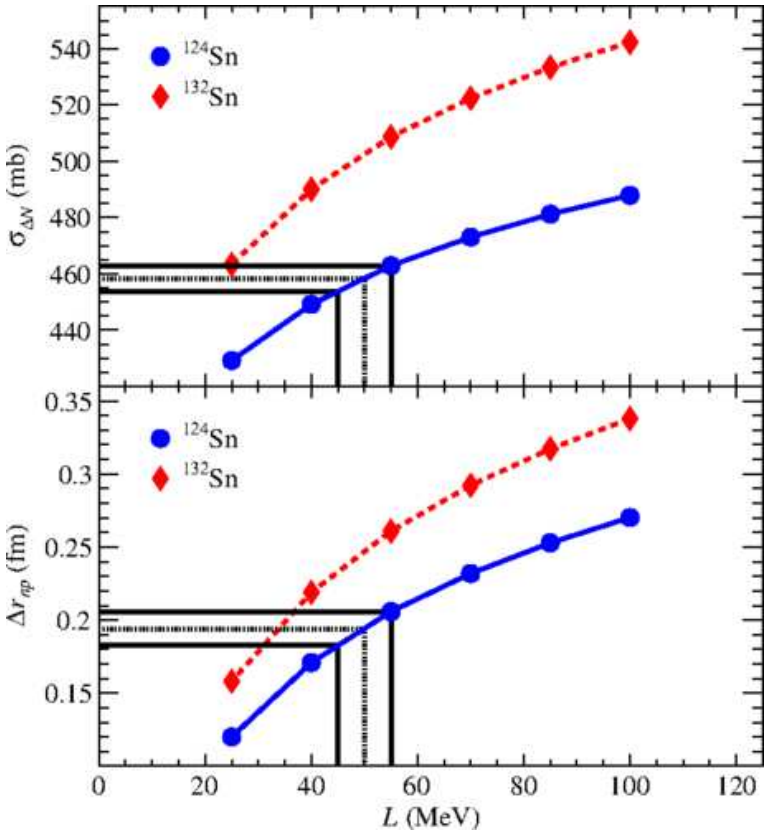

Figure 2.4.: Relation between $\sigma_{\Delta N}$ (Top) and Δr_{np} (Bottom) with parameter L for ^{124}Sn and ^{132}Sn. Calculations are based off of Relativistic Mean-Field theory. Lines are added to emphasize the sensitivity of L for a range of 10 MeV. Image is taken from [Aum+17].

The performance of this model has been tested using ^{12}C+^{12}C since there is information available on the total reaction cross section using the eikonal approximation. Input for the reaction theory comes from known nucleon-nucleon cross sections and densities, and any additional energy parameters that are often used, like in [Ray79; Hor+07; Kan+16], are omitted as they would hide deficiencies that come from the optical-limit eikonal approximation. The sensitivity can be

pushed further by changing which reaction target is used. A change in the neutron-removal and charge-changing cross sections as a function of energy should correspond to the difference in energy dependence of the pn and pp cross sections. The most obvious effect comes from using a proton target since the protons interact with the neutron skin via pn reactions. Additional factors should aslo be considered, such as the non-negligible chance that a proton will pass through the nucleus with out knocking out a nucleon. The ratios for the neutron-removal, charge-changing, and total reaction cross sections for a proton target, $\sigma_R(p)$, and a ^{12}C target, $\sigma_R(^{12}\mathrm{C})$, as a function of energy can be seen in Fig. 2.5. There is no energy dependence seen for $\sigma_R(p)/\sigma_R(^{12}\mathrm{C})$ target ratio, but a dependence for $\sigma_{\Delta Z}(p)/\sigma_{\Delta Z}(^{12}\mathrm{C})$ and $\sigma_{\Delta N}(p)/\sigma_{\Delta N}(^{12}\mathrm{C})$ can be seen. The strong dependence seen from the neutron-removal cross section comes from the strong energy dependence of the pp cross section. This energy dependence then provides a very sensitive test for the reaction theory when measured accurately. The charge-changing cross sections for proton and ^{12}C targets as a function of energy is also a useful test for the accuracy of the predicated cross sections because the rms radius of the charge distribution is known.

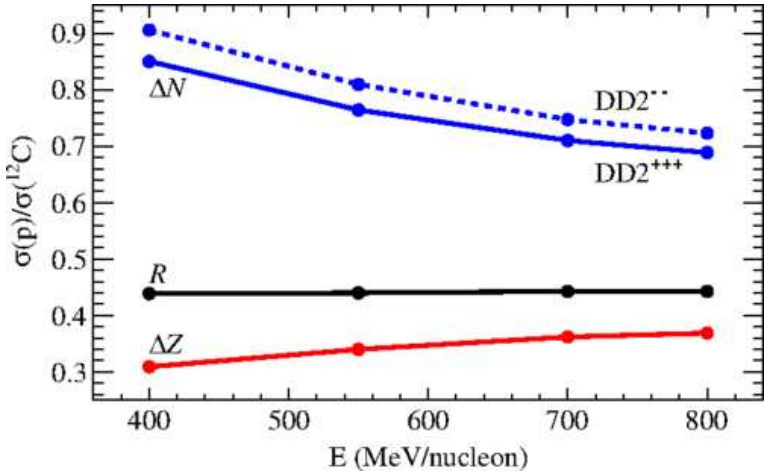

Figure 2.5.: Ratios of σ_R, $\sigma_{\Delta Z}$, and $\sigma_{\Delta N}$ for ^{134}Sn projectiles on a ^{12}C target as a function of the bombarding energy. There is no energy dependence for the total reaction cross section and a very small energy dependence for the charge changing cross section. However, there is a large energy dependence for the neutron removal cross section. Replicating this result in experiment would be a good test for the reaction theory. Image is taken from [Aum+17].

Theoretical calculations done for the charge-changing cross section of ^{120}Sn+^{12}C by C. Bertulani and their relation to experimental obtained cross sections can be found in Ch. 5.

3. Experimental Setup

The data presented in this thesis was taken during the experimental campaign s473 which took place at the research facility GSI Helmholtzzentrum für Schwerionenforschung GmbH (GSI) in February of 2019 as part of the R^{3}B Collaboration. The aim of this experiment was to prove that it is possible to accurately calculate charge-changing, neutron-removal, and total reaction cross sections with the R^{3}B setup. The following chapter will describe the accelerator facility, general setup, detectors, and the daq system used to acquire the data used in this analysis.

3.1. The GSI Accelerator Facility

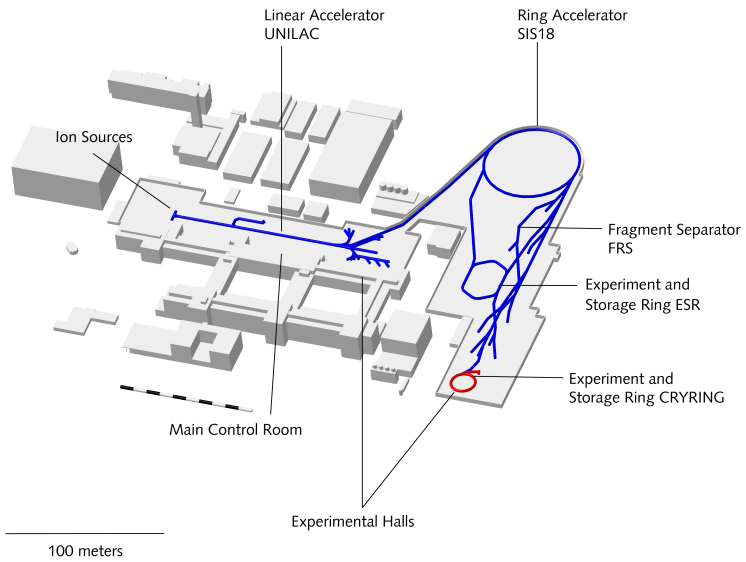

Figure 3.1.: Overview of the accelerator facility at GSI. The beam will start in from the ion source and get accelerated first in the UNILAC. The beam then moves to the SIS18 where it is accelerated to the desired energy. It is then sent to the experimental halls- Cave C for R^{3}B experiments. Image is taken from [GSI].

GSI is home to one of the most powerful accelerators in the world. It is currently the only accelerator facility in the world that can allow for the acceleration of all of the chemical elements occurring on Earth. For s473, it was required that there were high beam energies and a large-acceptance spectrometer. This again only exists at GSI using the combination of the SIS18-R3B for high beam energies and the new R3B-GLAD large-acceptance spectrometer.

The starting point for the ions is the Universal Linear Accelerator (UNILAC) which can accelerate all ions up to 11.4 MeV/u. The ions are either sent to experiments in Experimental Hall I or forwarded on to the ring accelerator Schwerionensynchrotron 18 (SIS18) to be further accelerated. If the ions are sent to the SIS18, once they have reached their desired energy, the ions will be forwarded on either directly to the experimental halls or continue on to either the experimental storage ring (ESR) or the fragment separator (FRS) if an exotic isotope is desired. This experiment used only the UNILAC and SIS18 since a stable beam of ^{120}Sn was used and it was not necessary to use the FRS.

3.1.1. R^{3}B Setup

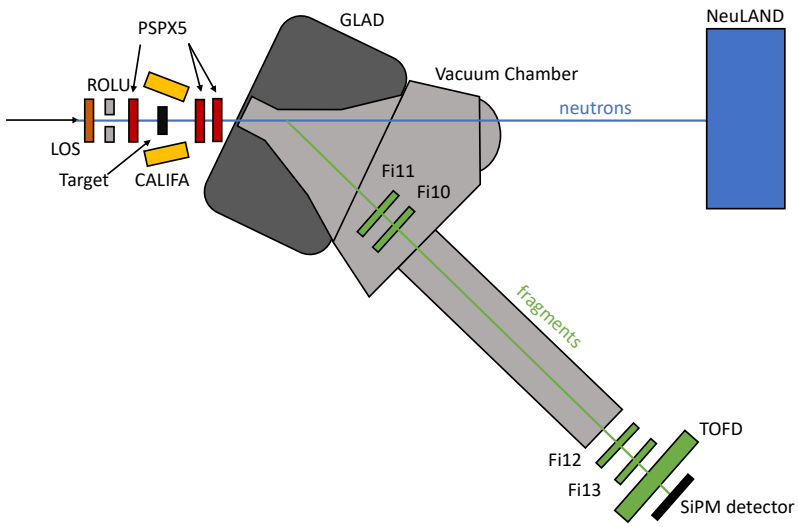

Figure 3.2.: Beam line configuration for the s473 Experimental Campaign. The beam enters the setup from the left and first hits the start detector LOS in orange. It then travels through the collimater ROLU and the first PSPX5 detector in red. The target is next surrounded by the gamma detector CALIFA in yellow. The beam then enters the magnet GLAD and is bent to 18°. The neutrons continue in a straight-line trajectory and are detected by NeuLAND in blue. The fragments are bent and travel to the tracking detectors- the fiber detectors (Fi10, Fi11, Fi12, and Fi13) and TOFD in green. The SiPM detector seen in black at the end of the fragment arm was in this experiment for testing purposes. The individual detectors are described in the text.

The experimental campaign s473 was done at the R^3B (Reactions with Relativistic Radioactive Beams) Setup of GSI located in cave C [R3B]. This experiment was one of the first to be completed in what is known as FAIR Phase 0. The Facility for Antiproton and Ion Research (FAIR) is currently under construction at GSI. FAIR will have the ability to accelerate particles to energies of 0.4 to 1.5 GeV/u with [SF06]. This is very important for the R^3B collaboration because the experiments rely on very high beam energies. Once completed, R^3B will move operations to the new facility.

3.2. GLAD

Even though FAIR is still under construction, some of the equipment that will be used is already built and operational. The new GSI Large-acceptance dipole magnet (GLAD) has been installed in cave C since February of 2016. GLAD is a zero-degree superconducting dipole magnet and has the following main parameters: (i) A large vertical gap providing an angular acceptance of $\pm$80 mrad for neutrons; (ii) A maximum bending angle of 40°, ensuring an acceptance of close to 100% even for experiments with very different magnetic rigidities of the beam and the fragments; (iii) A high field integral of about 5 Tm, which allows for a a bending angle of 18° for a 15 Tm beam. The design of GLAD includes four superconducting coils which are tilted to match the required acceptance angle for the particles of interest. The side coils are optimized to reduce the fringe field in order to guarantee a low magnetic field in the target region, where the detectors have to be placed [GSI].

3.3. Detectors

The detector setup for s473 can be seen in Fig. 3.2. The setup for R^3B changes from experiment to experiment, but there is a general overlap in the detectors used. A brief overview of each detector will be described below since many of these detectors have been described extensively in other thesis and publications before.

3.3.1. LOS

The first detector in the s473 setup was LOS. LOS is the start detector for the time of flight measurement for all of the detectors in the R^3B setup. LOS is comprised of eight Hamamatsu R8619 PMTs arranged in an octagonal pattern. The PMTs are directly coupled to the scintillator with optical glue. LOS is also used for position and energy-loss measurements. The time of flight measurement is calculated by taking an average of the eight different times measured by each PMT. The position

is calculated by utilizing the time difference in opposite PMTs. The nuclear charge of the ions is determined by the energy loss in the scintillator. Both the position and energy-loss measurements are used in the analysis of this experiment. The energy-loss measurements are used to extract the number of incoming particles from the beam while calculating the charge-changing cross section, which will be discussed in more detail in 5.3.

There are two readout electronics used for LOS; a constant fraction discriminator from Mesytec with VFTX [Gro12], which is a FPGA-based TDC module and a FQT, which is a Front-end charge Q and Time board in combination with TAMEX3 [Ugu+], which is another FPGA based multi-hit TDC. However, by the time s473 was running, only the FQT readout system was being used.

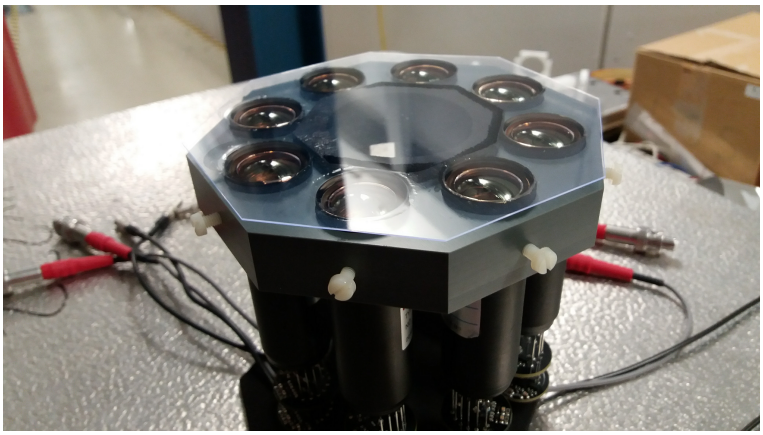

Figure 3.3.: An image of LOS. The eight PMTs can be seen arranged in an octagonal pattern, which are directly coupled to a scintillator. The start time is calculated by taking an average of the eight PMTs. The position is calculated by utilizing the time difference in opposite PMTs. The nuclear charge of the ions is determined by the energy loss in the scintillator. Image was taken by A. Kelic-Heil.

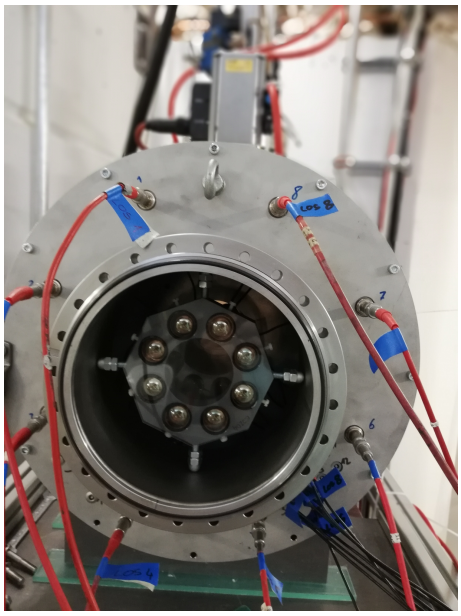

Figure 3.4.: LOS placed in the beam line. Image was taken by A. Kelic-Heil.

3.3.2. ROLU

ROLU stands for rechts, oben, links, and unten. It is the incoming beam collimator at the front of the beam line. ROLU is used to ensure that the beam spot is the desired size. It consists of four scintillators, each read out by a small PMT. These single detectors form an adjustable rectangular frame. The signal from ROLU is then used to reject projectiles from within the beam spot. Information from ROLU was only used during the beam time, not during the analysis.

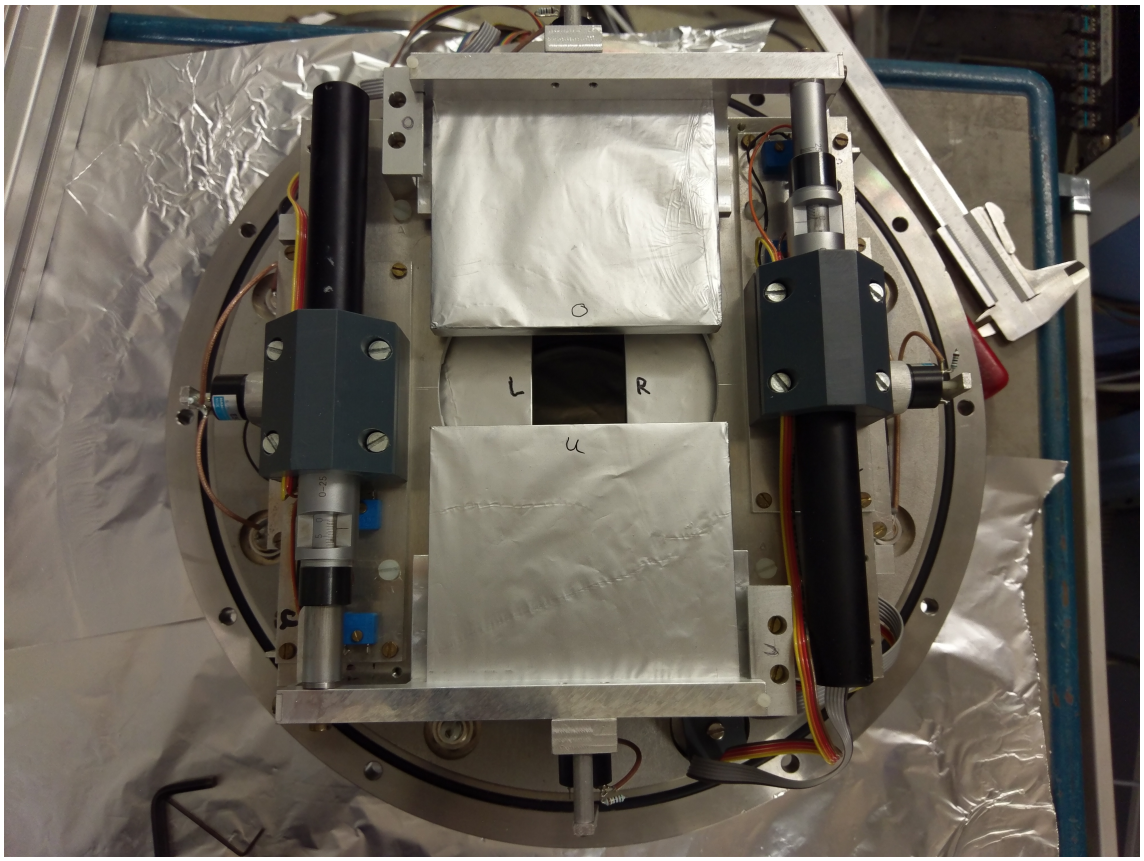

Figure 3.5.: An image of the collimator ROLU placed in the beam line. The four plates in gray marked R-O-L-U are able to move independently and adjust to form the desired beam acceptance. Image was taken by M. Heil.

3.3.3. PSP X5

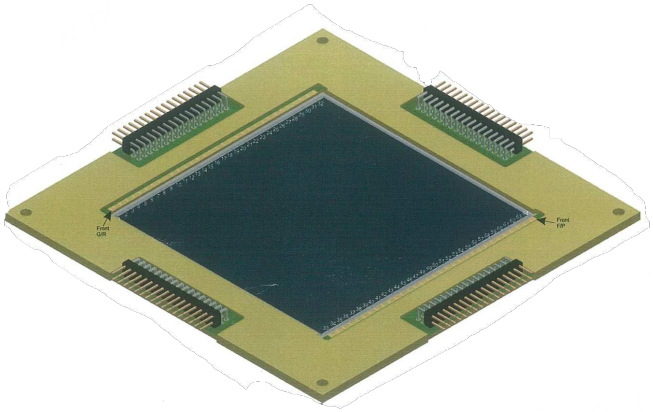

Figure 3.6.: Technical drawing for one side of the PSP X5. The 32 strips are read out on both ends of the detector. There are a total of 128 channels including the connections to the field plates and guard rings. These channels are read out in from the four 34 pin connectors. The drawing is provided from [Mic15].

PSP stands for Position Sensitive Pin Diode. PSPX5 detectors are made from 64 silicon strips, 32 in the x direction and 32 in the y direction. The active area of the detector is 9.57 x 9.57 cm^2. In s473, three PSP detectors were used, one in front of the target and two behind the target. The thickness of the PSP in front of the target was 210 μm and the thickness of the detectors behind the target were 314 and 313 μm, respectively. The detector in front of the target had been used in previous experiments and tests beams. The two detectors used behind the target were new, only having been used in the commissioning beam time a few months before.

The PSPX5s are a crucial part of analyzing this experiment, as they supply both position and energy information. This is possible because the silicon surface is made of a resistive material. The position of the hit is determined by the charge distribution on the resistive layer. The position of a hit can be calculated using the following formula:

$$pos = \frac{E_1 - E_2}{E_1 + E_2} \tag{3.1}$$

where E_1 and E_2 are the charges collected at the two ends of one strip. The resistive charge division has a position resolution of $\approx 100\,\mu$m possible with a minimum number of electronic channels needed. To ensure the position measurement is good in two dimensions, this detector was designed to also have a backside with strips perpendicular to the front [Syn18]. Both position and energy measurements are used during the analysis of this experiment, but the energy measurements of the two PSPs behind the target were the most important as this information was used to extract the

unreacted particles after the target to calculate the charge-changing cross sections, which will be discussed in more detail in 5.3.

3.3.4. Fibers

In this experiment, four fiber detectors (Fi10, Fi11, Fi12, and Fi13) were used for tracking heavy particles after GLAD. Each detector has an active area of 50 x 50 cm^2 and is composed of 1024 square fibers 500 μm thick. The fibers are glued parallel to each other on a frame and are set up perpendicular to the beam. Each fiber is connected to two different kinds of read out systems. One side is read out by a Hamamatsu multi-anode PMT H13700. The other side is read out by a Hamamatsu R8619 single PMT. The Hamamatsu multi-anode PMT H13700 consists of 256 anodes and there are two attached to the detector. This requires two neighboring fibers to be attached the same anode. To ensure that each fiber has a unique read out, the other side of the fiber is attached to a different single PMT. There are 4 of these attached to the detector. When an ion hits a fiber, the scintillating material produces a signal that is read out by a PMT. From this, the position of the ion can be determined. Timing and energy information can also be provided by the fiber detectors.

Detectors Fi10 and Fi11 were both placed in the x-direction in the vacuum chamber directly after GLAD. Fi12 and Fi13 were both placed outside of the vacuum at the end of the beam line. Fi12 was placed in the x-direction and Fi13 was placed in the y-direction. Data from the fiber detectors was not used in the presented analysis as tracking information was not necessary.

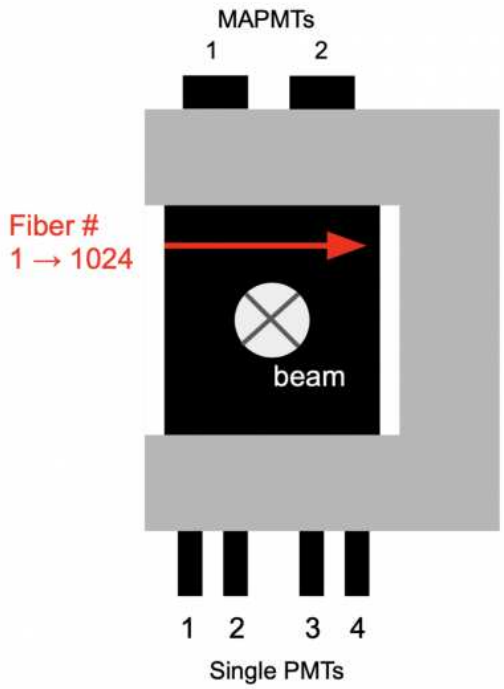

Figure 3.7.: Schematic drawing of the fiber detectors. There are 1024 fibers with two MAPMTs with 256 channels attached to the top of the detector and four SPMTs attached to the bottom for a unique mapping of every fiber. Image created by M. Heil.

3.3.5. TOFD

The next detector used in s473 was the Time of Flight (ToF) wall which is named TOFD [Hei+22]. It is made of two frames, or walls. Each wall consists of two planes that are made of 44 paddles situated in the x direction. The two planes inside one wall are placed offset by half a paddle width from each other to ensure that no particle travels through undetected. The dimension of the paddles are 1000 x 27 x 5 mm^3. The total size of the active area is 1200x800 mm^2. Each paddle is read out by two PMTs, one on the top of the paddle and the other on the bottom.

TOFD is not only used for time measurements, but also for position and energy loss. TOFD was placed at the end of the fragment arm and is the stop time for start detector LOS. TOFD is also used during the beam time to make sure that the beam is at the correct angle based on which paddles are being hit.

The TOFD is placed on a movable table that is capable of moving in both the x and y direction. This is so that during the experiment the TOFD can have so called ”meander runs” where the detector is moved through the beam line in both the x and y direction. This is done to ensure that all points on the TOFD are working properly as every part of the detector is hit by the beam. These runs are

then used during the analysis for calibration of the detector. Position and energy-loss information is used during the analysis of this experiment, but is not used for any final cross section calculations.

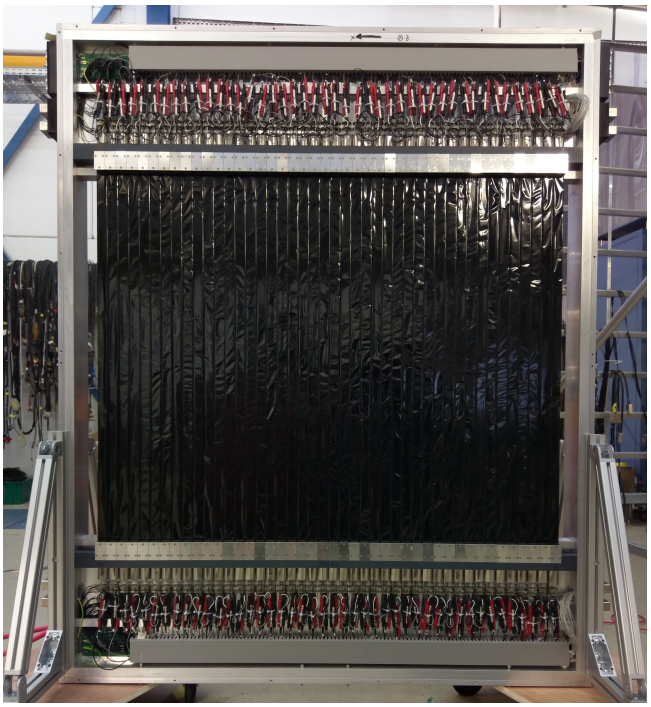

Figure 3.8.: An image of the TOFD. The 44 planes connected to individual PMTs on both ends can be seen. Four of these identical planes are used in s473, with two planes making a ”wall”. The second plane is offset to the first to ensure all particles are detected. Image was taken by M. Heil.

3.3.6. NeuLAND

NeuLAND (New Large-Area Neutron Detector) is the new neutron detector for R^3B collaboration, replacing the previous neutron detector LAND [Bor+21]. NeuLAND is still currently being built. It is planned to be comprised of 30 double planes with 100 submodules each with a size of 5 x 5 x 250 cm^3. The active area for the 3000 submodules will be 250 x 250 cm^2 with a depth of 3 m. NeuLAND is positioned at the zero degree line about 15 to 35 m downstream from the target. At the time of s473, there were 8 completed and operational double planes used.

The main features of NeuLAND are large geometric acceptance, high time and spatial resolution, large multi-neutron reconstruction efficiency, and a high detection efficiency for neutron energies between 100 and 1000 MeV. The time resolution for NeuLAND is $\sigma < 150$ ps. Neutron efficiency for 1n is ≈95% at 400 MeV and for 4n is ≈50% - 70%. This fulfils the ambitious requirements for high efficiency for multi-neutron recognition in R^3B experiments.

Data from NeuLAND was not used in the presented analysis as neutron information was not necessary.

3.3.7. CALIFA

CALIFA (CALorimeter for In-Flight detection of gamma-rays and high energy charged pArticles) is a highly segmented calorimeter that surrounds the target in the R^3B setup [Alv+14; Cab+20]. CALIFA is comprised of 2432 detection units of long CsI TI-doped scintillator crystals with a Large Area Avalanche Photo-Diode based readout, arranged in a barrel shape. CALIFA covers the polar angles of 19°to 140°. CALIFA will detect gamma rays and light charged particles at an energy resolution of 5-6% at 1 GeV (for gamma rays) and an efficiency better than 1% for charged particles up to 320 MeV in the barrel. As of s473, CALIFA has not been completed. Data was taken using seven segments for a total of 448 detection units covering the polar angles between 85°and 35°.

Data from CALIFA was not used in the presented analysis as gamma ray information was not necessary.

3.4. SiPM Detector

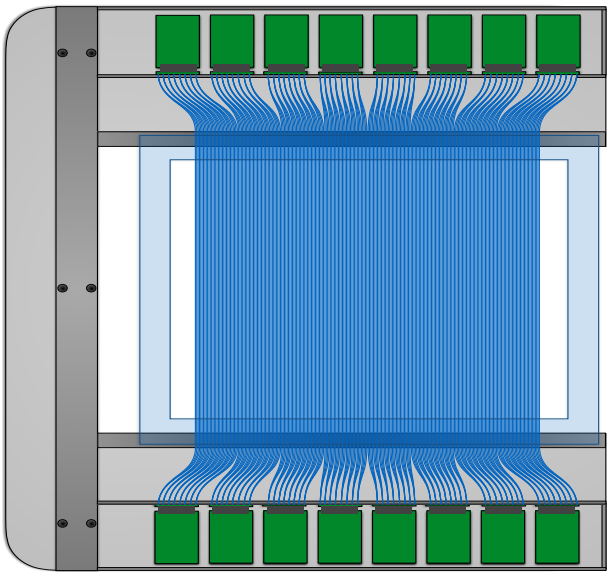

Figure 3.9.: An illustration of the completed SiPM Detector. The fiber sheet is fixed to an acrylic frame (blue transparent). Fibers are attached to SiPMs which then directly connect to the PADI boards. The electronics are attached to an aluminum frame. Figure made by J.Tanaka

In this section, a new fiber detector concept utilizing a silicon photomultiplier (SiPM) readout is discussed. Tracking detectors are a crucial part of the R^3B campaign. One incredibly important area to have a tracking detector is directly after the magnet. The ideal detector at this point is a fine fiber detector with good position resolution and less straggling. However, the PMT read-out system would malfunction at this location due to the influence of the magnetic field. A solution to this problem has been thought out in the form of a fiber detector with a SiPM read-out system. This read-out system is not influenced by magnetic fields and therefore can be used directly behind the magnet. The detector utilized a new combination of electronics: SiPM, Preamplifier Discriminator (PADI) boards, and Clock Time-to-Digital (Clock TDC) boards. There are 2,048 200 μm round scintillation fibers arranged on a flat sheet. The fibers are bundled together in groups of 8 and sorted so that each fiber has a unique mapping between two SiPMs on each side of the detector. In addition, real events from the detector can be determined by detecting the rising and falling edges of the signals from the SiPM at a certain threshold and using the time over threshold (TOT) analysis.

3.4.1. Materials

Fibers

The fibers used to construct the SiPM detector were 200 μm round fibers from Kuraray Co., LTD (Japan) SCSF-78. These fibers emit photons with a wavelength of 450 nm and have a single transparent cladding. The core is made of Polystyrene(PS) which has a refractive index n = 1.59. The cladding consists of Polymethylmethacrlate(PMMA), which has a refractive index of n = 1.49 and a thickness of 4 μm (2% of the diameter). The trapping efficiency of photons emitted to all solid angles in the fiber is 3.1%, which is obtained by considering the reflection angles at the surface of the core.

SiPM

This detector implements the use of SiPM as they are not influenced by magnetic fields. SiPMs work by detecting photons as they interact silicon. The photon has the possibility to be absorbed and transfer energy to a bound electron. If this happens, the absorbed energy causes the electron to move from the valence band to the conduction band, thus creating an electron-hole pair. There are a large range of wavelengths absorbed by silicon, making this a particularly efficient photodetector material. SiPMs work in the breakdown voltage of the Geiger Region, where amplification is given with an electron avalanche.

	SensL Specifications
Active Area	1x1 mm^2
Sensitive Area	64% of the active area
Gain	$3x10^6$
Pixel Size	35x35 μm
Number of Pixels	576
C_D	100 pF
C_C	100 pF
R_C	500 Ω
Applied HV	27 V

Table 3.1.: Specifications of the SiPM Boards

PADI

After the SiPM have created an energy signal it is sent to the PADI boards [Cio+14]. PADI stands for PreAmplifier-Discriminator ASIC chip and is intended to be used as a Front End Electronic that can read out timing information. The first design of the PADI board was called PADI-I and by the time the SiPM detector was constructed, the PADI boards were on design PADI-8, which is the third update. It is named PADI-8 because the number of of channels the ASIC on the board can handle was increased to 8. Since there are two ASIC cards on the PADI board, each board can have 16 channels on it.

The charge signals received from the SiPMs are amplified and shaped, and then are discriminated based on the threshold settings. A timing signal with a leading and trailing edge is then produced. The incoming signals are amplified by a factor of 251 and then go on to the discriminator. If the signal generated is above the threshold, two output signals are generated. The first is generated when the leading edge of the signal goes above threshold and the second is generated when the trailing edge of the signal goes below the threshold. The thresholds need to be set very carefully as to not accidentally cut off good data.

PADI Board Modification

During the initial testing stages of the SiPM detector by S. Scholl, it was discovered that the charge signals from the SiPM output and the PADI boards were saturated. Therefore, a modification was made to the PADI boards to prevent this. R_c=500Ω resistors were placed on all 16 channels of the PADI board to create a connection between the signals and ground.

Clock TDC

After the PADI boards, the next electronics the signal moves on to is the Clock TDC [TDC]. The Clock TDC is a time-to-digital converted developed by GSI. The Clock TDC has a FPGA chip implemented on the board that is able to provide a time resolution better than 400 ps. Each board is capable of digitizing 128 differential signals. The TDC is deadtime free and has a double-pulse resolution of about 10 ns. The TDC has a 12-bit coarse time counter that is operated by a 250 MHz clock and it samples the arrival time for the input signals.

The Clock TDC supplies two different times in order to calculate the time over threshold; the "*coarse time*" T_c and the "*fine time*" T_f. The coarse time comes from the internal clock and is defined as

$$T_c = N \cdot 4ns \tag{3.2}$$

where N equals the number of clock cycles. There is a maximum coarse time window of 4096 bins that the coarse time counter can provide and this divides the times into either leading time T^{lead} and trailing time T^{trail}. This bin number is the number of clock cycles being processed with respect to the trigger timing. The combination of a 12-bit coarse time counter operated by a 250 MHz clock enables a maximum trigger window of 16 μs.

The fine time comes from an additional mechanism built into the TDC to achieve a better time resolution. These times are recorded using a flip-flop mechanism with twelve phase-shifted clocks of the same frequency, which gives each 4 ns clock cycle twelve additional bins. The timing signals are then obtained by

$$T^{lead/trail} = T_c^{lead/trail} - T_f^{lead/trail} \tag{3.3}$$

Since the measurements of the twelve bins from the fine time are not linear, it is necessary to do a time calibration for each measurement. For more information on the calibration of the fine time, please refer to the master thesis of S. Scholl [Sch18].

3.4.2. Fiber Mapping and Construction

The construction of the SiPM detector starts with the fibers glued parallel to each other on a a plastic frame and then the surface of the fibers is covered by a 10 μm light tight black foil. Beyond the plastic sheet, the fibers are separate and can be sorted to the appropriate SiPM.

The board for the SiPM comprised of three parts: a mask, spacer, and electronics. An illustration of the boards can be seen in Fig. 3.10. There are 8 fibers bundled to each SiPM. To ensure a unique mapping for each fiber, the sorting is different on each side, as seen in Fig. 3.11. On the top side of the detector, 8 fibers in a row are connected to the same SiPM. On the bottom side of the detector,

these same 8 fibers are all sorted to a different SiPM. To ensure that the correct fiber was being placed, a magnifying camera was used to easier show which fiber was next. Each mask has 32 holes and accepts 256 fibers, which means that the pattern repeats itself every 64 fibers.

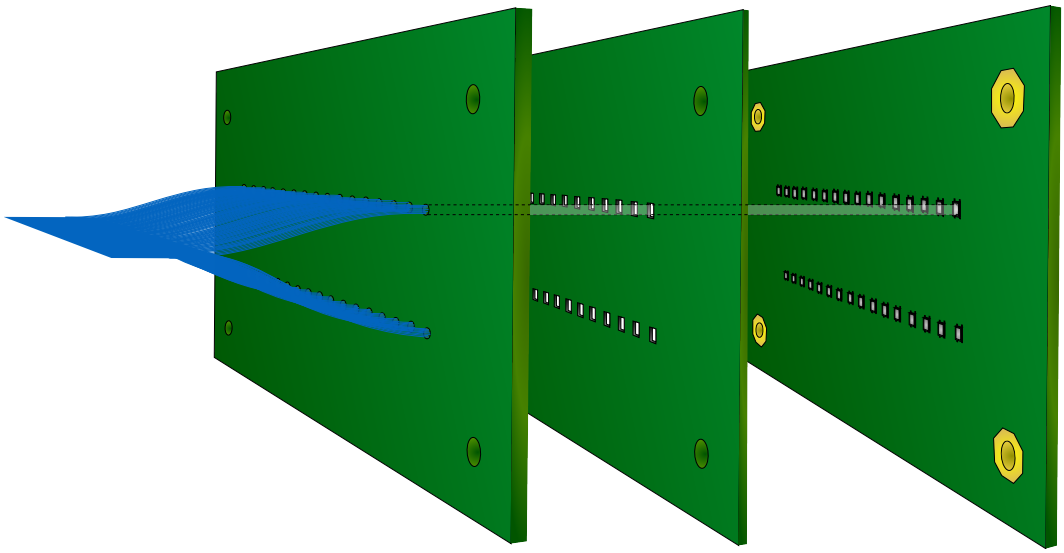

Figure 3.10.: An illustration of the three parts that make up the SiPM Board. The first piece is the mask, which is where the fibers are sorted. It has 32 holes and 8 fibers go into each hole, allowing each mask to accommodate 256 fibers. The middle piece is the spacer, which is needed to compensate the volume of the SiPMs. The final piece has the SiPMs. The gap between the fibers and SiPM created by the spacer is filled with an optical coupling agent. Figure made by J. Tanaka.

After all the fibers have been sorted, they are glued together using Epoxy 301. Once the glue has set overnight, the fibers are cut and sanded until smooth. It is very important for the fibers and mask to be level so that the other pieces of the board fit together properly. The next piece added is the spacer, which is the middle piece seen in Fig 3.10. The spacer is used to give adequate room for the SiPMs that stick out from the next piece. However, this leaves space between the fibers and the SiPMs. This is compensated by a light coupling material. The first build used optical grease to fill in the gap just for testing purposes. However, since the intent of this detector is to be placed inside the vacuum chamber, this is not a long term solution. Earlier this year, the optical grease was cleaned off and replaced with vacuum chamber safe optical silicon pads. Once the fibers and SiPMs are optically coupled, the board is screwed onto the aluminum frame.

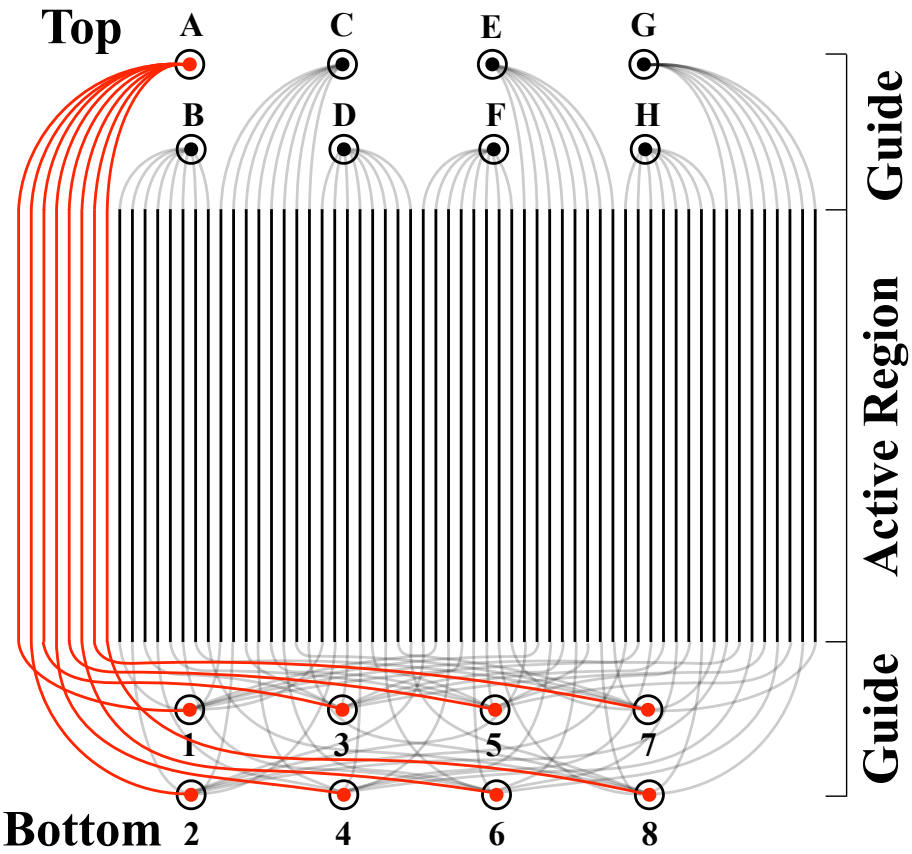

Figure 3.11.: An illustration of the mapping of the fibers.64 for fibers are used as an example, which will cover 16 SiPMs (A-H on the top and 1-8 on the bottom). The red lines show that the 8 fibers connected to SiPM on the top will connect to 1-8 on the bottom. Combination of SiPM1 channel *n* to 8*n* on the top and bottom will correspond to 63*n* to 64*n*, where n is from 1 to 32. Figure made by J. Tanaka.

3.4.3. Testing

There have been multiple test runs of the detector since construction. The first test was done during the experimental campaign in February 2019, the same experiment the data from the rest of this thesis is based on. The detector was placed at the end of the beam line as a ”parasite,” meaning that the detector was running during this experiment, but any data extracted from this detector would not be used for any official analysis. The detector was placed at the beam line height on a platform built from profiles. It was unmovable, so it was not possible to have any sweep runs to test the entire area of the detector.

Some preliminary data from this test run was analyzed and the data is presented below. In Fig. 3.12, the channels read out by the top SiPMs vs the channels read out by the bottom SiPMs can be seen. In the left plot, no cuts have been placed on the data. In the right plot, a multiplicity cut of

2 has been placed on the data, so only the events that saw a hit on both sides of the detector survive. Since all the data left is in the 8x8 squares, its shows that the mapping was correct. In Fig. 3.13, the ToT from all of the different energies used during s473 have been overlaid together. The data came out as expected; the slowest ToT in black is from 400 AMeV, the second slowest is in red from 550 AMeV, the third slowest is in green from 650 AMeV, and the fastest is in blue from 800 AMeV. Fig. 3.14 focuses on the ToT from 400 AMeV. A maximum energy cut has been placed on the data. The low energy peak in black is from the non-maximum energy hits and the high energy peak in red is the maximum energy hits. The separate peaks makes is possible to cut out the noise from the detector, leaving only the physics data. This preliminary analysis shows that the SiPM detector is a viable candidate for a detector to be used in future R^3B experiments, although more tests are necessary.

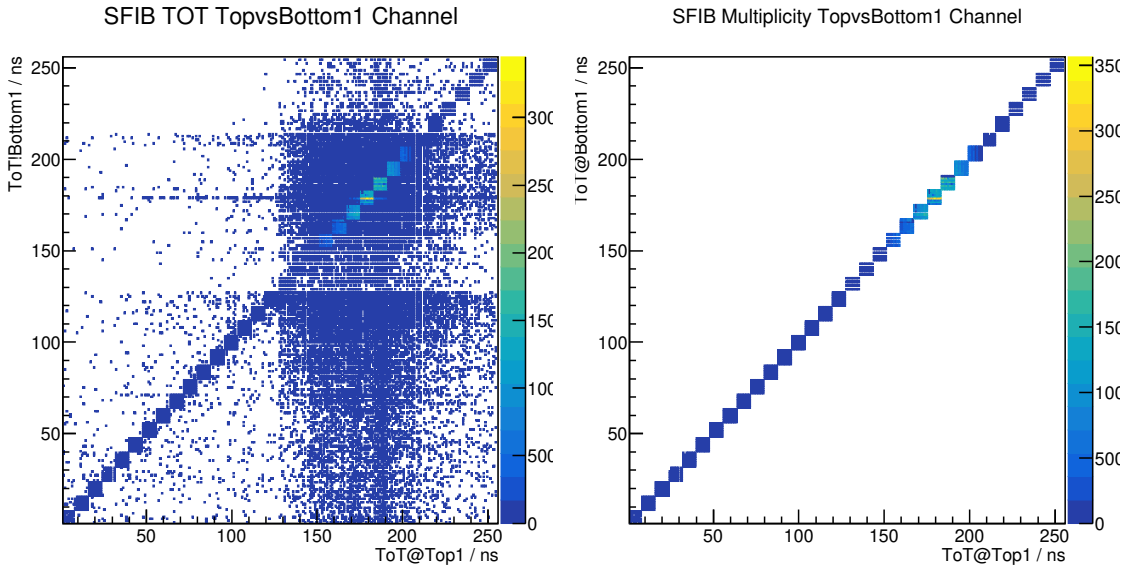

Figure 3.12.: LEFT: Channels from the top SiPMs vs the bottom SiPMs. No cuts are placed on the data. RIGHT: Again channels from the top SiPMs vs the bottom SiPMs. A multiplicity cut of 1 has been applied, and only channels in the 8x8 squares remain, showing the mapping was correctly implemented.

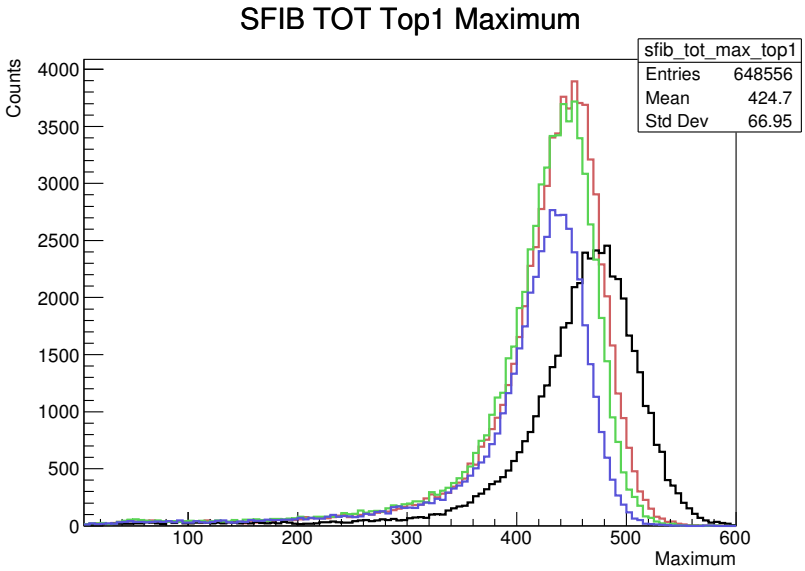

Figure 3.13.: The ToT in ns for the 4 different energies used during s473 from the top SiPMs. As expected, the lowest energy, 400 400 AMeV has the highest ToT in black, then next 550 AMeV in red, then 650 AMeV in green, and finally 800 AMeV with the smallest ToT in blue.

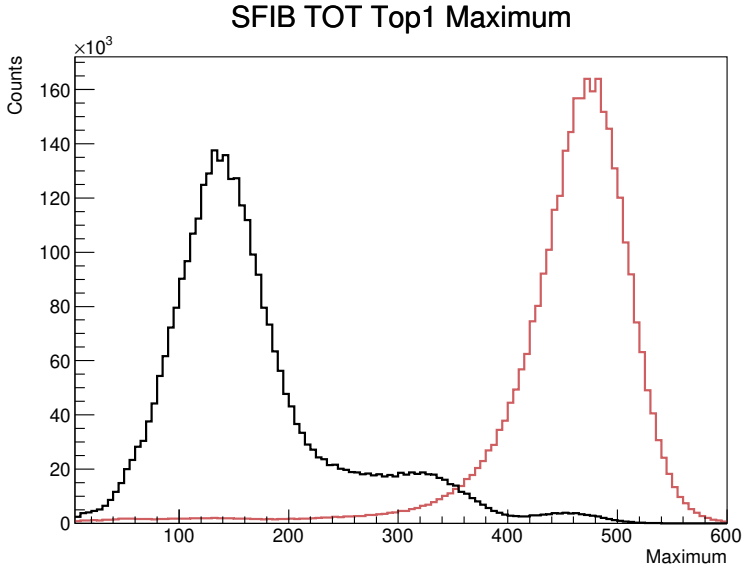

Figure 3.14.: The ToT in ns for the top SiPMs. A maximum energy cut was applied to the data and the red peak represents the maximum energy while the black peak represents all other energies and is the noise from the electronics. A distinction between maximum energy and noise can be seen, allowing for the noise to be mostly cut away leaving the real events.

The second test for the detector was done in February of 2020 during the experimental campaign of a collaborator using neutron rich Ca isotopes. Again, the detector was placed at the end of the beam line as a parasite. This time, however, the detector was placed on the movable platform that the ToFD is placed on. This allowed for the entire detector to be placed in the beam line to ensure all points of the detector were working efficiently. Online analysis of the data in real time did not present any issues within the detector; all areas of the detector appeared to be working as expected.

Based on the successes of the previous testing, it was decided that the detector would be used in the experiment that occurred in April 2021, which was the follow up experiment to the one presented in this thesis. Since the detector would be placed inside of the vacuum, the optical grease used between the the fibers and SiPM was no longer suitable. The grease was cleaned off and replaced with silicon pads. To ensure that the coupling was strong, the detector was first tested with a laser. A light-tight sleeve was built and the laser was shined on just one board to start.

Unfortunately, issues were discovered during the laser testing phase. The main thing looked for in the data while analyzing were matching leading and trailing times. As these signals are created together in the PADI board, there should always be a pair. However, this match was missing when the test data was analyzed, and it looked quite noisy, as can be seen in Fig. 3.15. As this is presented in log scale, there are many expected matches in red, but there are many mismatched counts as well.

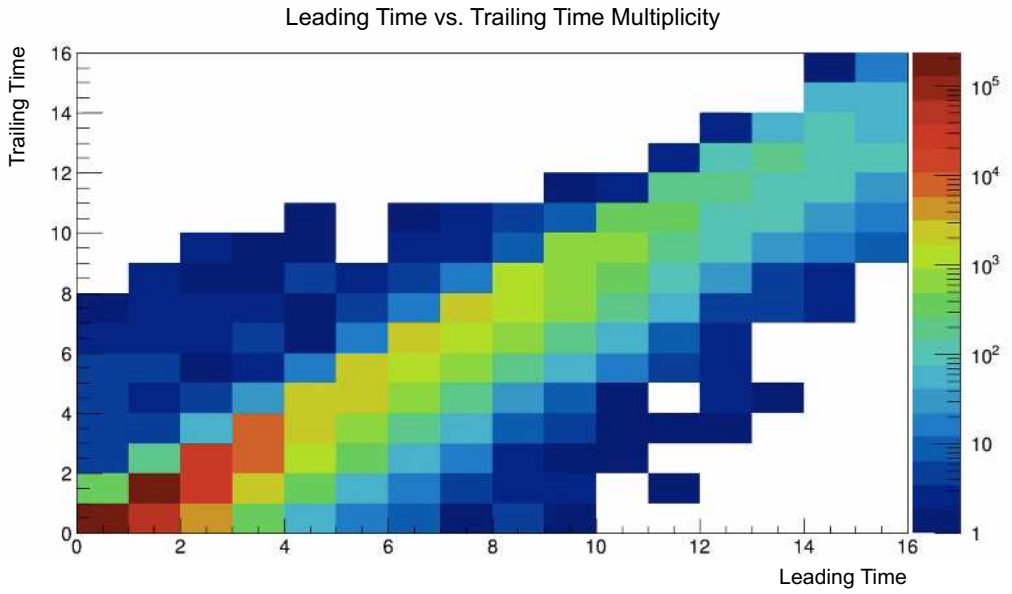

Figure 3.15.: Leading vs. trailing time multiplicity for the SiPM detector from laser testing. All leading times should have a matching trailing time, but as the plot shows, there are uncorrelated times. This suggests a problem within the readout of the detector.

Some ideas for the problem were discussed. Since this issue had not been present in the previous

testing of the detector, one leading theory is that the testing was not conducted in a light-free environment, and the discrepancy therefore came from light interacting with the detector and creating noise. Since this problem could not be quickly understood, the decision to leave the SiPM detector out of the experiment was made. No further tests have been done to determine the cause of the issues, but any attempts should be done in a clearly light-free environment to ensure that this variable is not the cause of the problem.

3.5. Targets and Energies

3.5.1. Targets

For s473, 7 different targets were used as well as runs without any targets. In the table below, it can be seen which targets were used at each energy. The carbon targets are ^{12}C and the plastic targets are CH_2. The exact dimensions of the carbon targets can be seen in Tab. 3.2.

Density g/cm^3	Thickness g/cm^2	Length cm
1.84	1.002984	0.5451
	1.985912	1.0793
	4.034752	2.1928

Table 3.2.: The exact density, thicknesses, and lengths for the carbon targets used in s473.

For simplicity, 1.002984 g/cm^2 will be referred to as 1 g/cm^2, 1.985912 g/cm^2 as 2 g/cm^2, and 4.034752 g/cm^2 as 4 g/cm^2.

Energy (AMeV)	C 1 g/cm^2	C 2 g/cm^2	C 4 g/cm^2	CH_2 1.2 g/cm^2	CH_2 2.3 g/cm^2	Pb	Empty
400	X			X			X
550	X	X		X	X		X
650	X	X	X	X			X
800	X	X	X	X	X	X	X
900		X	X		X		

Table 3.3.: All of the targets used during the s473 campaign. Thicker targets could not be used at lower beam energies as the beam's energy loss would be too great to make it past the target. Due to unfortunate circumstances with magnet, there was not enough time to test all of the targets at 900 AMeV.

The intention of s473 was to use carbon and proton targets. Since proton targets are not possible, the carbon contribution is to be subtracted from the CH_2 target. By measuring with both C and

CH_2, an uncertainty of <1% can be achieved in the data. The proton target is more sensitive to the neutron distribution at low energy, and vice versa at high energy. Since the C target is N=Z, it will show a characteristic behavior for the different targets as a function of energy in the cross sections. The lead target is used for the Coulomb contribution, which is not presented in this thesis.

3.5.2. Energies

In Tab. 3.3, the energies are listed as 400,550,650, and 800 AMeV. These are the energies as the beam enters Cave C, but the beam will experience energy loss as the beam interacts with the detectors and the target in the beam line. Tab. 3.4 shows the precise energy as it enters the target, when it is halfway through, and as it leaves the target.

Start Energy in AMeV	Target Thickness in g/cm^2	Energy in AMeV Front	Energy in AMeV Middle	Energy in AMeV Back
400	1	394.093	364.223	333.123
550	1	544.828	519.02	492.695
	2	544.828	493.227	439.314
650	1	645.122	620.899	596.344
	2	645.122	596.839	547.116
800	1	795.414	772.749	749.892
	2	795.414	750.357	704.479
	4	795.414	703.011	606.628

Table 3.4.: The beam energy as it goes through every target at each energy. The middle distance for 1 g/cm^2 is 0.27255 cm, 2 g/cm^2 is 0.53965 cm, and 4 g/cm^2 is 1.0964 cm. Energy loss is calculated using the GSI program ATIMA [ATI].

3.6. DAQ

In order for the signals from the detectors to be usable, a Data AcQuisition (DAQ) system is needed to process and record the data. The DAQ was originally created based on the Multi-Branch System (MBS) [MBS], but as of s473 a newer system called drasi was in use for most of the detector systems. Drasi is a networked program consisting of several parts [dra]. A typical configuration will consist of the following parts:

- Readout program (on each readout mode)
- Event builder
- Log message writer
- Monitoring programs
- Monitor dump to time-series graphing

- Command line control program

Most of the detector systems in the R^3B setup are a part of the Main DAQ group except for a few of the detectors, such as NeuLAND and Califa, that have their own DAQ system. However, every DAQ group is under the same Time-order that collects and sorts events and writes the events to storage. The data is saved directly to long-term storage from the DAQ.

The data is stored in files in the List-Mode-Data (LMD) format. At the time of s473, all LMD files were saved on the R^3B server nyx (data can now be found on the server lustre). Whether or not an event gets saved is determined by the trigger logic.

The events accepted by the DAQ should be in coincidence with each other. In order to determine if the events are in coincidence, the central trigger logic receives signals from the individual detectors. An accepted trigger is when there is no deadtime and it is a good set of detector signals. Once a trigger is accepted, it is sent to the ”Master Start.” Typically the trigger is controlled by LOS.

Signals that have been sent to the Master Start are then sorted into different trigger patterns, called Tpat. The Tpats are based off of signals received from the different detector signals and other auxiliary signals. When triggers are generated from different detectors, the combination of signals are assigned to a Tbit number. Tbit is the Tpat variable expressed in decimal form (2^{Tbit-1}). The distribution of Tpats from s473 expressed as Tbit values can be seen in Fig. 3.16. Selected triggers from s473 can be seen in Table

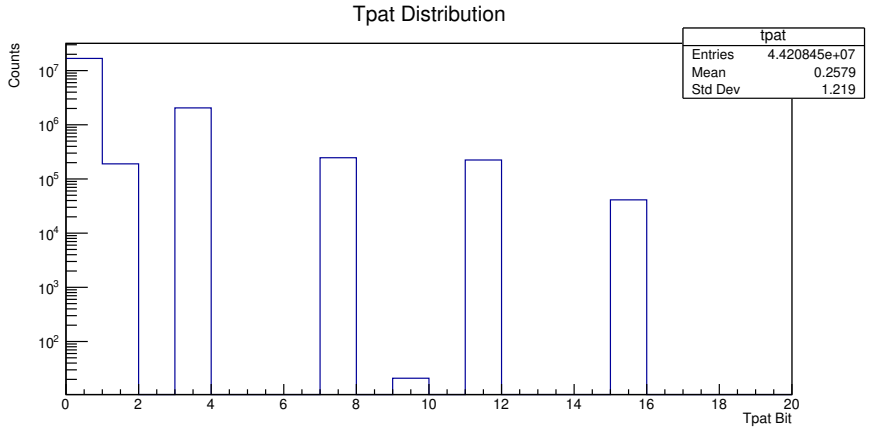

Figure 3.16.: The patterns are recorded in a binary system. There are many events in the zero Tbit due to a CALIFA trigger. These triggers are not used for the analysis of other detectors.

Tpat Value	Tbit Value	Trigger	Spill-On	LOS!ROLU	TOFD	NeuLAND
1	1	MinBias	1	1	-	-
2	3	Fragment	1	1	1	-
3	7	NeuLAND	1	1	1	1

Table 3.5.: Selected triggers (minimum bias, fragment, and neutron) produced by the trigger logic based on the coincidences between detectors. All triggers shown here require the spill to be on. The minimum bias trigger looks for a signal in LOS, but not in ROLU. The fragment trigger looks for a signal in LOS but not ROLU, and in the TOFD. The neutron trigger looks for a signal in LOS but not ROLU, the TOFD, and NeuLAND.

These Tpat categories can then be used during the analysis phase to easily cut out unwanted data. This is very important for this experiment because the cross sections are to be calculated using the ratios of the counts from the incoming beam and the counts from the unreacted beam once it has gone through the target and the rest of the experimental setup. The numbers used here need to be extremely accurate or the cross sections will off by large percentages. This will be discussed further in the following chapters. Since only the counts are being used to calculate the cross sections instead of the more traditional method of using a specific reaction channel, no downscaling was used during this experiment.

4. Calibration and R^{3}BRoot

After the data is stored in LMD files, it is placed in the so-called UCESB (Unpack and Check Every Single Bit) level [UCE]. UCESB is capable of reading several types of data formats and can also write files to ROOT. It is a program used to generate data unpackers. Here, the data is still raw, meaning the data has not been converted to physics units yet. In order to get the data to physical units and extract any meaningful physics information, the detectors must go through their own individual calibration procedure. Each detector is calibrated individually using the R^{3}BRoot analysis framework. Once a detector has been calibrated completely, it can be used in conjunction with the other detectors in the experimental setup. The following chapter will discuss the different data levels and calibration of LOS, the PSPs, and the fibers using R^{3}BRoot. Calibration of the TOFD was performed by J. Simon and NeuLAND by D. Jelavić Malenica.

4.1. R^{3}BRoot

R^{3}BRoot is the simulation and analysis framework for all R^{3}B experiments [Ber11]. R^{3}BRoot uses the ROOT framework to unpack and sort data into trees [ROO]. It is based off of the FairRoot [Ber+08] base library used across the different experiments at GSI. The FairRoot base library provides a common data structure that can be used for simulation and analysis based on Root Trees, a common geometry description, detector base class, and many other features. The R^{3}BRoot implements the specific pieces needed only for R^{3}B experiments, such as detector geometry and materials, magnetic field maps, event generators, database connectivity that can handle multiple experimental setups, and more. R^{3}BRoot is typically coded in the language of C++, but other languages are possible to use. The specific data levels and calibration routines using R^{3}BRoot will be described in the following sections.

4.2. Data Levels

Almost all detectors follow the same data levels in R^{3}BRoot. Only the PSPs have an additional level, which will be mentioned below. The levels are as follows:

MAPPED: Mapped is the lowest level of data and is provided by ucesb. Here, the data is converted from the ucesb data structure to the R^{3}BRoot structure. All units are still arbitrary from the electronics.

PRECAL: Precal is a special level of calibration that only exists for the PSPs. It is an additional position calibration and will be described in more detail in Sec. 4.4.

CAL: Cal is an intermediate step of calibration that all detectors have between Mapped and Hit. It supplies some information regarding position, energy, and time depending on the detector, but is generally not converted to physical units yet. It is the calibration of each electronics channel individually. A transition of the times from Mapped level to Cal level using Fiber 10 can be seen in Fig. 4.8 (Mapped) and Fig. 4.9 (Cal).

HIT: Hit is the final level of detector calibration. It is the combination of information from all channels of a given detector. The channels within the detector are now synchronized. All energies, positions, times, etc should now be in real physical units. Energies are in MeV, times are in ns with respect to a defined zero, and positions are all in cm. A transition of Channels (Cal) to Fiber ID (Hit) using Fiber 10 can be seen in Fig. **??** (Cal) and Fig. 4.10 (Hit).

TRACK: This is the final level for the data after every detector is calibrated individually. Using the positions of the detectors in the experiment, they can now be synchronized together. Tracking information for s473 was not needed for this analysis and is therefore not presented in this thesis.

4.3. LOS

The LOS calibration is preformed in two different steps, Mapped2Cal and Cal2Hit. The basic framework for these steps are already in R^{3}BRoot and were created by A. Kelic-Heil.

At the mapped level for LOS, the available information is the following:

- Detector

- Channel
- Type
- Coarse Time
- Fine Time

Information for Detector, Channel, and Type all come directly from the electronics. Detector has all information in the first bin for one detector. Channel has a bit more information, it is for channels 1-8 and shows which PMT was hit. The coarse and fine time measurements both come from the FQT read-out system. The time signal is split corresponding to the time relative to the next clock cycle (fine time) and to the number of clock cycles (coarse time). The range of the clock cycle is 7.8 ps, so to convert the fine time to ns, it is divided first by the clock cycle, and then again by 1000. For all hits, the script searches the list of detector hits. When a hit matches, this item is added. If it does not match an existing hit, a new hit is created. To ensure there are not multiple hits, the script looks for hits in coincidence and will skip if one is found.

In order to get to the CAL level, parameters from the Mapped level need to be generated. Since LOS is before the target, the beam should be the same coming through regardless of the run, so any run can be used for calibration. Between the Mapped and CAL levels, the coarse and fine times are calibrated to leading and trailing times in nanoseconds.

Parameters for the HIT level were not generated, but the script will still convert to physical units. Instead, the already existing code made by A. Kelic-Heil was implemented to get the following information:

- Detector
- Time in ns
- Position X in cm
- Position Y in cm
- Deposited Energy

The leading and trailing times from the CAL level are combined to create just one time in nanoseconds. This is done bu either taking the time average over 4 signals (right, top, left, and bottom) or over the two opposite signals (right and left or top and bottom). The average of leading times obtained by TAMEX of adjacent channels are used to create the positions for X and Y in cm. The final position calibration of LOS can be seen in Fig. 4.1. The energy is measured using a principle of integrated Time-over-Threshold (ToT). A Charge -to-Time-Digital-Converter (QDC) board is included in the FQT, which is where the input charge signal is shaped and integrated and the signal integration

enables linearity of charge measurements. ToT can then be obtained from subtracting the trailing time from the leading time of the integrated signal.

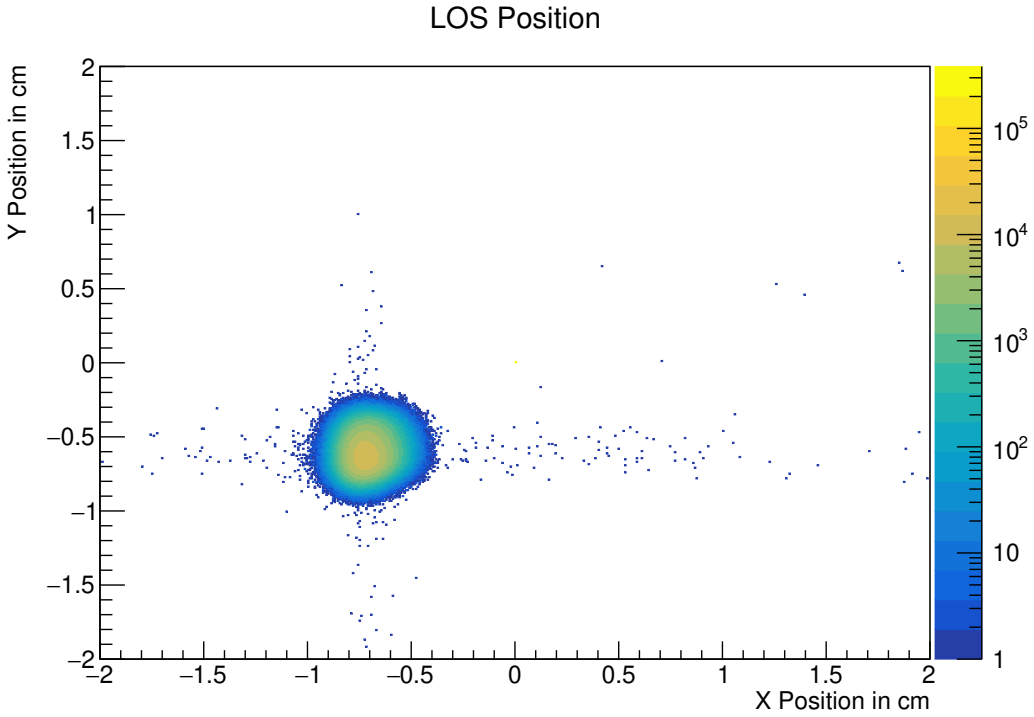

Figure 4.1.: The calibrated X and Y position for LOS in cm from the hit level. An accurate representation of the beam spot before it goes through any detector or target.

4.4. PSP

The PSP calibration is preformed in three steps, Mapped2Precal, Precal2Cal, and Cal2Hit. The basic framework for these steps are already in R^{3}BRoot and were created first by I. Syndikus [Syn18] and then the class was recreated by M. Holl. The calibration was initially done using the process created by I. Syndikus, but was later redone from the precal2cal step with the new class created by M. Holl, so these are the methods that will be discussed below.

4.4.1. Data Structure

Before going into how the calibration is done, a few remarks about the data structure should be mentioned. The data from the PSPs is collected in a unique way. As mentioned in the previous section,

the PSPs are comprised of 32 strips in the x direction and 32 strips in the y direction each with their own channel read-out. The 64 channels are fed-through by two mesytec MPR-32 preamplifiers that have an energy range of 1 GeV placed on the outside of the chamber. Using this feed-through, the channels of the detector can be mapped to the channels of the preamplifier. The differential output from the preamplifiers were connected to the Front-End Board with optical link EXtension 3b (FEBEX3b) ADC, which is read-out by the DAQ. General information about the FEBEX Software can be found on GSI's website [feb].

When a charge is collected it is converted to a signal proportional to the original charge by the preamplifier with a pulse height determined by the FEBEX3b ADC. This is done by applying a moving average filter to the incoming pulses. The pulse height signal is summed up over two time intervals where the length is $w \times \Delta t$. The time intervals start at two different times, t_1 and $t_2 = t_1 + (w + g) \times \Delta t$ where $g \times \Delta t$ is the time span between them and Δt is the time between two pulse shape samples. For the FEBEX3b ADC $\Delta t = 20\,\text{ns}$. The difference of the second and first sum is the height of the filter signal as a function of the time t_1 for values of the interval length w and the time span g between the intervals.

The FEBEX3b also provides signals to the DAQ. An additional filter will determine the pulse height and so long as the data is above a specific threshold, the data is recorded. During s473, the trigger for the PSPs came from the master start. A new method to read-out the data in hopes of better resolution was also used during s473. The FEBEX3b filter was split into two, one for energy and one for position. Each PSP detector used essentially became two separate detectors and were individually labeled. The first PSP is therefore labeled $PSPX1$ and $PSPX2$, the second PSP is $PSPX3$ and $PSPX4$ and the last PSP is $PSPX5$ and $PSPX6$. All of the odd named detectors are read-out from the "energy" filter, which is the longer filter with $w = 200$ and $g = 15$. The even named detectors are read-out from the "position" filter, which is shorter with $w = 10$ and $g = 10$. It was determined by S. Storck-Dutine that the position filter had better resolution for both energy and position when using a heavy beam, so only this filter is used during analysis. In addition to the multiple filter read-outs, each filter saves the data from the front and back of the detector separately. Therefore, the PSPs will be labeles as follows for the remainder of this thesis:

- PSPx1 and PSPx2 $\rightarrow$PSP2
- PSPx3 and PSPx4 $\rightarrow$PSP4
- PSPx5 and PSPx6 $\rightarrow$PSP6

In the new class, the data is called $PSPX2\_xHit$ or $PSPX2\_yHit$. It is important to note that X and Y do not refer to direction of the strips, but rather X means the front of the detector and Y means the back of the detector. Combining the data from X and Y gives the complete data set.

4.4.2. Initial Position Calibration

The first step in calibrating the PSPs is called Mapped2Precal. On the mapped level, the available information is strip number and energy. The strip number ranges between 1-33 for the front of the detector and between 34-65 for the back of the detector. The energy is given in ADC channels. The energy can either be positive or negative depending on the polarity of the signal and the side of the detector, respectively. Ucesb has already created a mapping of the electronic channel number to a meaningful physical channel number. This first level of calibration is done to match the two channels belonging to one strip. It is possible that the position calculated from Eq. 3.1 will not be zero for hits in the middle and a gain factor applied to the measured energy at the end of one strip is necessary to correct the position. The same run is used to calibrate all three PSP detectors. Since PSP4 and PSP6 are behind the target, the run picked does have an impact. A run using the Pb target at 800 MeV/nucleon was chosen for the calibration run.

The method of calibration is to use what are called ”interstrip” events. Since the detector has two sides, X and Y, that receive the ion, it is possible to look for events that hit in between the strips of the detector on of the sides. This is done by gating on a multiplicity of 1 from the strip tree for either the front or the back, and then gating on a multiplicity of 2 for the other side. This will create a plot with a crooked grid structure, as can be seen in Fig. 4.2.

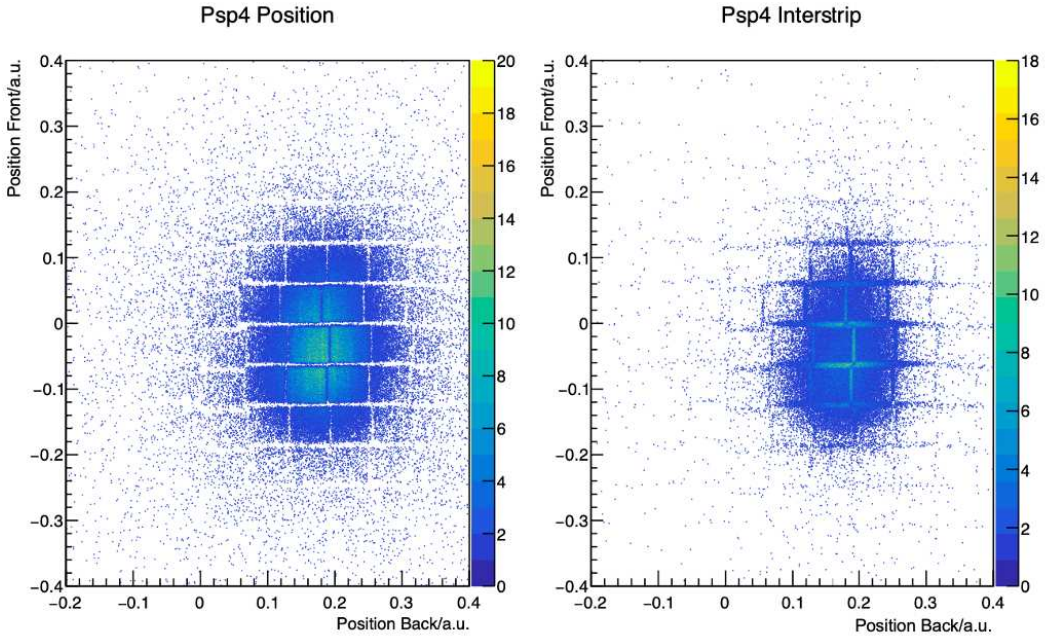

Figure 4.2.: At the mapped level, the gain factor has not been applied to the measured energy yet leading to incorrect positions. The visible ”grid” is the space between the strips and should be straight.

Interstrip events are selected by gating on events of neighboring strips that both see a hit in one event on one side but only passed through one strip on the other side. To further clean the spectrum, a cut to ensure the measured energy is the same on both sides of the detector is also used. A gate is placed on the strips that the beam is centered on to ensure the data analyzed is the beam. Individual plots for all the strips are generated and for strips that collected enough data, a Gaussian is fit to the peak. The gain parameters that come from the Gaussian fit are applied to the Mapped data, correcting the position, as can be seen in Fig. 4.3. The positions are however only calibrated to arbitrary units in this step, they are calibrated to physical units in the final step described below.

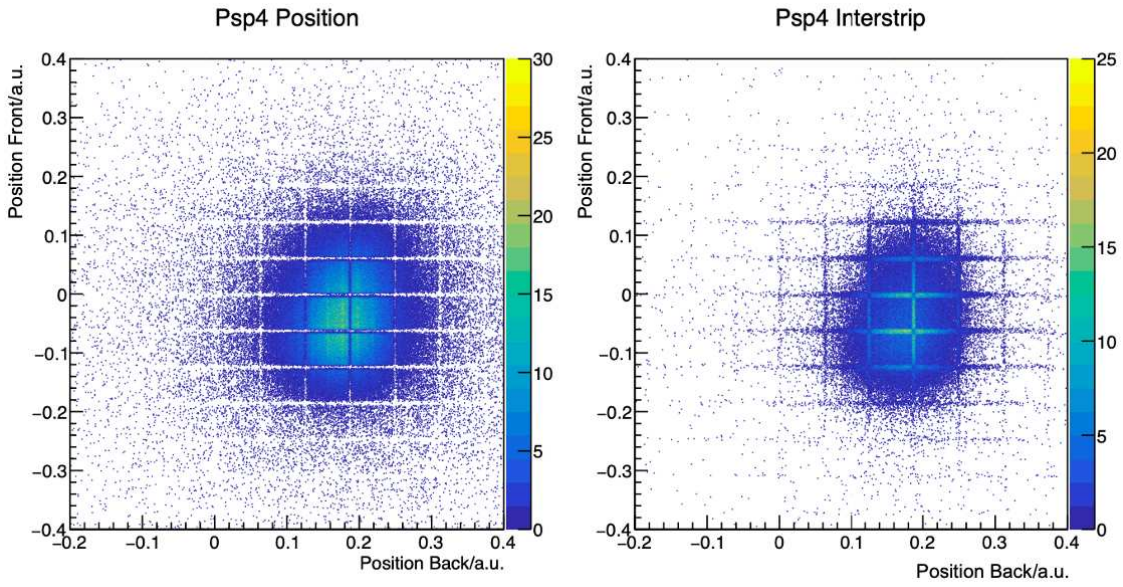

Figure 4.3.: After the gain factor has been applied to the measured energy and the calibration is complete, the interstrips can clearly be seen in a correct grid pattern.

4.4.3. Energy Calibration

The next step in the calibration is called Precal2Cal. On the precal level, the available information is strip number, energy 1, and energy 2. Strip number does not change between the mapped and precal levels. Energy is split into two separate leaves because the energy is read-out on both ends of the strip. This step of the calibration focuses on the energy and combining the two energies into one value and converting to physical units. In the previous step, the calibration was done by matching the gains of the read-out channels within one strip. For the precal2cal step of the calibration, the gain matching is applied to each strip in order to match the sum energy of all of the strips. Only events that have an ion passing through one strip on the front and back are selected to be used for the calibration.

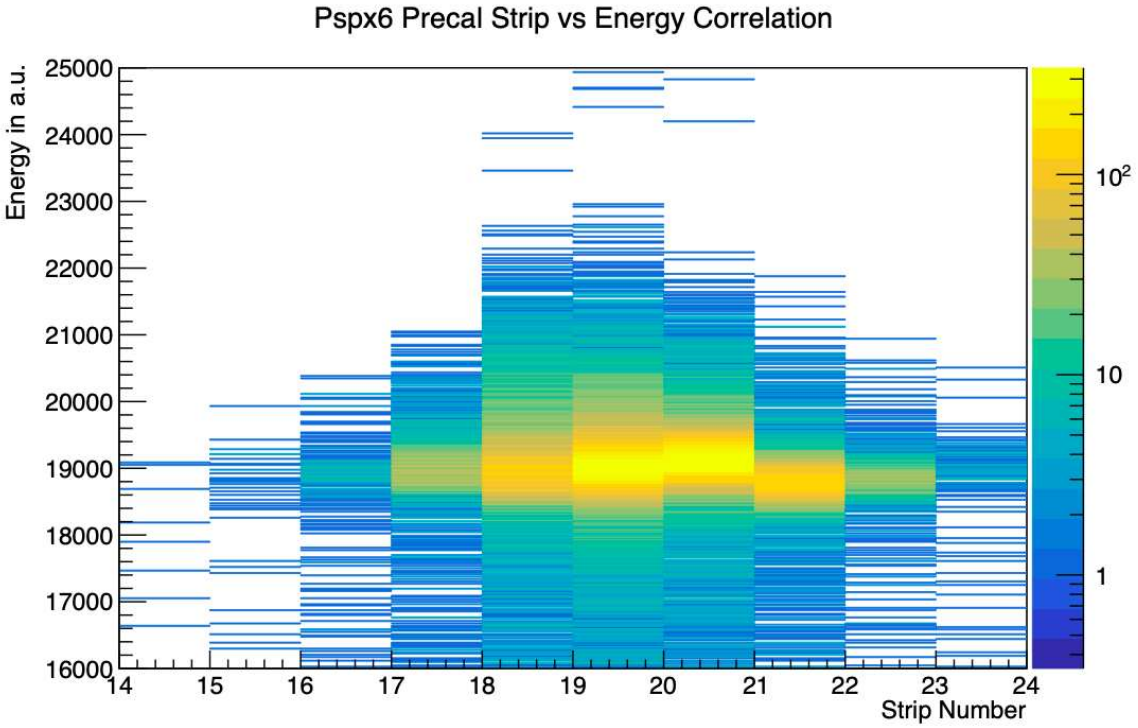

(a) Mapped Level

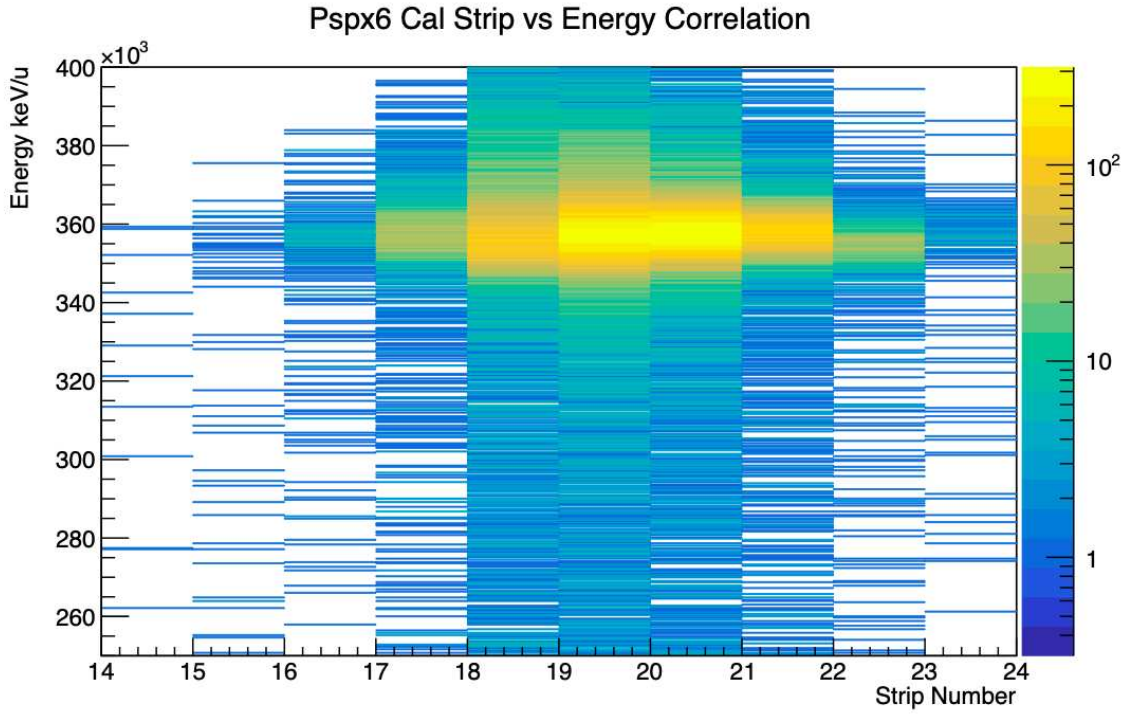

(b) Cal Level

Figure 4.4.: Plot (a) shows the energy of PSP6 uncalibrated. The energy in the individual strips are mismatched and the energy is given in arbitrary units. Plot (b) shows the energy after gain parameters have been applied. The energy in the individual strips are no longer mismatched and the energy is now given in units of keV.

The calibration is done using the same method as in Mapped2Precal, fitting a Gaussian to the peaks of strips with many events and applying these gain parameters to the data. Fig. 4.4 shows the correction from applying the gain parameters. Units for the energy are now in keV.

4.4.4. Final Position Calibration

The final step of calibrating the PSPs is called Cal2Hit. The available information on the Cal level is strip number, position in arbitrary units, and the calibrated energy from the previous step. This calibration step will convert the position from arbitrary units into cm. Again, interstrips are used because they have a known set distance between them as each strip is 2.99 mm wide. Again, each peak is fit with a Gaussian and then a TGraph is used to plot the points on one axis and the distance between the strips on the other axis as can be seen in Fig. 4.5 and a linear fit is applied. The slope from the linear fit are then applied to the data. Fig. 4.6 shows the position change from arbitrary units to cm. The PSP data is now completely calibrated and the available information at the Hit level is energy in keV and position in cm.

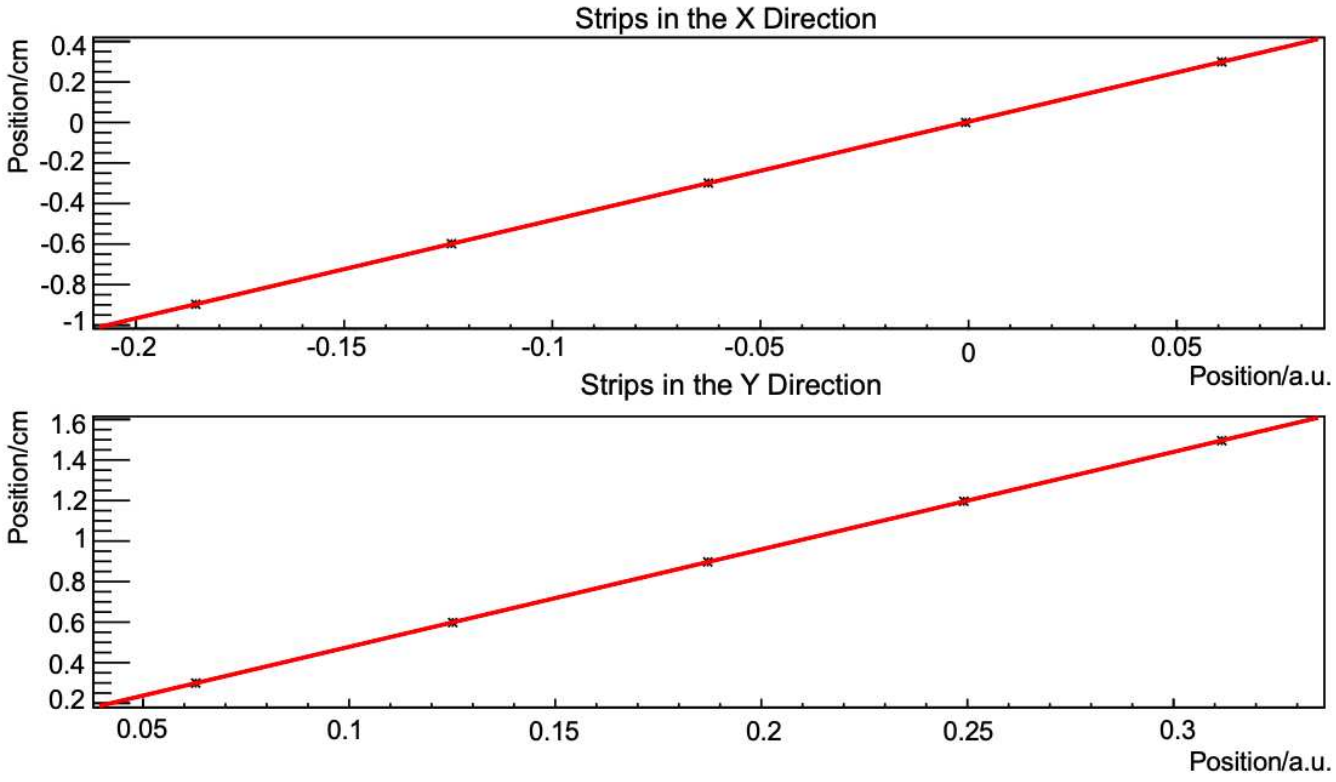

Figure 4.5.: Shows how the arbitrary units are converted into cm from the Cal level. The location of the arbitrary units are matched to the known distance and location of the strips and then a linear fit is applied, seen in red. The slope of the linear fit is applied to the data and the units are converted to cm.

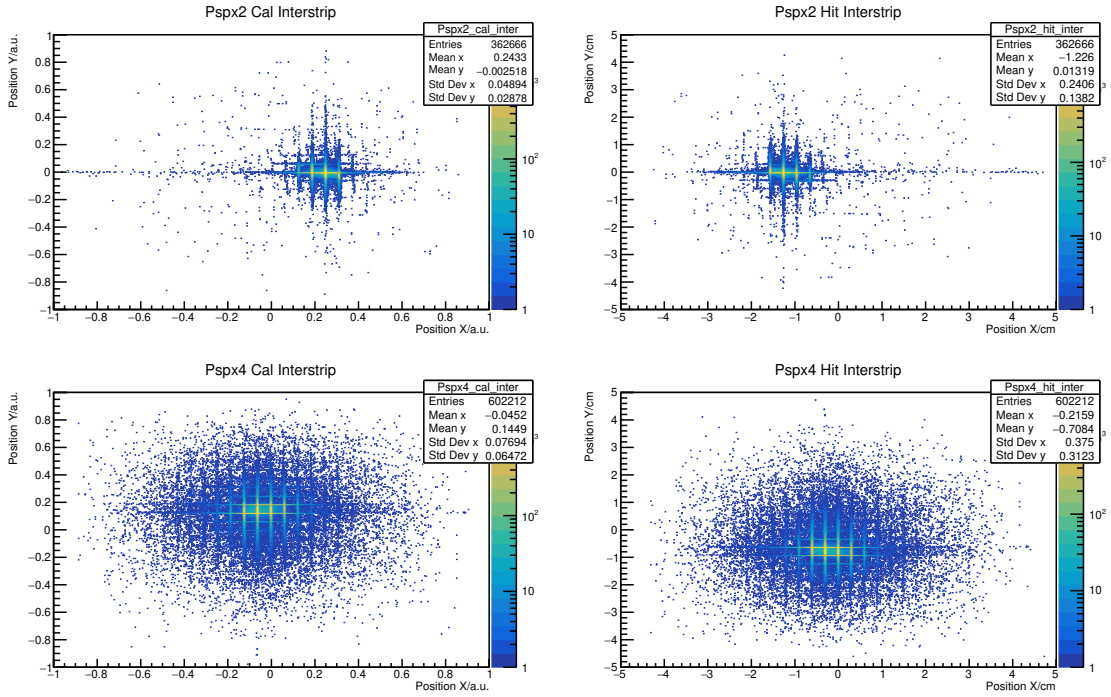

Figure 4.6.: Final position calibration plots for PSP2 (top) and PSP4 (bottom) using interstrips. Both plots on the left show the interstrip events with the first part of the calibration applied still in arbitrary units. Both plots on the right show the offset parameters applied to the data and the data is now in cm.

4.5. Fibers

The fiber calibration is preformed in a very similar way as LOS, in two different steps, Mapped2Cal and Cal2Hit. The basic framework for these steps are already in R^{3}BRoot and were created by M. Heil.

The first step of the fiber calibration is called Mapped2Cal. At the mapped level the fibers have very basic information. The information given is which side of the detector saw a hit, the channel number, if the time signal was a leading not trailing edge, and the coarse and fine time. The channel number is for both the SPMT and the MAMPT. The data from the two PMTs is still separate at this point, so there are 512 channels for the MAMPT and 4 channels for the SPMT, as can be seen in Fig. 4.7. The figure is shown in log scale because the large number of counts in the 4 SPMTs, which are seen in channels 1 to 4. As the data shown is from a physics run, the large peak staring around channel 200 is the unreacted beam, with reacted particles in the channels to the right.

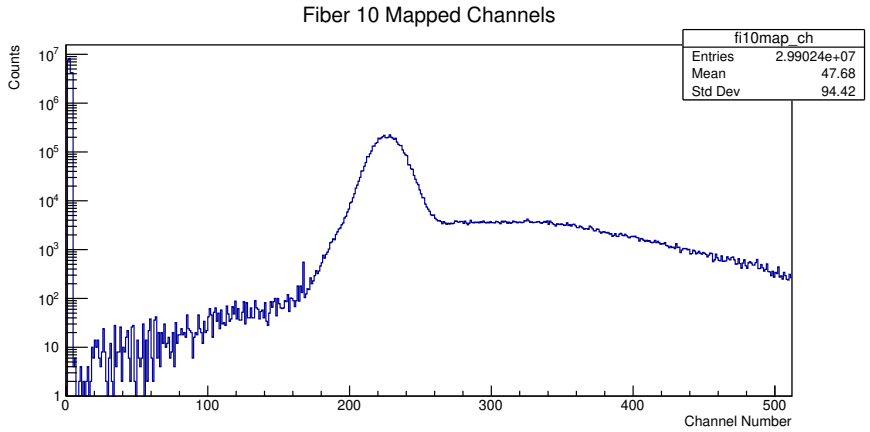

Figure 4.7.: Channels of Fiber 10 at the Mapped level. The channels come directly from the electronics and the SPMT data has not yet been combined with the MAMPT data to make every fiber distinguishable, so only 512 channels are available as opposed to 1024 fibers. All of the data from the SPMTs is placed in channels 1-4. Plot is from a run with the 1 g/cm^2 C target at 550 AMeV.

The information on leading, trailing, coarse and fine time is all in arbitrary units and comes directly from the Clock TDC. More information on the Clock TDC can be found in Sec. 3.4.1.

In order to get to the Cal level, parameters from the Mapped level need to be generated. To generate the parameters a sweep run is needed. A sweep run is taken during the experiment after all of the thresholds and voltages are set. The fiber detectors are all on their own movable platforms so that the detectors can be moved during the experiment if needed. The platform is long enough that every fiber on the detector can be moved into the beam. A sweep run is where the detector is moved from one side of the platform to the other so that every fiber is exposed and therefore parameters for every fiber channel can be generated. In s473, only one complete sweep run was performed for the fibers at 400 AMeV, so this is the run used for the calibration of all the fiber detectors for the entire experiment.

The information available at the CAL level for the fibers is as follows:

- Side
- Channel
- Is Leading
- Time in ns

Side is either 0 or 1 and is representative of which PMT read-out the data; 0 is for MAPMT and 1 is for SPMT. Channel and Is Leading are still the same as it is in the mapped level. As an example of how the data looks on the mapped level, the separate coarse and fine times can be seen in Fig. 4.8.

However, at the CAL level coarse and fine time have been combined to create a time in nanoseconds (ns). The script will ask for SPMT and MAPMT fine time separately since the signal for fine time for the SPMT comes from Tamex and MAPMT comes from the Clock TDC, and then sorts the fine time accordingly. The fine time is then calibrated by using the raw signal from the Clock TDC. The MAMPT signal is considered first, and only signals greater than 0 and less than the Clock frequency. Calibrated time in ns is then filled by $T_{coarse} \cdot ClockFreq - T_{fine}$. The SPMT signal is then considered with the same method. Only signals greater than 0 and less than the Tamex frequency. Then the time in ns is additionally filled by $T_{coarse} \cdot TamexFreq - T_{fine}$. After this process is completed, the data is now converted to ns and the spectra for this can be seen in Fig. 4.9. Timing information from the fiber detectors was not used in this experiment, the figures are just examples to illustrate the differences between mapped and cal level.

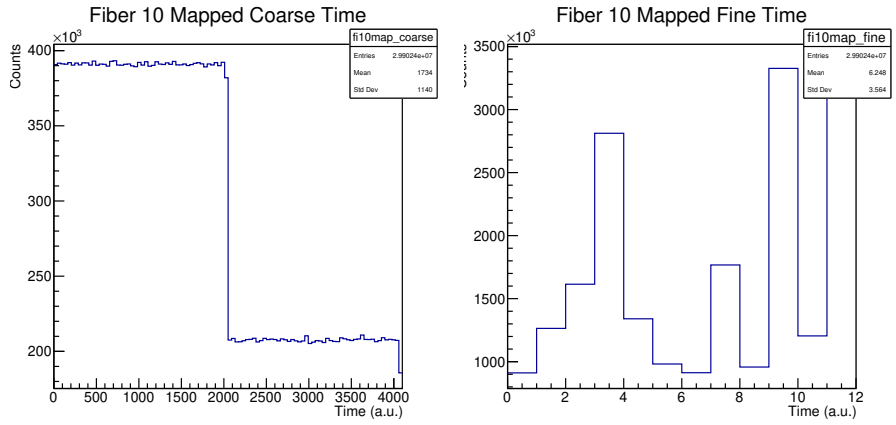

Figure 4.8.: At the Mapped level, the two time read-outs from the Clock TDC, coarse and fine time, are read out separately. The maximum coarse time window provided is 4096 bins for both the leading and trailing times. The fine time is used to improve the time resolution and uses twelve phase-shifted clocks of the same frequency.

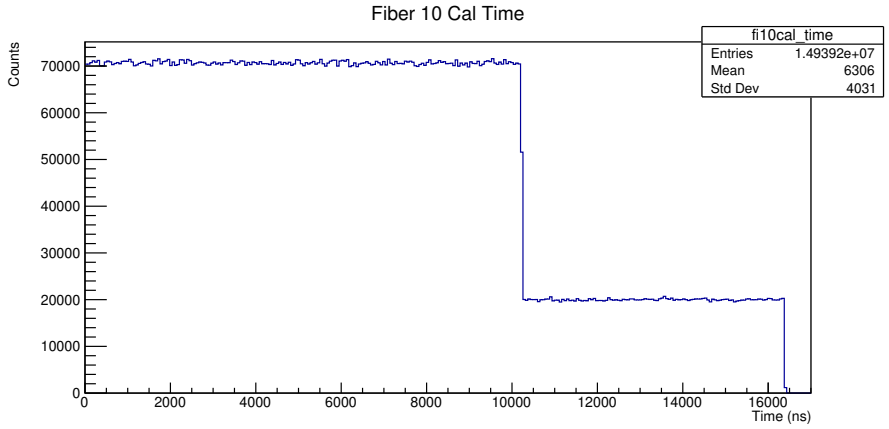

Figure 4.9.: At the Cal level, the coarse and fine times are combined together and converted into ns. This is done by multiplying the coarse time and the clock frequency for MAPMT or Tamex frequency for SPMT and subtracting the fine time.

More parameters need to be generated between the CAL and HIT levels for the fibers. All of the information for gain matching and getting positions in centimeters can be found in the macro R3BBunchedFiberHitPar.h and R3BBunchedFiberHitPar.cxx created by M. Heil. The root file created in the CAL level for the sweep run is unpacked through a macro that calls on the previously mentioned files and will calculate the necessary gain and offset parameters. These parameters are matched based on if the signal came from a MAPMT or SPMT. The ToT is then calculated, again using MAPMT and SPMT separate. For each PMT, the leading time finds a matching trailing time. The ToT is filled by the trailing time subtracting the leading time, both of which have been converted to ns using the clock frequency and coarse binning. The ToT and fiber ID are plotted together and the ToT is projected and searches for the maximum bin, and this is the gain parameter. The offset is found similarly by plotting the time of flight against fiber ID, projecting the time of flight, and finding the maximum bin. Once the gain match and offset parameters have been generated, root files with CAL level data for any run can be sent through a different unpacker that calls these parameters and be accurately calibrated and ready for analysis.

Once the fibers have been calibrated to the HIT level, there is a lot of information available to use for analysis. The fiber identification is the HIT level information for the channels. The script will make a permutation over every hit in the MAPMT and SPMT to match all the unique fiber IDs. There is now X or Y position information in centimeters, whether the information is X or Y depends on the orientation of the detector. This position information is essentially the same information as the fiber identification, just with real position units. The conversion to cm is accomplished by using the fiber thickness, fiber ID, detector width, and the air layer, which is relative to the fiber thickness. At the HIT level, the SPMT information has been combined with the MAPMT information and there are now 1024 fibers presented instead of 512 channels, as can be seen in Fig. 4.10. The large peak

starting from around fiber number 400 is the unreacted beam, and the smaller counts to the right after fiber number 500 are the reacted particles. The energy loss is calculated by taking the square root of the MAPMT ToT multiplied by the SPMT ToT, both of which were determined in the steps described above. The final time is calculated by averaging of the MAPMT time and the SPMT time, again having been determined in the steps described above, and is now the combination of all coarse and fine times for the leading and trailing times.

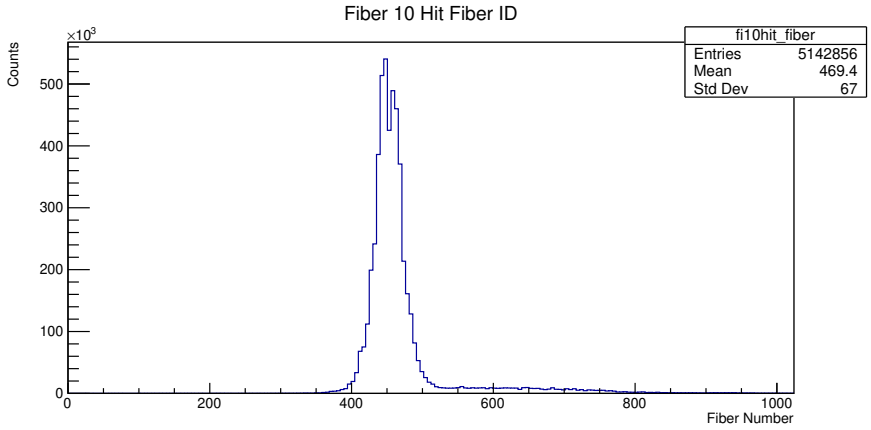

Figure 4.10.: At the Hit level, the information from the MAPMT and SPMT are combined. Now the individual fibers are distinguishable and there are 1024 fibers seen in the Fiber ID plot.

Although the fiber detectors were calibrated completely to the hit level, they were not used in the analysis in the present work as they are not necessary to measure the charge-changing cross section. For more information on the analysis for the energy loss of the fiber detectors, please refer to App. A.

5. Analysis and Results

Once the detectors have been successfully calibrated the Hit level as discussed in the previous chapter, they can be used to analyze for physical data. This chapter will describe the final analysis method used to extract a charge-changing cross section and the calculations. The results of this method are presented as well as theoretical calculations. Discussions on how the experimental method can be improved are presented at the end of this chapter as well.

5.1. Cross Section Calculations

5.1.1. Reaction Probabilities

The charge-changing cross section $\sigma_{\Delta Z}$, which has been defined in Sec. 2.1.4, is derived from the reaction probability of runs with a target, $P^t_{\Delta Z}$, and without (empty run), $P^e_{\Delta Z}$. If one assumes perfect conditions for detection and identification, i.e., detection and identification efficiency at 100%, the number of incoming particles, I, would be equal to the unreacted particles, U, and the reacted particles, R

$$I = U + R. \tag{5.1}$$

The reaction probability, P, is therefore defined as

$$P = \frac{R}{I} = 1 - \frac{U}{I}. \tag{5.2}$$

The number of incoming particles is easily extracted from using either LOS or PSP2, so only U or R needs to further be extracted from the data.

Since detection and identification methods are generally not perfect, corrections need to be applied to Eq. 5.1 and 5.2. There are less systematic uncertainties for U, and is therefore the observable used for calculations.

5.1.2. Cross Sections

Thin Targets

The method used for cross section calculation is dependent on the thickness of the target used. As the thickness of the target increases, the projectile will lose more energy as it travels through and experience a straggling effect so it is no longer moving on a straight-line trajectory. Thicker targets also pose the possibility of multiple reactions, i.e., the already reacted particle reacts a second time with a different particle inside the target. This effect is explained more in Sec. 5.1.2. For an experiment with a fixed target, the number of reacted particles is defined as

$$R = \sigma T I \tag{5.3}$$

where σ is the cross section and T is the number of scattering centers per unit area and defined as

$$T = t\frac{N_A}{M} \tag{5.4}$$

where N_A is Avogadro's constant, t is the target thickness in $\frac{g}{cm^2}$ and M is the target's molar mass. The molar mass of carbon is $M = 12.0107\frac{g}{mol}$. Using Equations 5.1 and 5.2, the cross section, σ with reaction probability P is

$$\sigma = \frac{1}{T}P \tag{5.5}$$

for thin targets. This calculation, however, does not account for any background contributions. For this, a run with no target needs to be included to subtract out the background reactions. R can then be split as

$$R = R_T + R_B \tag{5.6}$$

where R_T is the contribution of reacted particles in a target and R_B is the background contribution and are defined as

$$R_T = I^t \sigma T \tag{5.7}$$

$$R_B = (I^t - R^t)\frac{R^e}{I^e}. \tag{5.8}$$

where I^t is the number of incoming particles and R^t is the number of reacted particles for the target run, and I^e is the number of incoming particles and R^e is any reacted particle for the empty run. The reaction cross section can then be written as

$$\sigma = \frac{1}{T}\frac{(P^t - P^e)}{(1 - P^e)} \tag{5.9}$$

Thick Targets

When a thick target is instead used, the exponential decrease of possible reaction candidates, i.e., unreacted particles, throughout the target also needs to be considered [Sch17]. The number of particles detected is the same as before

$$R^t = R^t_{TR} + R^t_{BR} \tag{5.10}$$

where R^t_{TR} is the number of reactions in the target and R^t_{BR} is the number of reactions in the background. Looking at Fig. 5.1, the incoming projectile, or number of possible reaction candidates, I^t is

$$I^t \exp[-(\sigma + \sigma_p)T'] \tag{5.11}$$

where σ is the cross section for the reaction of interest and σ_p is the cross section of the primary reaction. $-\sigma T'$ excludes the possibility of counting an event twice and $-\sigma_p T'$ considers the decrease of reaction candidates that possibly happened in a different channel.

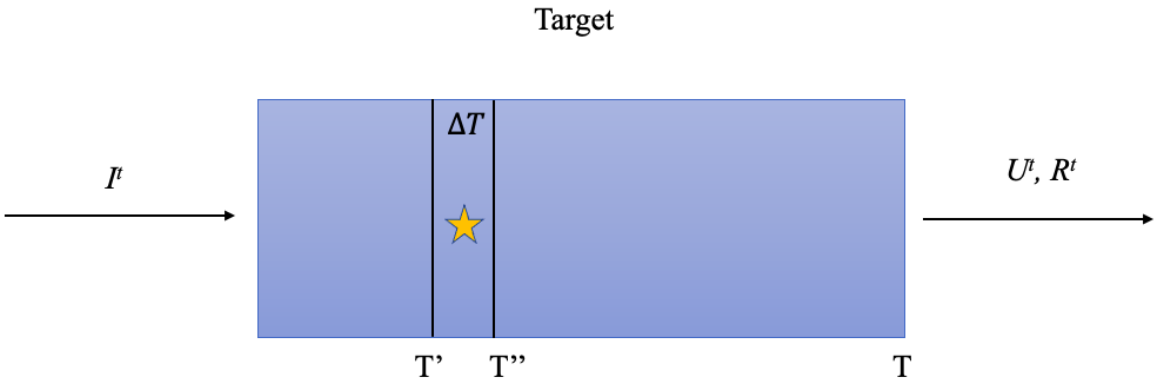

Figure 5.1.: Visualization of a projectile, I^t, interacting with a thick target in blue, and leaving the other side as either unreacted, U^t, or reacted, R^t. As the projectile travels through the target, it has the chance to react. If the yellow star represents the reaction of interest, it is still possible for secondary reactions to happen after. More details are supplied in the text.

The probability that the reaction happens in ΔT is $\sigma \Delta T$. So the number of reaction products in T" is expressed as

$$I^t \text{exp}[-(\sigma + \sigma_p)T'] \cdot \sigma \Delta T \tag{5.12}$$

From *T"*, secondary reactions are possible. The probability of a secondary reaction is denoted by σ_s. So it is possible the number of reactions is reduced due to this. R^t_{TR} can then be written as

$$R^t_{TR} = I^t \text{exp}[-(\sigma + \sigma_p)T'] \cdot \sigma \Delta T \cdot \text{exp}[-\sigma_s(T - T'')] \tag{5.13}$$

When $\Delta T \rightarrow 0$, so *T'=T"*, then Eq. 5.12 becomes

$$\text{d}R^t_{TR} = I^t \text{exp}[-(\sigma + \sigma_p)T'] \cdot \sigma \cdot \text{exp}[-\sigma_s(T - T')]\text{d}T' \tag{5.14}$$

Integrating over *T'* from 0 to T gives

$$R^t_{TR} = I^t \sigma \text{exp}[-\sigma_f T] \int_0^T \text{exp}[-(\sigma + \sigma_p)T']\text{exp}[\sigma_s T']\, \text{d}T' \tag{5.15}$$

$$= I^t \sigma \text{exp}[-\sigma_f T] \left[\left(\frac{1}{-\sigma - \sigma_p + \sigma_s} \right) \text{exp}[-(-\sigma - \sigma_p + \sigma_s)T'] \right]_0^T \tag{5.16}$$

$$= I^t \sigma \left(\frac{\text{exp}[-\sigma_f T]}{-\sigma - \sigma_p + \sigma_s} \right) (\text{exp}[-(\sigma - \sigma_p + \sigma_s] - 1)]. \tag{5.17}$$

The number of background reactions can then be expressed as

$$R^t_{TR} = I^t \text{exp}[-\sigma_\text{R}\text{T}]\text{P}^\text{e} \tag{5.18}$$

where the number of unreacted particles behind the target is I^texp[-$\sigma_R T$], σ_R is the total reaction cross section and P^e is the probability a background reaction will occur. Then inserting Eq. 5.17 and Eq. 5.18 into Eq. 5.10

$$R^t = I^t \sigma \left(\frac{\text{exp}[-\sigma_s T]}{-\sigma - \sigma_p + \sigma_s} \right) (\text{exp}[-(\sigma + \sigma_p - \sigma_s] - 1) + I^t \text{exp}[-\sigma_R T] P^e \tag{5.19}$$

$$= P^t I^t \tag{5.20}$$

and the cross section can be written as

$$\sigma = (P^t - e^{-\sigma_R T} P^e) \frac{-\sigma - \sigma_p + \sigma_s}{e^{-(\sigma + \sigma_p)T} - e^{-\sigma_s T}}. \tag{5.21}$$

In the circumstances that $\sigma_s = \sigma_p = \sigma'$, Eq. 5.21 can be written as

$$\sigma_{s=p} = -\frac{1}{T}\ln\left[e^{-\sigma_R T}e^{\sigma' T}P^e - e^{\sigma' T}P^t + 1\right] \tag{5.22}$$

This equation can be reduced further when applied to σ_R. $\sigma_s = \sigma_p = 0$ since any reaction is a reaction of interest and the classification therefore does not change with any subsequent reactions. Eq. 5.21 can then be simplified to

$$\sigma = -\frac{1}{T}\ln\left(\frac{U^t}{I^t}\frac{I^e}{U^e}\right) \tag{5.23}$$

$$= -\frac{1}{T}\ln\left(\frac{1-P^t}{1-P^e}\right). \tag{5.24}$$

Assumptions were made to allow for this cross section calculation, such as: the beam does not lose energy as it goes through the target, and therefore all reactions (of interest or secondary) occur similarly; background reactions are neglected if secondary; and background reactions are assumed to occur only behind the target.

In the case of the charge-changing cross section, Eq. 5.22 can be simplified to

$$\sigma_{\Delta Z} = -\frac{1}{T}\ln\left[e^{-\sigma_R T}P^e_{\Delta Z} - P^t_{\Delta Z} + 1\right]. \tag{5.25}$$

5.2. Method to Extract U and I

Now that it is understood how to calculate the cross sections, I^t, I^e, U^t, and U^e need to be extracted from the data. The method to extract the incoming and unreacted values is described in the following section. This was not the only method attempted, however, and these can be read about in Appendix B.

5.2.1. Maximum Energy Cuts

For any given event, it is possible that one or multiple detectors will see more than 1 hit. These hits are typically something other than a real event, such as noise from the electronics. In order to ensure that the data under analysis is a real physics events, a script was written to pull out the hit with the highest energy. There are also a lot of false events in the files, such as events with a

zero value that come from the trigger of a different detector. To remove events such as these, a multiplicity cut of 1 was placed on LOS, allowing only real events seen by LOS through. If a hit can fit both criteria, it is placed into a new root file which is then used to analyze the data. This method does introduce some systematic bias to the data as pileup will be included in the counts since it will be recognized as the hit with the highest energy. Pileup occurs when two events happen before the trigger window closes and the energies are summed together. The pileup will come from both unreacted and reacted; the unreacted counts are still needed but the reacted will add error into the calculations. However, this effect is small, not more than 10% of pileup events.

5.2.2. Fit Procedure

Incoming

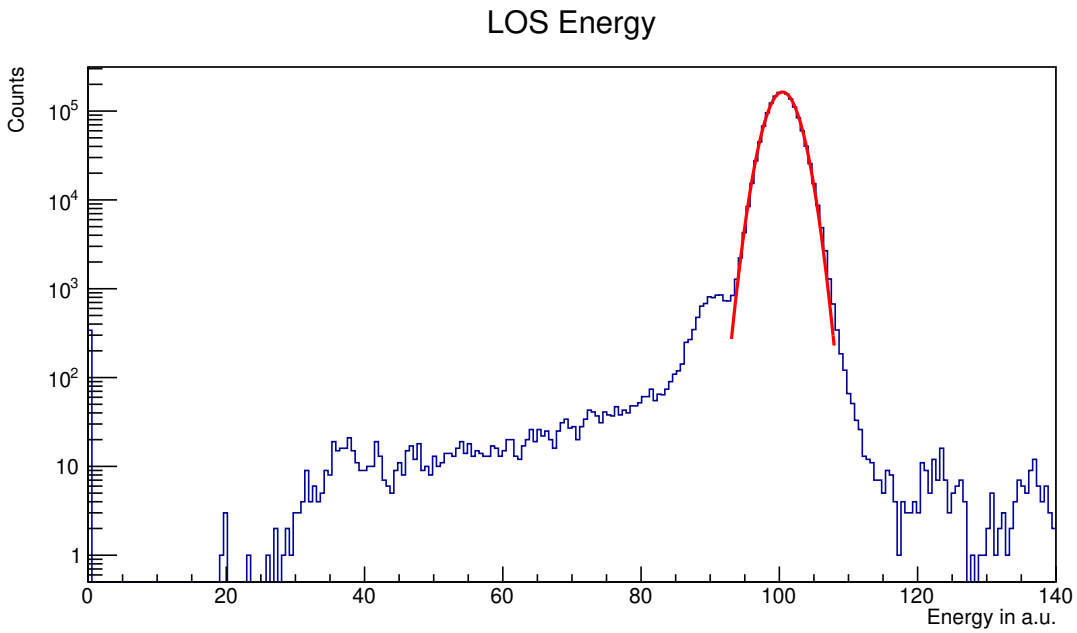

Figure 5.2.: LOS energy spectrum. The peak comes completely from the beam and a Gaussian can be fit very cleanly to extract the number of incoming particles.

For s473, there were two detectors in front of the target that can be used for extracting the number of incoming particles, LOS and PSP2. It was determined that LOS yielded more accurate numbers, so PSP2 was not used for this purpose. All numbers extracted for the incoming and unreacted were done in the same way; a Gaussian was fit to the energy peak and the integral of this fit divided by bin width gave the numbers used. LOS has a very clean energy peak that a Gaussian fit can easily be applied to, which can be seen in Fig. 5.2.

Unreacted

After a fit has been determined for the incoming, a 2 sigma cut from the fit of LOS is placed on the rest of the data to ensure that only particles from the incoming make it into the unreacted plots. There were two detector systems behind the target in s473 that were capable of providing energy information to extract the number of unreacted particles (U^e and U^t), PSP4 and PSP6 and the TOFD. The two PSP detectors were the more desirable detector system as they were directly behind the target, still in the vacuum, and have a high energy resolution. The TOFD calibration is still ongoing, so it could not be reliably used for the extraction of the unreacted particles. The two PSP detectors behind the target were used then.

In Fig. 5.4, the unreacted peaks in the PSP detectors can be seen quite clearly. However, when looking at the correlation plots of the two PSP detectors, there are arm-like structures coming off of the beam spot. It has been hypothesized that this is a feature from the response function of the PSP electronics that occurs when the rates are high in the strips. This feature begins around 1 kHz, and the rates for s473 were roughly between 2-3.3 kHz, as can be seen in Tab. 5.1. It was confirmed that these events do belong to the unreacted by placing a gate on the unreacted peak for TOFD. Therefore, the method to extract the unreacted particles was first done by fitting the peak of the 1D plots and finding the sigma value. A suitable cut for only Z=50 could not be determined this way. It is also visible in Fig. 5.3 that it is very difficult to clearly differentiate between Z=50 and Z=49 even in the 2D plots. To find the most suitable cut for the data, many charge-changing cross section calculations with different sigma cuts were performed. The different cross section values can be seen in Fig 5.5-5.7. These different values were obtained by taking the sigma value from the fit of the Z=50 peak and multiplying it with different constants to find a trend in the cross section values. The trend that can be seen most clearly in Fig. 5.6 and Fig. 5.7 is that the slope of the cross sections stays fairly consistent up until around $2 \cdot \sigma$, and then the slope becomes steeper. This is from the introduction of too many Z=49 particles into the cut and the reaction probability becoming lower. The slope in Fig. 5.5 remains fairly linear and not much can be determined from here. So, based on the plots with thicker targets, a 2 sigma cut was placed on low energy side of both PSPs, and all events above the unreacted peak were kept in the data since any cut larger than 2 sigma allowed Z=49 particles into the counts. The final cut can be seen in Fig. 5.3. Every run was individually analyzed using this method to keep the results as consistent as possible. It should be noted that the response function of the electronics is still under investigation, and it can not be said with certainty which events truly belong to the unreacted particles.

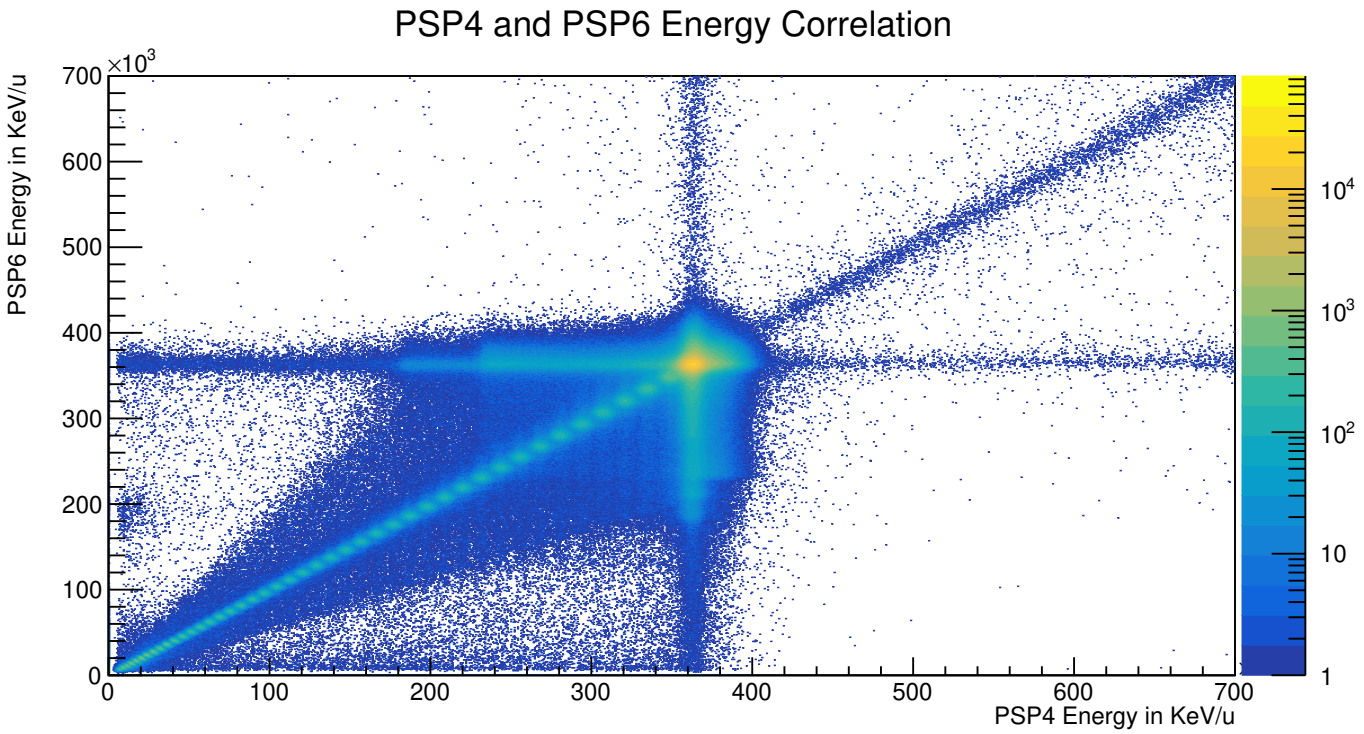

Figure 5.3.: Correlated energy spectrum for PSP4 and PSP6. The beam spot and fragments are clearly discernible. The arm-like features extending from the beam spot are from the response function of the readout electronics when the rates are too high per strip. These events are also unreacted particles. The kite like feature is also an artifact of the detector electronics.

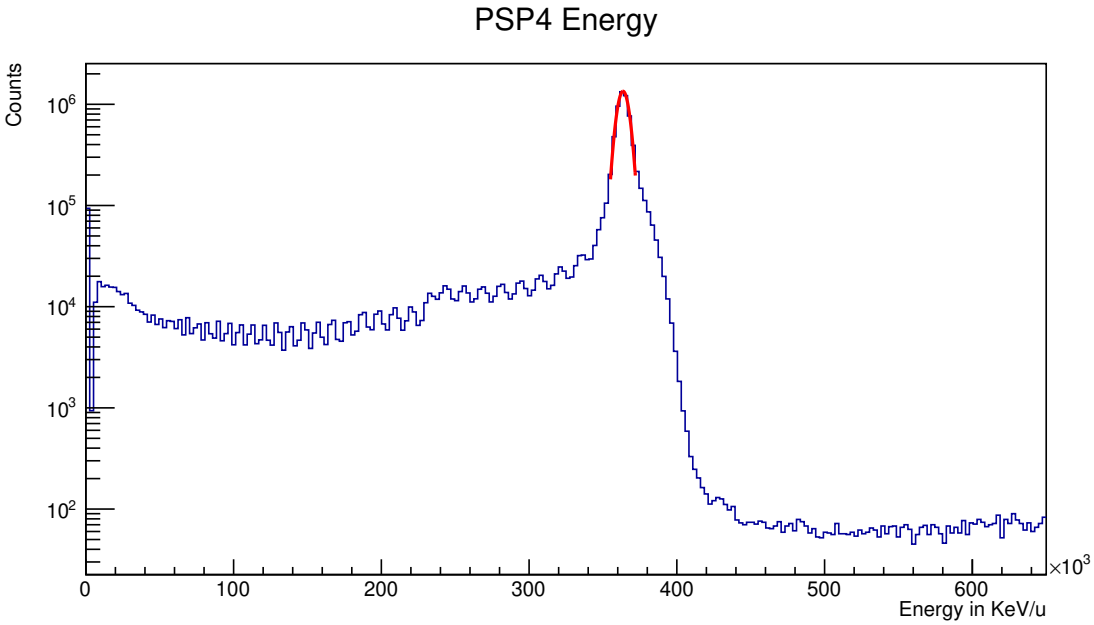

(a) PSPX4

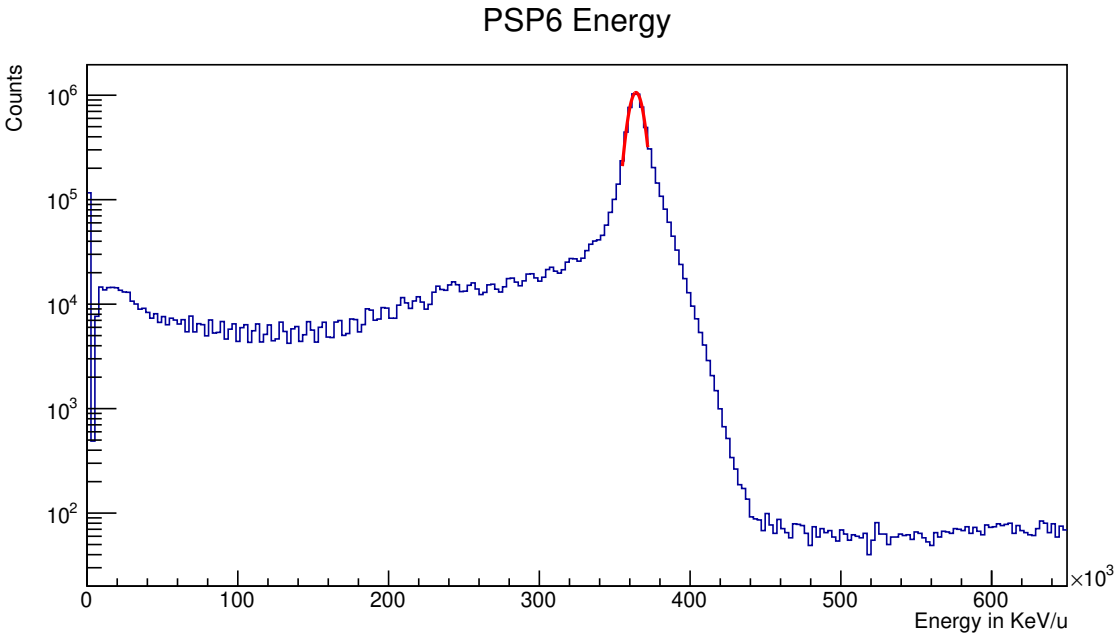

(b) PSPX6

Figure 5.4.: The energy spectrum's for PSP4 (Left) and PSP6 (Right). The shoulder from the pileup can be slightly be seen to the right of the peaks and the fragments to the left. Although better than PSP2, these peaks were also not Gaussian and also challenging to get an accurate fit.

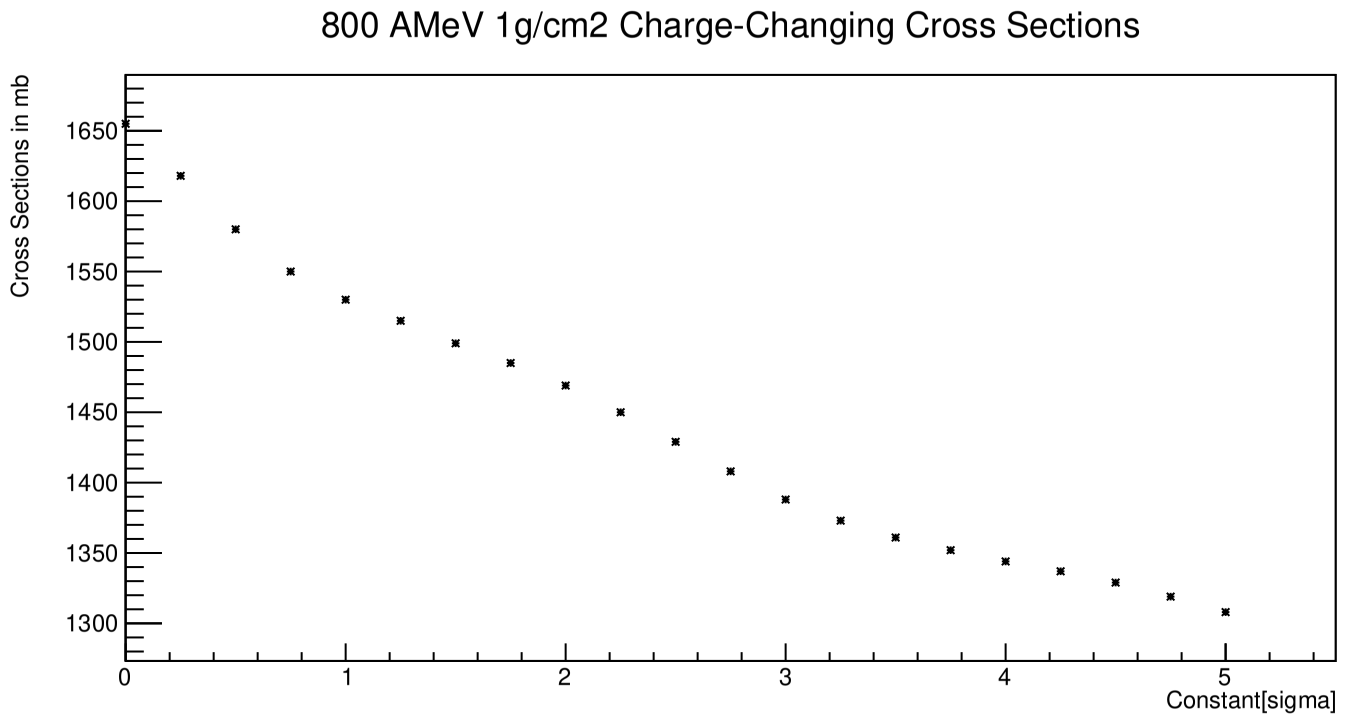

Figure 5.5.: Calculated charge-changing cross for beam energy 800 AMeV with a 1 g/cm^2 target using different sigma cuts. Constants between 0-5 were applied to the sigma value to see the change in the cross section value to determine which cut provides the most unreacted particles without going too far into the reacted particles. The slope here is fairly linear beyond 1 sigma, but this cut clearly removed unreacted Z=50 particles and was not used.

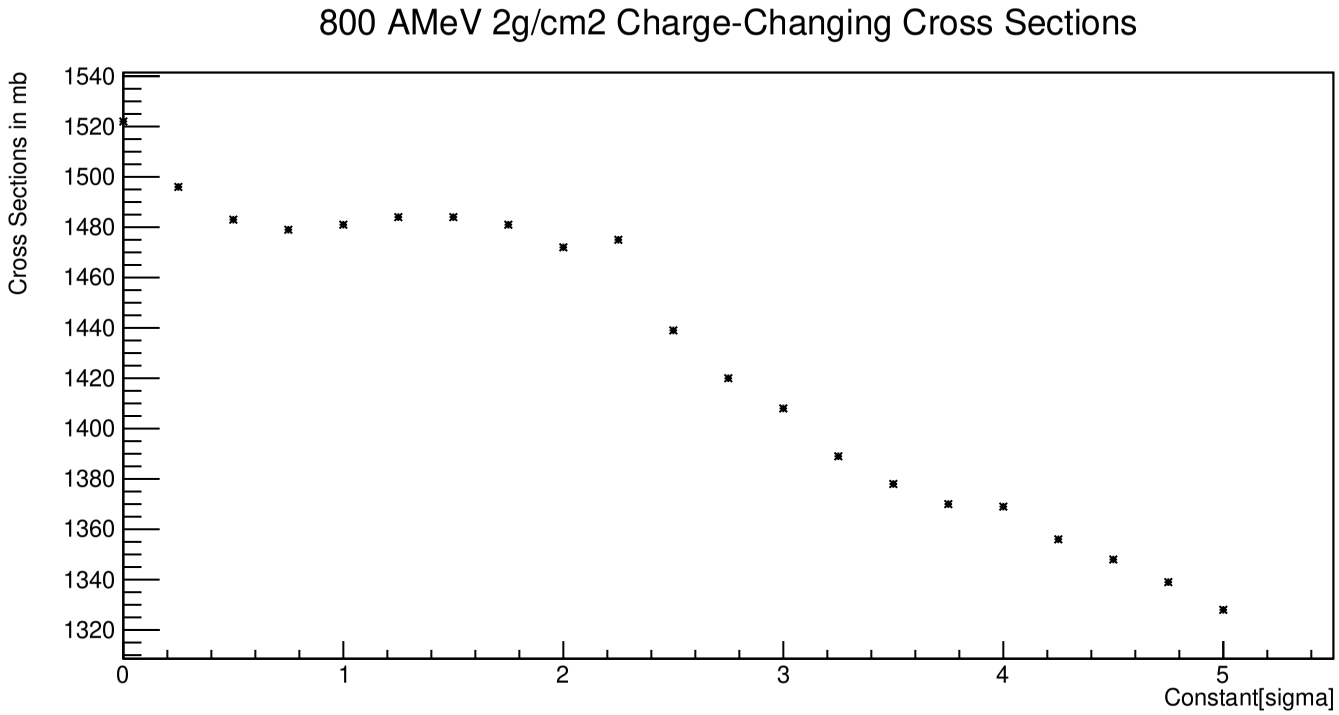

Figure 5.6.: Calculated charge-changing cross for beam energy 800 AMeV with a 1 g/cm^2 target using different sigma cuts. Constants between 0-5 were applied to the sigma value to see the change in the cross section value to determine which cut provides the most unreacted particles without going too far into the reacted particles. The cross sections remain fairly constant until about 2 sigma, and then starting dropping except for the outlier at about 2.2 sigma. A 2 sigma cut did not obviously remove any unreacted Z=50 particles and therefore was used as the cut placed on all data runs. An example of the 2 sigma cut can be seen in Fig. 5.8.

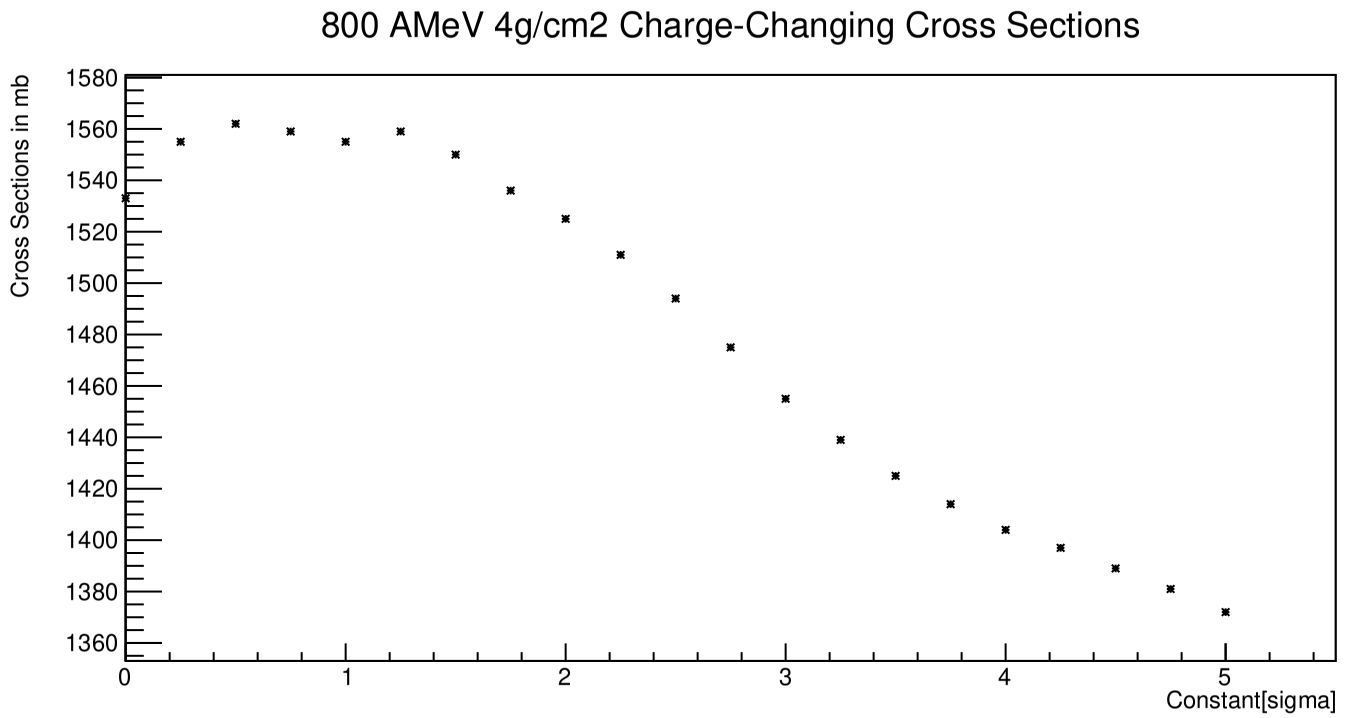

Figure 5.7.: Calculated charge-changing cross for beam energy 800 AMeV with a 2 g/cm^2 target using different sigma cuts. Constants between 0-5 were applied to the sigma value to see the change in the cross section value to determine which cut provides the most unreacted particles without going too far into the reacted particles. The cross sections remain fairly constant until about 1.6 sigma, and then starting dropping. However a cut of 1.6 sigma clearly removed unreacted Z=50 particles and was not used.

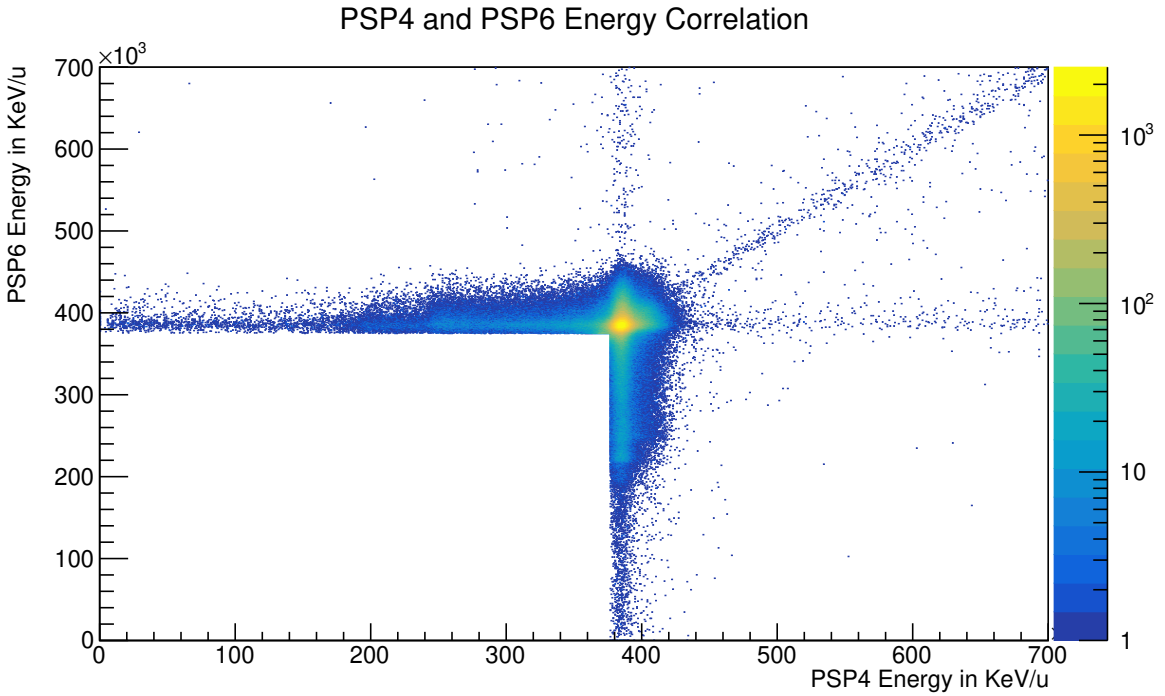

Figure 5.8.: Cut used on PSP4 and PSP6 to extract the number of unreacted particles after the target. The uncorrelated arms extending from the beam spot comes from the electronics spreading out the signal due to a high rate and also need to be included in the value for the unreacted particles.

5.2.3. Error Propagation

Statistical Error

The statistical uncertainty for σ is calculated using Gaussian error propagation. Eq. 5.23, which was used to calculate the charge changing cross sections, had 5 variables to calculates statistical error from: T, I^t, U^t, I^e, and U^e with corresponding errors ΔT, ΔI_t, ΔU^t, ΔI^e, and ΔU^e. The equation is then:

$$\Delta\sigma = \sqrt{\left(\frac{\partial\sigma}{\partial T}\Delta T\right)^2 + \left(\frac{\partial\sigma}{\partial U^t}\Delta U^t\right)^2 + \left(\frac{\partial\sigma}{\partial I^t}\Delta I^t\right)^2 + \left(\frac{\partial\sigma}{\partial I^e}\Delta I^e\right)^2 + \left(\frac{\partial\sigma}{\partial U^e}\Delta U^e\right)^2}. \tag{5.26}$$

The systematical error from the target is included is included in ΔT and is negligibly small for all targets used in this experiment. Therefore Eq. 5.26 can be simplified to

$$\Delta\sigma = \left(\frac{1}{T}\right)\sqrt{\left(\frac{-1}{U^t}\Delta U^t\right)^2 + \left(\frac{1}{I^t}\Delta I^t\right)^2 + \left(\frac{-1}{I^e}\Delta I^e\right)^2 + \left(\frac{1}{U^e}\Delta U^e\right)^2}. \tag{5.27}$$

Systematic Error

The systematic error investigated in this thesis is the acceptance and efficiency of the PSP detectors and the error of the cut described in Sec. 5.2.2. There is also a contribution from the correction of using the ”simpler” Eq. 5.23 instead of Eq. 5.25, which is discussed in Sec. 5.1.2.

The acceptance of the PSP detectors were found to be 100% and therefore have no contribution to the systematic error. The acceptance was confirmed by gating on the position of beam spot in PSP2 and PSP4 and counting the number of events. The position of the beam spot and reacted particles for PSP4 can be seen in Fig. 5.9. All particles clearly fit within the 10 cm width of the detector.

Due to the geometry of the setup, only the efficiency of PSP4 can be determined, which was found to be 94.5%. This was calculated by placing a cut on charge Z=50 on all PSP detectors and counting the number of hits. So in the case of PSP4, the equation would be

$$Eff.(PSP4) = \frac{Z = 50(PSP2, PSP4, PSP6)}{Z = 50(PSP2, PSP6)}. \tag{5.28}$$

This efficiency is then applied to the number of unreacted particles in Eq. 5.23. However, since the counts for unreacted particles are present on both sides of the fraction in this equation, the efficiency correction cancels itself out and therefore does not contribute to the systematic error. However, if the efficiency of the detectors is different, this does does not cancel out and would have an impact on the systematic error. Since only the efficiency of PSP4 can be determined, it is assumed all efficiencies are equal and therefore cancel out.

The error of the cut placed to extract the number of unreacted particles also needs to be investigated. This was done by placing a cut on the uncorrelated ”arms” that are visible in Fig. 5.8 and an example of the cut can be seen in Fig. 5.10. A Gaussian was fit to the 1D projection of the cut and an example of a fit is seen in Fig. 5.11. The dotted line here represents the missing unreacted particles taken away by the cut. The integral was calculated from 0 to the start of the cut to get a count of the missing unreacted particles, as well as the error of the cut. The missing unreacted counts were added to the existing yields and a new corrected cross section was calculated. The error propagation was preformed and was found to be less than 2 mb for all runs, and therefore negligible.

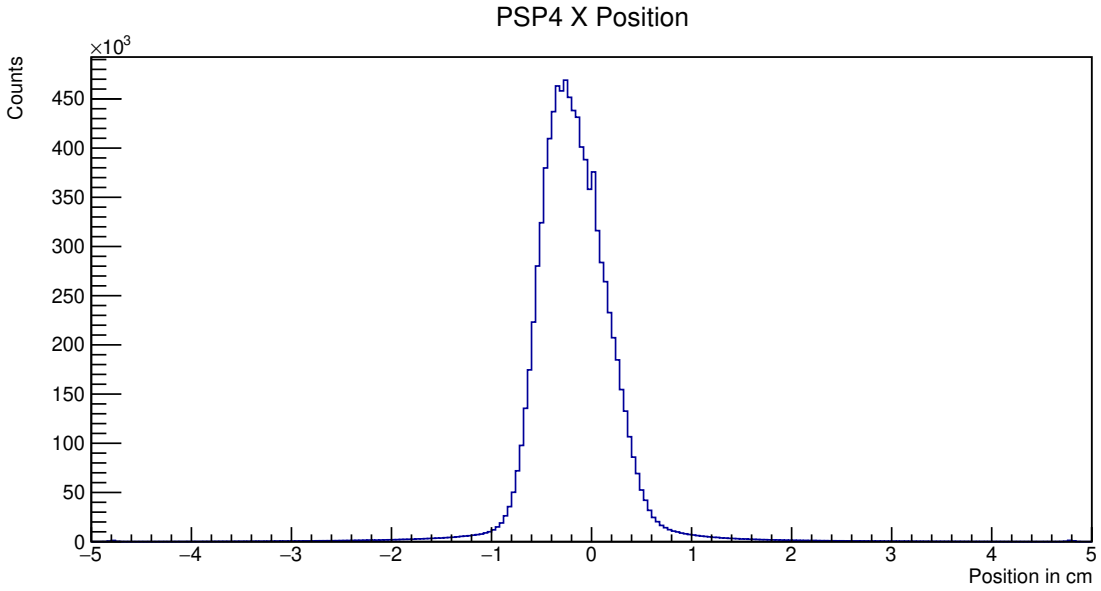

(a) X Position

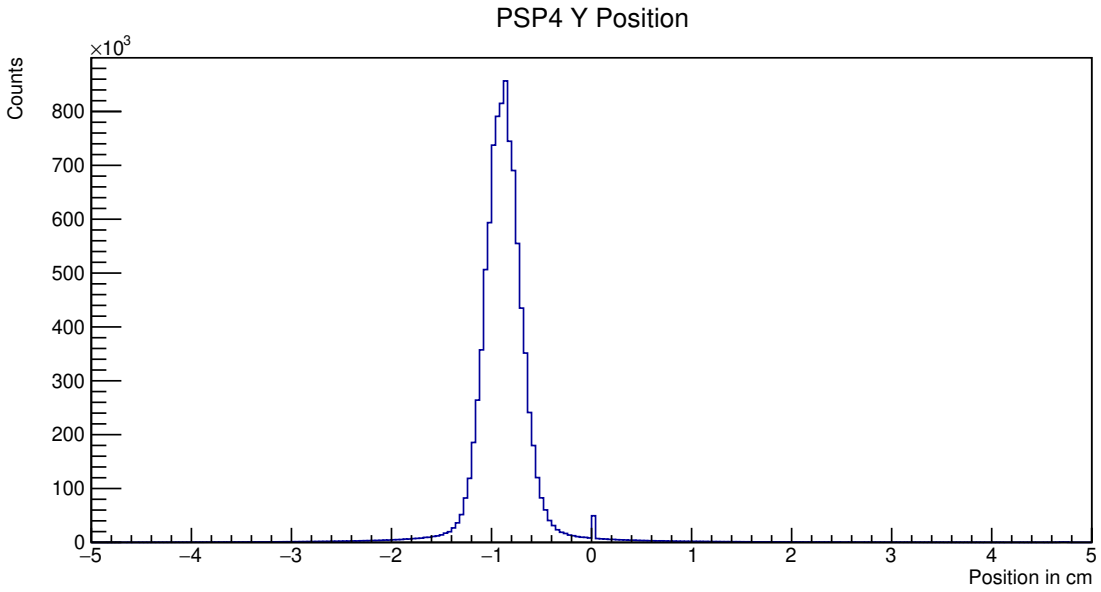

(b) Y Position

Figure 5.9.: Plot (a) shows the X position of PSP4 and Plot (b) shows the Y position of PSP4 from a run with the 1 g/cm^2 target. All counts clearly inside the 10 cm width of the detector.

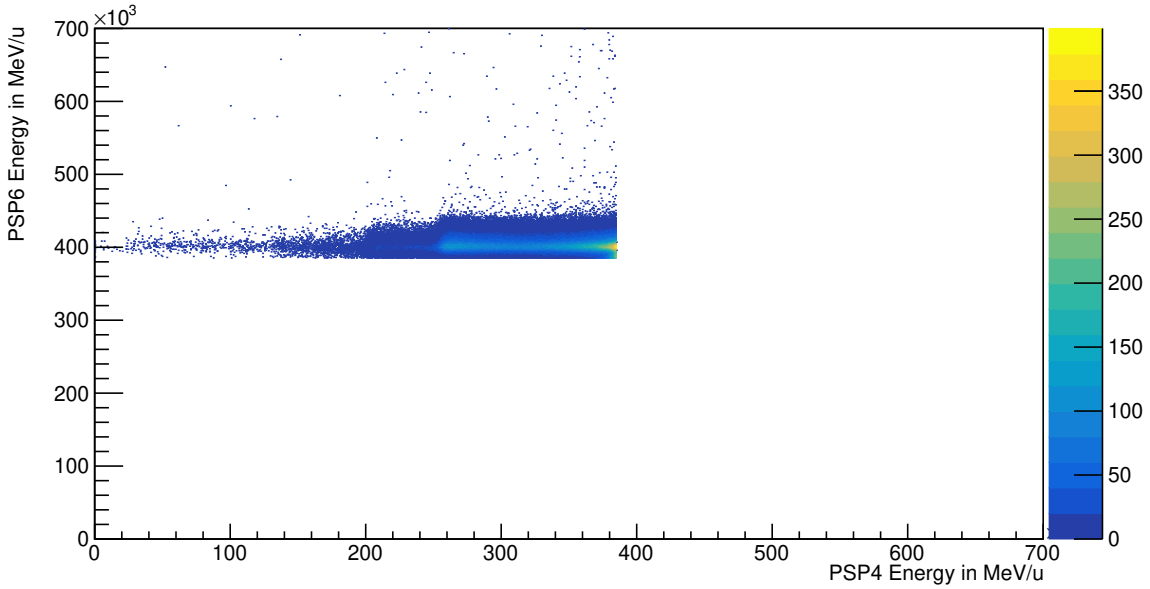

Figure 5.10.: Example of the cut placed on one of the uncorrelated arms to determine how many unreacted particles were excluded due to the original 2 sigma cut.

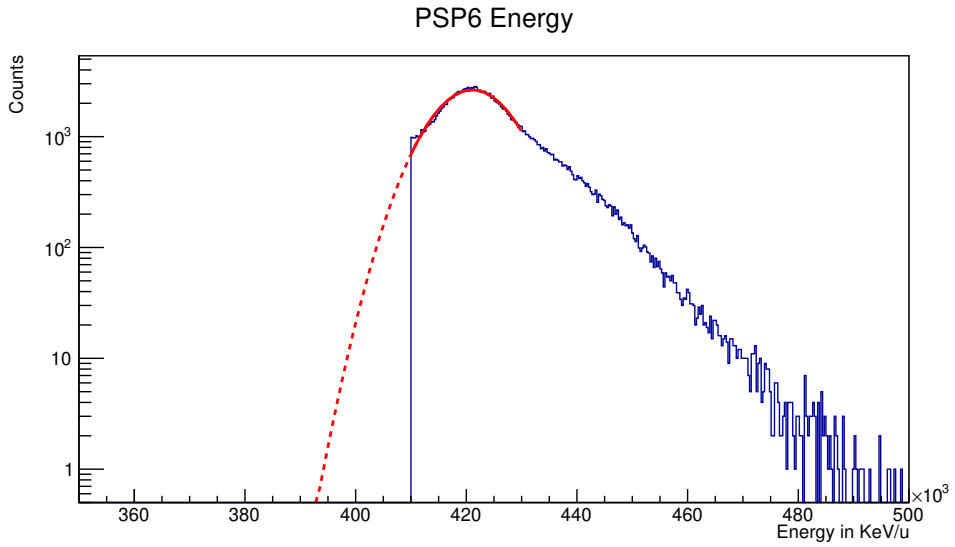

Figure 5.11.: An example of the fit placed on one of the arms presented in log scale. The dotted line represents the unreacted particles eliminated from the counts by the cut. The integral and error of this fit was done from 0 to the value of the cut. These additional counts were added to calculate a corrected charge changing cross section and the error of the cut.

As it can be seen in Eq. 5.25, σ_R is an input. However, the focus of this analysis was σ_Z and σ_R was

not included to this point. This made it not possible to use Eq. 5.25 since only experimental inputs should be used to check the validity of the theoretical models. Therefore, the ”simpler” Eq. 5.23 was used to calculate σ_Z. However, the correction to the background that is included in Eq. 5.25 can not be overlooked. Therefore, the difference between the calculated cross sections are added in to the result as a systematic error. The input for σ_R comes from the the theoretical calculations of C. Bertulani [Ber23]. The theoretical calculations are described in more detail in Sec. 5.4.1, where it is discussed that they are higher than the experimentally obtained values. The error for Eq. 5.25 can be written as

$$\Delta\sigma_{\Delta Z} = \sqrt{\left(\frac{\partial\sigma_{\Delta Z}}{\partial T}\Delta T\right)^2 + \left(\frac{\partial\sigma_{\Delta Z}}{\partial P^t_{\Delta Z}}\Delta P^t_{\Delta Z}\right)^2 + \left(\frac{\partial\sigma_{\Delta Z}}{\partial P^e_{\Delta Z}}\Delta P^e_{\Delta Z}\right)^2 + \left(\frac{\partial\sigma_{\Delta Z}}{\partial\sigma_R}\Delta\sigma_R\right)^2}. \tag{5.29}$$

Eq. 5.29 is not completely correct, as the $P\Delta Z$ values come from data stating σ_R. This contribution is weighted additionally by $P_e\Delta_R$, which is a small number. It should be noted that the uncertainty is slightly overestimated. The contribution from σ is very small and therefore has a small effect on the overall value of Eq. 5.29. This allows for the input of σ_R to be any theoretically calculated value with little consequence to the error. The value chosen was from the model that had the closest charge radius value to the experimentally measured. To find the systematic error from using Eq. 5.23, the value from Eq. 5.25 was subtracted to find the difference in the cross sections. This difference was between 1-3% of the corrected cross sections.

5.3. Results

Due to the uncertainties discussed above in Sec. 5.2.2, the results presented here require further investigation before they can be considered final. The results presented here were calculated using a 2 sigma cut on LOS for the incoming values and a 2 sigma cut on the low energy tail of the unreacted peak, but includes all events above, on both PSP4 and PSP6 for the unreacted values, as this method gave the cleanest cut to exclude any charge that was not Z=50.

5.3.1. Reaction Probabilities and Charge-Changing Cross Sections

As discussed in Sec. 5.2, it was hypothesized that the electronics used on the PSP detectors spread the signal of the incoming data if the rate is higher than 1 kHz. The spread out signal can be seen in the uncorrelated arms of PSP4 and PSP6 in Fig. 5.8. Using a cut on the unreacted beam in TOFD, it

was confirmed that the majority of these events are indeed the unreacted beam. The results for the charge-changing cross section that can be seen in Tab. 5.1 were obtained by placing a 2 sigma cut on the beam spot for both PSP4 and PSP6. The data for energy with 2 sigma below the beam spot and all the energy higher was taken into consideration for the cross section calculations. The cut used can be seen in Fig. 5.8. A 2 sigma cut was chosen because any cut larger would allow too much of charge Z=49 into the counts. The extracted value for the incoming particle count comes from placing a 2 sigma cut on the beam spot in LOS.

There is also the possibility for Z=51 to be populated as a result of charge-exchange reactions, meaning a reaction that turns a neutron into a proton. These reactions can happen through two different processes; the Gamow-Teller (GT) giant resonance, which is the oscillation in spin-isospin degrees of freedom without spatial wave function changes [Yas+18], or the excitation of a Δ (1232) resonance, which results in a significant kinetic energy shift and the decay to a nucleon and a pion [Rod+20]. The pion production threshold in a laboratory setting is 300 MeV/nucleon, and therefore can only be observed in higher energy experiments, whereas Gamow-Teller can be seen at excitation energies as low as $E_x = 16.5$ MeV. As the first interaction for the charge-exchange happens with a neutron, it is not included in Glauber-model calculations, and should be considered when comparing experiment to theory. Due to the structure of this data, Z=51 particles are not excluded and contribute the the counts for the charge-changing cross section.

Since the rate used during the experimental run has an effect on the detectors, an investigation into whether the rate also affects the reaction probability, and therefore the cross section, was also done. The rates from each individual run were calculated and can also be seen in Tab. 5.1. Some connections between the rate and the resulting measurements could be made. The most substantial result came from two runs with energy 550 AMeV. Two runs conducted directly after another using the same target, C 1 g/cm^2, had the rates increased between them. With no other changes in the experimental setup, this resulted in $\sigma_{\Delta Z}$=1636 mb for the run with a lower rate and $\sigma_{\Delta Z}$=1506 mb for the run with a higher rate.

Energy in AMeV	Target C in g/cm^2	Rate (kHz)	Reaction Probability $P_{\Delta Z}$	$\sigma_{\Delta Z}$ in mb
400	empty	2.187	0.03954	
	1	2.457	0.10351	1360 (14)(36)
550	empty	2.991	0.02785	
	1	2.048	0.10709	1636 (13)(22)
	1	2.973	0.10205	1506 (20)(25)
	2	2.561	0.17208	1571 (13)(21)
650	empty	3.059	0.03783	
	1	3.063	0.10143	1291 (17)(41)
	2	3.133	0.162707	1365 (10)(37)
800	empty	3.095	0.03093	
	1	3.249	0.09993	1417 (16)(31)
	2	3.223	0.16303	1441 (7)(30)
	4	3.264	0.28811	1490 (7)(26)

Table 5.1.: Rates, reaction probabilities, and corrected charge-changing cross sections, $\sigma_{\Delta Z}$, including statistical and systematic error for ^{120}Sn obtained in the present analysis using a 2 sigma cut to acquire the incoming and unreacted particle values.

All charge-changing cross section values are corrected from the cut error and presented below as a function of energy in Fig 5.12. The vertical error bars represent the statistical and systematic error for the cross section value and the horizontal error bars in represent the energy loss of the beam as it travels through the front, middle, and end of the target. Beyond the error bars, there is additional uncontrollable uncertainty due to the beam rate fluctuation, which accounted for about a 20% change for deducible unreacted particle yields. This makes the cross section values discussed in this thesis unusable to compare to theory, and therefore, no conclusion can be drawn from these numbers.

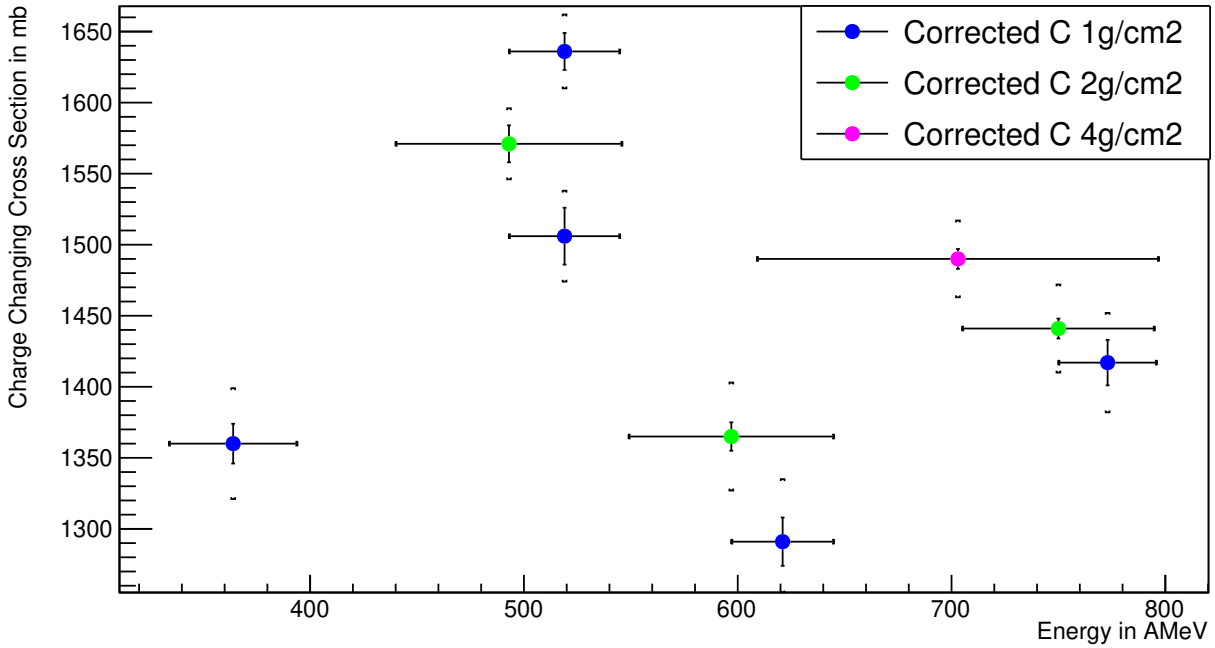

Figure 5.12.: Corrected charge-Changing cross sections for s473 presented as a function of energy. Error bars in the horizontal represent the energy loss as the beam goes through the target. Error bars in the vertical represent the calculated statistical and systematic error for the charge-changing cross section. There is additional uncontrollable uncertainty due to the fluctuation of the beam rate, which accounts for around a 20% change in deduced unreacted particle yields. The target thicknesses are presented by different colors.

5.4. Discussion

5.4.1. Theoretical Calculations

The theoretical calculations were kindly done by C. Bertulani [Ber23] using 19 different Skyrme functionals. Due to the uncertainties from the experimental measurement, a direct comparison between the theoretical and experimental values could not be suitably done. The theoretical results for the charge-changing cross section vs the charge radius (R_{ch}) for each energy used in s473 can be seen below in Fig. 5.13-5.16. The charge radius has been precisely measured at 4.6519(0.0021) fm [AM13] and is represented in the plots with a solid black line and the blue box surrounding it is the experimental error. For an accurately measured charge-changing cross section, the value would be expected around the slope of the theoretical calculations.

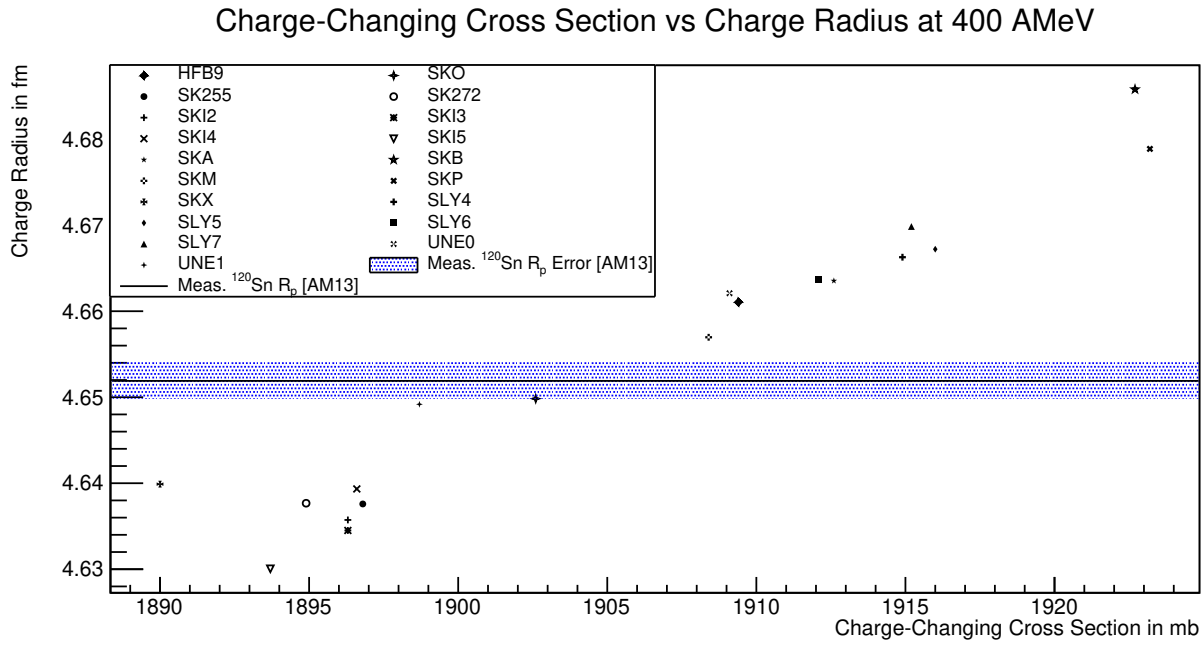

Figure 5.13.: Glauber model calculations provided by C. Bertulani [Ber23] for ^{120}Sn+C at 400 AMeV from 19 Skyrme functionals presented as data points. The solid black line represents the experimentally measured charge radius (R_p) [AM13] for ^{120}Sn and the blue box is the error. It is expected the measured charge-changing cross section would be at the cross of this line and the slope of the theoretical model calculations.

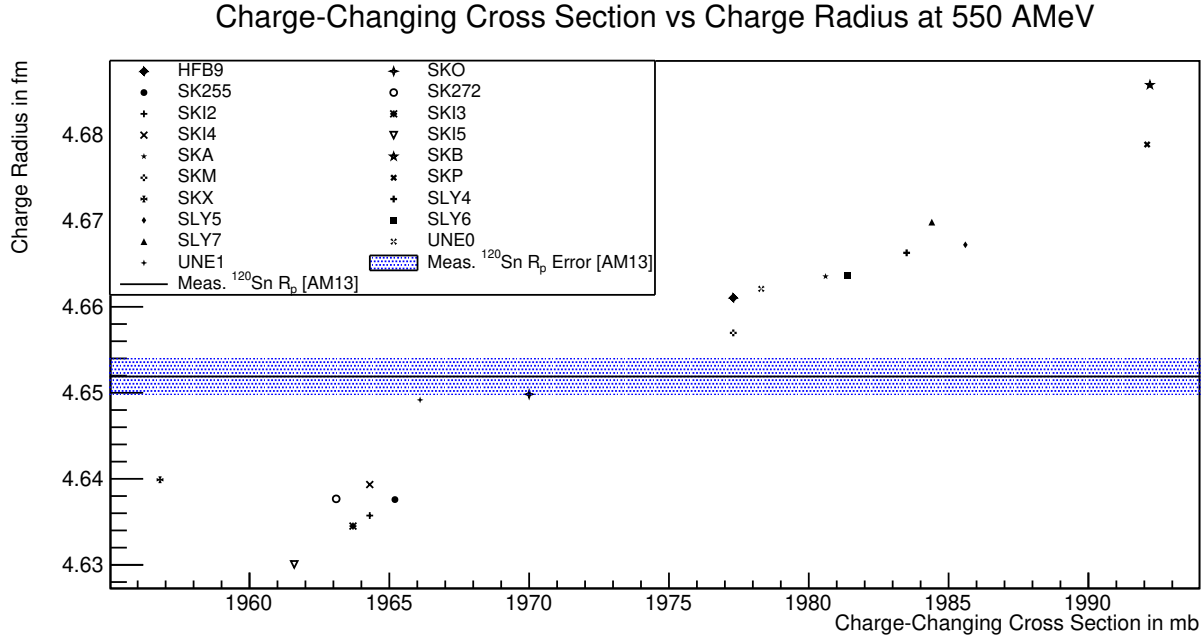

Figure 5.14.: Same as Fig. 5.13 for energy 550 AMeV.

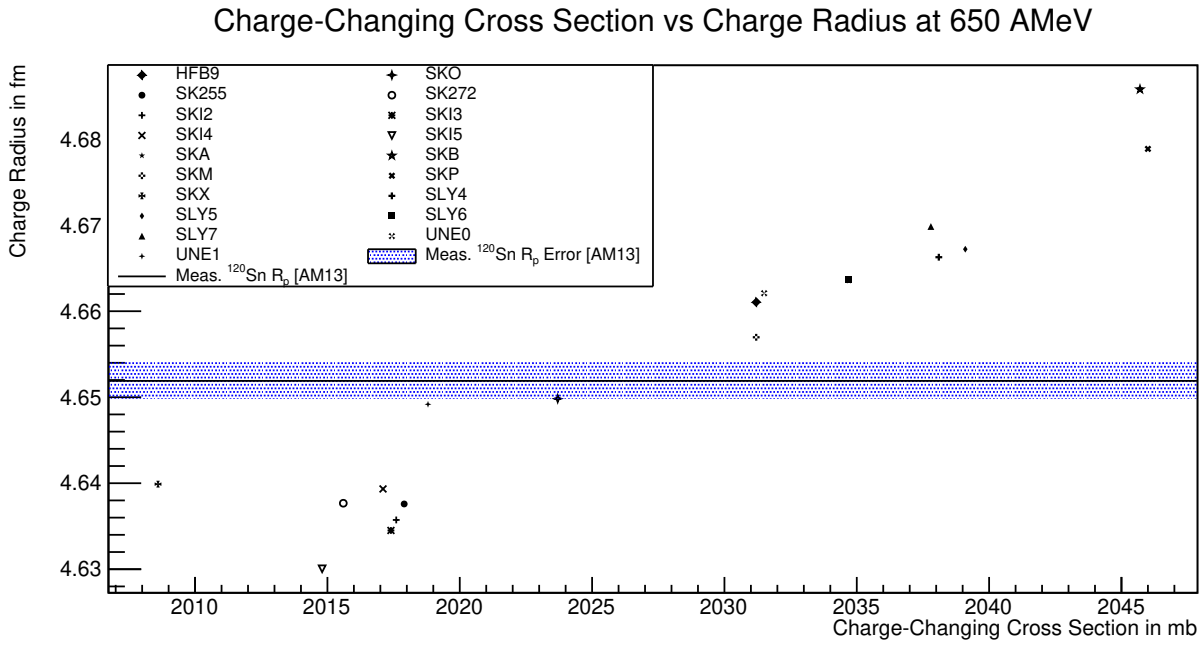

Figure 5.15.: Same as Fig. 5.13 for energy 650 AMeV.

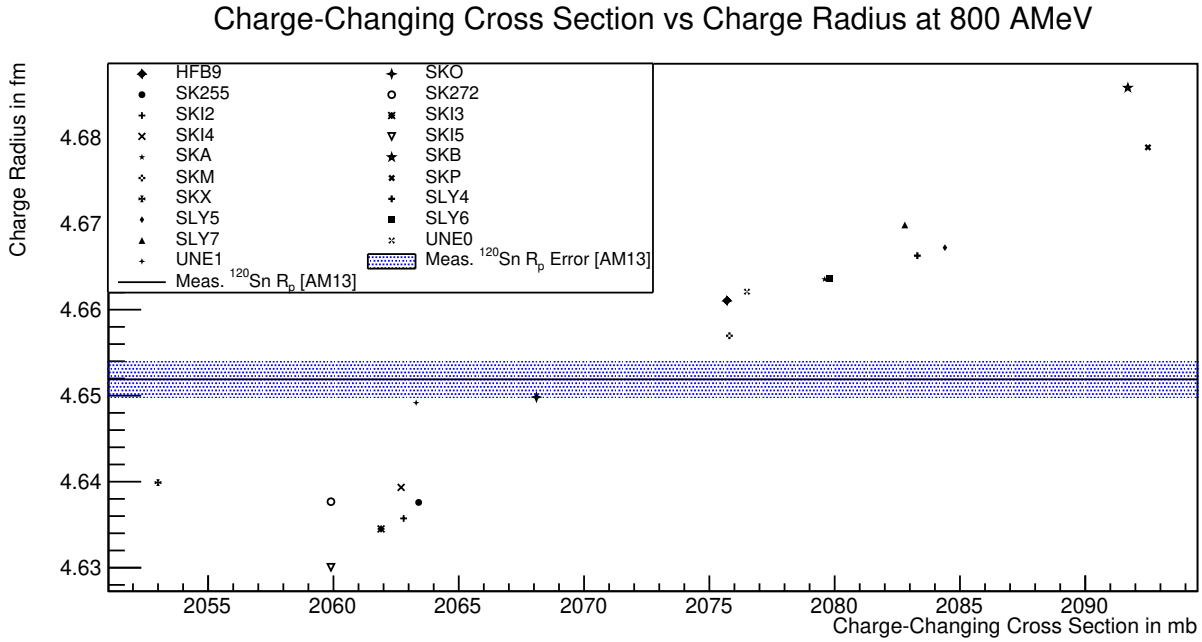

Figure 5.16.: Same as Fig. 5.13 for energy 800 AMeV.

5.4.2. Experimental Limitations

The statistics for this experiment were quite high, and therefore the statistical error is small. The exact values can be seen in Tab. 5.2.

Energy in AMeV	Target C in g/cm^2	Statistics Incoming	Statistics Unreacted	$\Delta\sigma_{\Delta Z}$ in mb
400	empty	8098354	7778129	
	1	8861750	7944443	14
550	empty	13162656	12796130	
	1	8526991	7613860	13
	1	2547282	2287320	20
	2	1553393	1286087	13
650	empty	4049303	3896084	
	1	11302196	10155747	17
	2	4835986	4049035	10
800	empty	11224808	10877678	
	1	4535277	4082057	16
	2	7861181	6579542	7
	4	1445653	1029152	7

Table 5.2.: Statistics and statistical error for every run used in the analysis of the work presented in this thesis.

Gathering the quantities for the input for the reaction probability $P_{\Delta Z}$ is not trivial. The cross section measurement is sensitive enough that a small change in the way the cut is done or method of extracting the values can result in a large change in the measured cross section. The majority of the difficulties analyzing this experiment came from the issues stemming from the readout of the electronics in the PSPs. The PSPs are the ideal detectors to extract the number of unreacted particles, as they have a good energy loss resolution. From Fig 5.4, it can be seen that the energy loss resolution is capable of distinguishing the individual charges down to around $Z = 25$. Using one before the target and two after allows for less uncertainty in the extracted values as everything is being detected with the same electronics and method. Two PSPs behind the target allows for a clear correlation of the unreacted beam and reacted particles, so clear cuts can be made on the data. However, due to the electronics spreading out the signal when overloaded by a high rate and the unresolved issues surrounding pile-up, these detectors could not be used to the best of their abilities. The detector in front of the target was deemed unusable as the spread of the data from the high rates was too large and yielded inaccurate values. Many attempts were still made to use the PSP detectors behind the target, but it cannot be said for certain what the best method to extract the values were given the current condition of the data. With the removal of the issues stemming from the readout of the electronics, it is possible that the data from the detectors would then be usable and an accurate cross section measurement could be attainable. Therefore, it is necessary that the response functions of the detectors be understood, and that the detectors are calibrated to the highest resolution possible.

The final calibration of the TOFD is still in progress. The reaction probabilities measured from using the TOFD to extract the unreacted values were very high, with values of around $P_{\Delta Z} \approx 0.29$ for an no target run. The cross sections measured were difficult to understand as they ranged from $\sigma_{\Delta Z} \approx 1366 - 2262$ mb. It is necessary for the TOFD to be calibrated to a higher resolution before results can be used from this detector.

The accuracy of the cross sections presented in Tab. 5.1 are not confirmed due to ongoing investigation of the detectors involved in the measurement.

5.4.3. Constraining L

If the desired constraint on L is within 30 MeV, this corresponds to a 0.08 fm sensitivity of the neutron skin thickness, which requires $\Delta\sigma_{\Delta N} \approx 10$ mb $(\Delta\sigma_{\Delta N}/\sigma_{\Delta N}) \approx 2.5$ % [Sch17].

While the analysis did not progress far enough to calculate the measured neutron-removal cross section, it is still possible to use the theoretical values and statistical error values obtained from the measured charge-changing cross section for valuable input. In Fig. 5.17, the theoretical neutron skin thicknesses are plotted as a function of the theoretical neutron-removal cross sections in which a strong correlation can be seen. The statistical error from the measured charge-changing cross section at 800 AMeV with a 2 g/cm^2 target has been added to one of the data points in the blue box. While this specific scenario shows $\Delta\sigma_{\Delta N}$ to be below the required ≈10 mb, this is not always the case. All experimental runs with target thickness 1 g/cm^2 had $\Delta\sigma_{\Delta N}$ range from 14-20 mb, and thus is already too high. Only at 650 AMeV with a thicker 2 g/cm^2 target was a $\Delta\sigma_{\Delta N}$ of 10 mb reached, and decreased even further to 7 mb at 800 AMeV. It should also be mentioned that this $\Delta\sigma_{\Delta N}$ value does not include any systematic error, so in order for this method to be effective, this must also be kept very low.

With thicker targets, higher beam energy, and low systematic error, it is possible to reach the necessary $\Delta\sigma_{\Delta N} \approx 10$ mb $(\Delta\sigma_{\Delta N}/\sigma_{\Delta N} \approx 2.5$ %) precision required, making this an effective method to constrain L within 30 MeV, and thus, the EOS in neutron-rich matter.

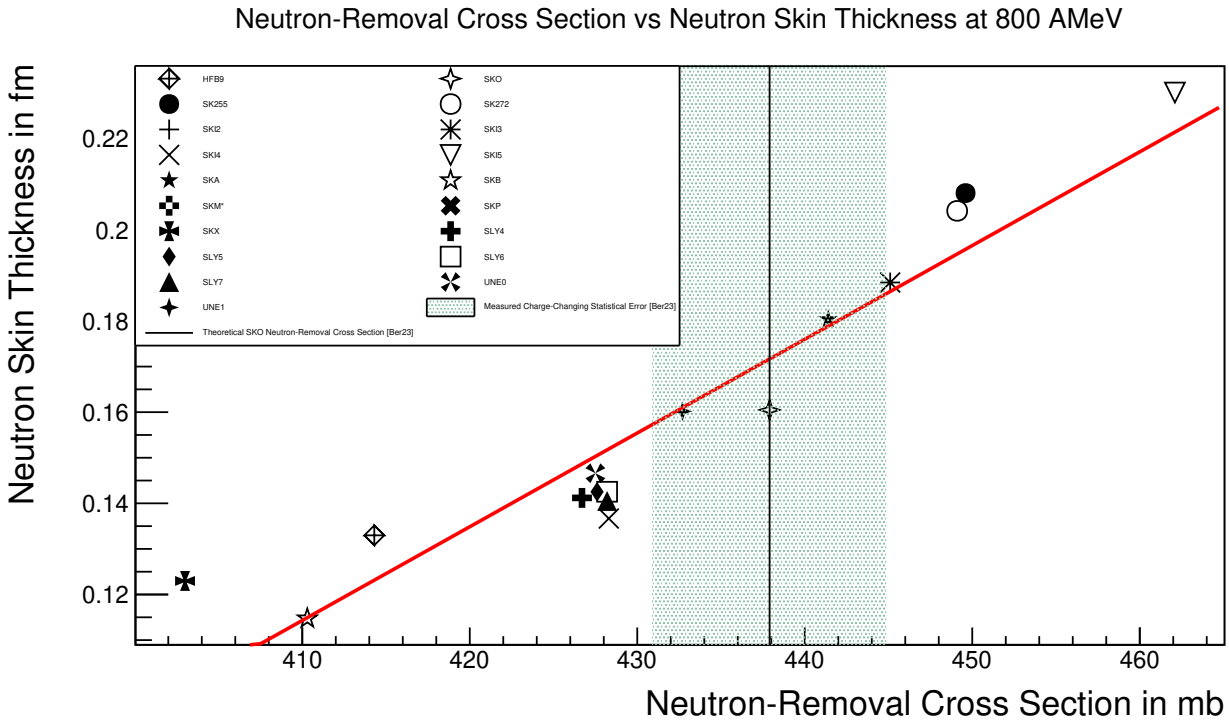

Figure 5.17.: Neutron skin thickness as a function of the theoretical neutron-removal cross sections. The strong correlation is highlighted by the red line. Measured charge-changing cross section error bars from the 800 AMeV run with a 2 g/cm^2 target is highlighted in the blue box.

5.4.4. Future Improvements

It is shown here that the cross section is very sensitive to systematic uncertainties. For future experiments, it is crucial for uncertainties be reduced to the order of $\approx$ 1% in order to determine cross section measurements with better than 2% accuracy. One way that could be considered is a change in the experimental setup. A fragmented beam is preferred to a primary beam as the beam is more spread out and less intense. This allows for a more efficient calibration of the detectors as more area is hit by the beam. It also lowers the intensity that any one part of the detector would experience. This is not always possible, however. If a primary beam must be used, it could also be done that the beam is less intense or also spread out to help with the calibration of the detectors. Another important point is that the read-out of the data from the electronics needs to be understood for a successful analysis. The rate dependence needs to be understood to prevent or fix the spreading out of the signal. The pile-up from the PSPs also affects the shape of the energy peak. This issue can become less with the implementation of tprev and tnext, which the calculation of the time from the previous event (tprev) and the time to the next (tnext) event. Also, it is crucial to accurately measure the distances between the detectors in the experimental setup for the TRACKING stage of

the analysis. Without accurate measurements, the tracking of fragments between the detectors will not be completely accurate and can lead to misidentification. It is also important to set appropriate thresholds for the electronics to ensure the detectors are recording as little noise as possible to allow for the best resolution of the physics data. The detectors used also must be optimized. If no downscaling is used in the experiment, then a detector with a higher charge resolution is necessary. In Fig. 5.18, the Gaussian of Z=50 is represented in red and Z=49 is represented in blue. Due to the amplitude of Z=50 being much higher than that of Z=49, Z=49 blends into Z=50 and is not possible to resolve. In Plot (a) the sigmas are the experimental value, and in Plot (b) the sigma for both peaks has been reduced to the point they can be individually distinguished. The experimental sigma gave a resolution of around 1.1% and it would be necessary to have a resolution of around 0.65% to confidently resolve each peak. To achieve cross section measurements with better than 2% accuracy, it would be necessary to either have a detector with a high enough charge resolution to distinguish between Z=50 and Z=49 or have a lower beam intensity so that both detector and readout are not overloaded and the deadtime effects are under control.

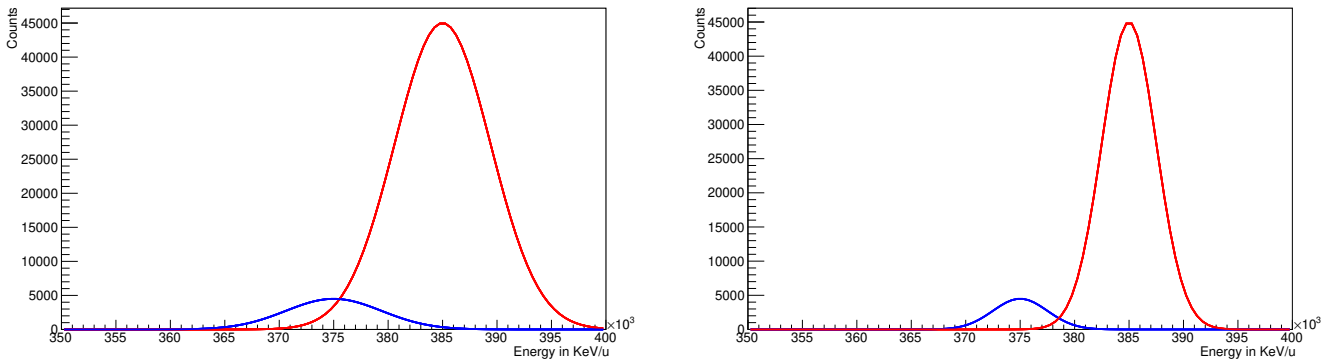

(a) Experimental sigma value of 4400 used for Z=50 and Z=49. Detector resolution is 1.1%.

(b) Sigma value decreased to 2500 for Z=50 and Z=49. Detector resolution would now be 0.65%

Figure 5.18.: Plot (a) Gaussian representations with experimental amplitude, mean, and sigma. Plot (b) is the same, but with an altered sigma to resolve Z=49 and Z=50 clearly.

6. Conclusion

Measurements for the charge-changing and neutron-removal for ^{120}Sn were done at the R^{3}B Setup at GSI Helmholtzzentrum für Schwerionenforschung GmbH in February of 2019. A beam of ^{120}Sn was accelerated at different energies and onto different targets, which can be seen in Tab 6.1. The proposed method of measuring the neutron-removal and charge-changing cross sections was chosen due to many advantages. On the theory side, only inputs from the Glauber Model and density are needed. On the experimental side, the robustness of the method is an advantage, as the analysis is only looking for the surviving particles (apart from the collective contribution). The charge-changing cross section is in particular advantageous to study since charge radii are so well known. This allows the input of measured, quantitative values to test the Glauber model with. Also, GSI is uniquely suited for the beam energies and setup needed for this experiment.

Energy (AMeV)	**C 1 g/cm^2**	**C 2 g/cm^2**	**C 4 g/cm^2**	**CH_2 1.2 g/cm^2**	**CH_2 2.3 g/cm^2**	**Pb**	**Empty**
400	X			X			X
550	X	X		X	X		X
650	X	X	X	X			X
800	X	X	X	X	X	X	X
900		X	X		X		

Table 6.1.: All of incoming beam energies used during this experimental campaign with an X indicating if a certain target was used during that energy. The plastic CH and Pb targets were not used in the present analysis.

The measurement of the charge-changing cross section for ^{120}Sn is discussed in the present work. Various Glauber model calculations done by Carlos Bertulani [Ber23] are provided for the theoretical framework for probing different interaction models. The measured cross section values were roughly 20% lower than the theoretical calculations. Comparison to theory is therefore not possible in this state and no conclusion can be made for the reaction model from these values.

The statistical and systematic errors from the use of a ”simpler” equation are found to be above limit of 2%. However, there was additional uncontrollable uncertainty from the fluctuation in the beam rate. This flux created an error in the response of the electronics. Specifically, the PSP detectors

used to extract the yield of charged particles before and after the target were found to have issues in the readout electronics. A rate dependence was found to have an effect on the readout system from 100 Hz, and this experiment was running above 1 KHz. The effect caused the areas of the detector receiving intense input, i.e. the beam spot, to produce a non-Gaussian response for the readout energy. The spread of the data from this response also made it difficult to make a clear distinction between $Z = 50$ and $Z = 49$ particles. This had a large impact on the analysis of the data as the area of interest was the beam spot and how many unreacted particles survived. The different beam rates had an observed fluctuation of deduced yields for unreacted particles of about 20% and resulted in a systematic shift to the calculated charge-changing cross sections. Therefore, obtaining an accurate yield of unreacted particles within the desired precision was not possible. It is necessary to study the readout electronics further before using these detectors again at high beam rates.

A. Fiber Energy Loss

Analysis on the energy loss from the fiber detectors lead to some questionable discoveries. The energy loss across different fiber detectors was investigated and it was discovered that there is no correlation between the energies, as can be seen in Fig. A.1. It was uncertain if this was coming from an issue during the unpacking stages or if this came from the detector itself. The raw data was then investigated from the ucsebs level before any calibration procedure occurs, and the same non-correlation effects were seen, as can be seen in Fig. A.2.

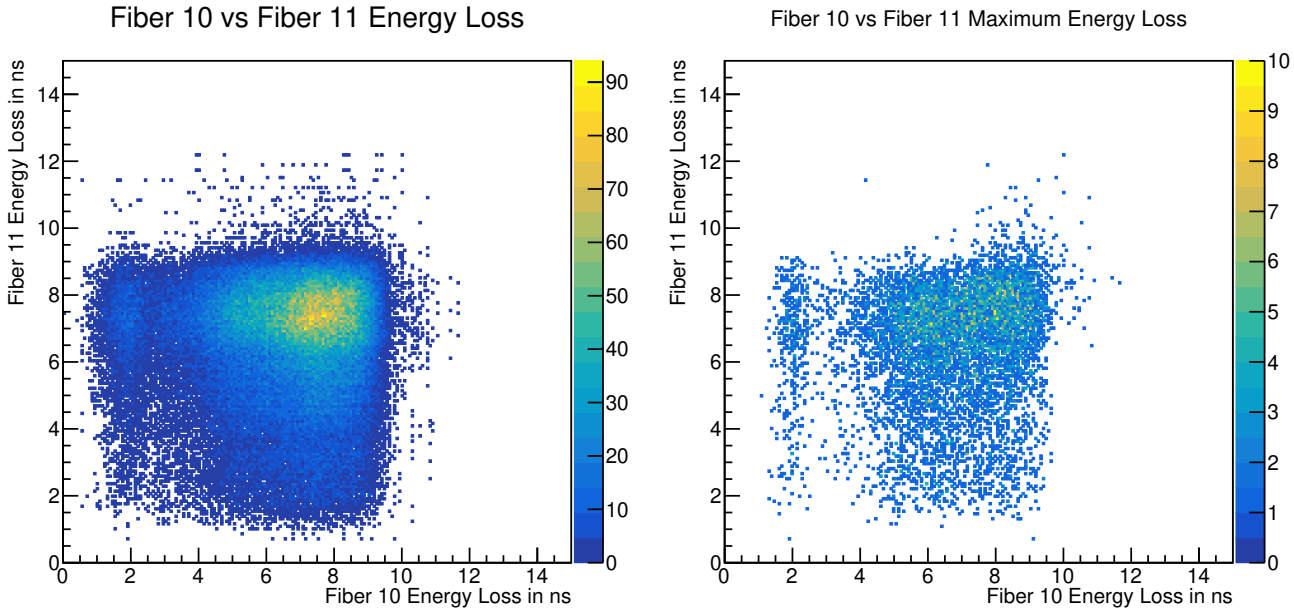

Figure A.1.: LEFT: Energy loss in Fiber 10 vs Fiber 11 and RIGHT: Maximum energy loss in Fiber 10 vs Fiber 11. No Correlation can be seen between the energies from the two different energy detectors. There is a limit to the data around 10 ns.

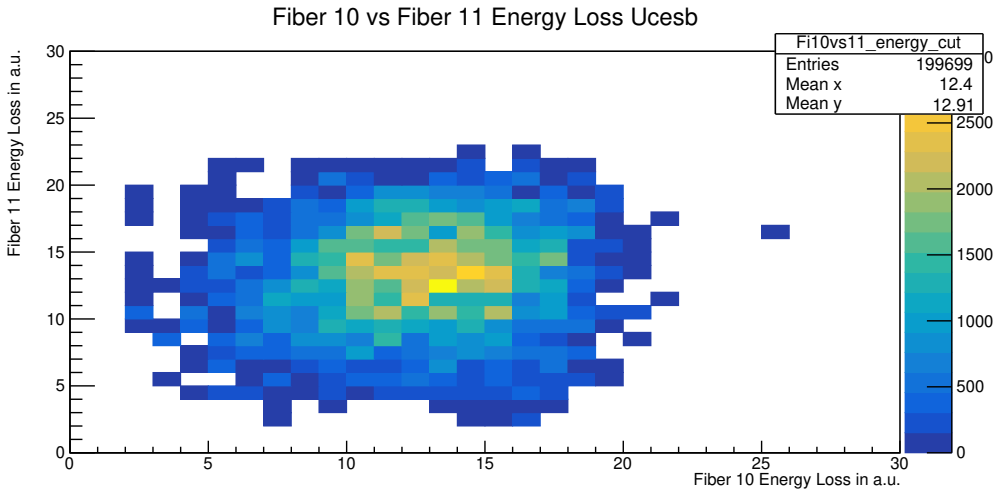

Figure A.2.: Energy loss in Fiber 10 vs Fiber 11 from the ucesb level. Still no correlation can be seen between the energies in the different detectors, showing that the energy loss data was never correlated.

The energy loss also seemed to have a hard cut at roughly 10 ns. Also, when the energy loss is plotted against the fiber number, it is difficult to see the distinction between the energy of the real events and the noise from the detectors, as can be seen in Fig. A.3. Without this clear divide, it is difficult to know if the data being analyzed is the real physics event or just noise from the detector.

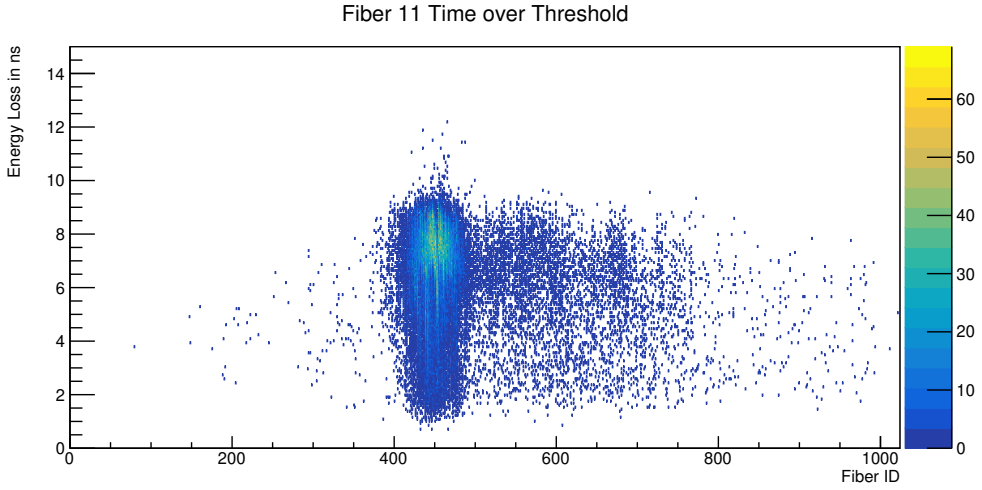

Figure A.3.: Time over threshold for Fiber 11. A difference between the energy recorded as noise and real energy should be easily discernible but is not, making it difficult to cut away the data that is not needed for anaylsis.

To try and make these plots a bit simpler, they were attempted with only the maximum energy event. However, the maximum energy hit for each event was not clear. As can be seen in Fig. A.4, in the left plot there is one very clear there is one maximum energy result. However, in the right plot there are at least 3 events that have a similar energy that could be considered the maximum energy event. Because of this, it is not clear which event is the real event. More investigation is needed to understand what the data is showing before the data from the fibers can be used for analysis.

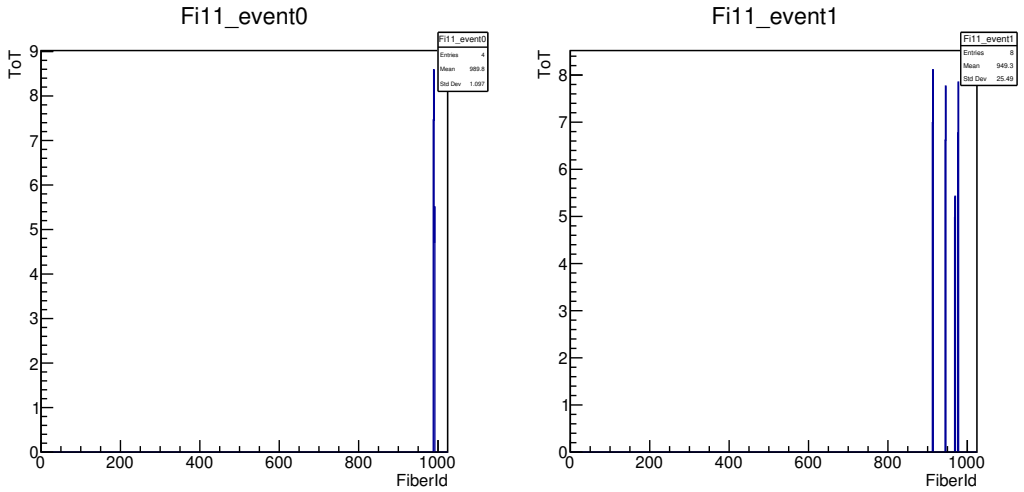

Figure A.4.: LEFT: The hits in event zero for Fiber 11. One clear peak is seen, making the maximum energy easy to distinguish. RIGHT: The hits in event 1 for Fiber 11. Multiple peaks with large energy can be seen, making the maximum energy and real maximum energy event unclear and therefore difficult to analyze.

B. Different Analysis Methods

The analysis for the charge-changing cross section presented multiple problems. The response functions of the PSPs were not understood until recently. The TOFD calibration presented unforeseen issues that delayed the completed calibration. The final method used is described in Ch. 5.2.2. The methods attempted prior to the final method are described below.

B.1. Alternative Analysis using the PSPs

PSP2 was not used for the incoming value as it presented challenges for a clean analysis. Analysis of the energy from the PSPs was conducted two ways: either by combining the energy from the front and back of each detector into one energy or using just the energy from the front or back. PSP2 had been used in a previous experiment, and therefore had radiation damage. While an energy peak can clearly be seen, it is difficult to get an accurate fit as there is a large shoulder connected to the peak as the energy value increases, which can be seen in Fig. B.1.

Radiation damage is not the only possible reason for the shoulder. The PSP's also experience pileup, which is when two events happen before the trigger window closes and the energies are summed together. There are a non-negligible amount of these events that contribute to the tail after the peak from the beam spot. Pileup will be discussed in more detail in the following sections.

The first attempts at extracting the number of incoming and unreacted particles was done by using both LOS and PSP2 for the incoming and both PSP4 and PSP6 for the unreacted. Due to the non-elliptical shape of the beam, getting an accurate 2D cut on the beam spot presented challenges. As can be seen in Fig. B.2, there is a very prominent ellipse in the center, but much of the beam spot is also above this ellipse and also needs to be taken into account to have the accurate number of incoming. For the unreacted, the beam spot seems to be a bit more circular, as can be seen in Fig. B.3, and is therefore easier to cut on. However, the vertical and horizontal lines coming off the beam spot are non-negligible amounts of potentially unreacted beam that do not get accounted for

with this cut. For these reasons, the 2D cut method was abandoned in favor of using the integral divided by bin width from a Gaussian fit on a 1D plot.

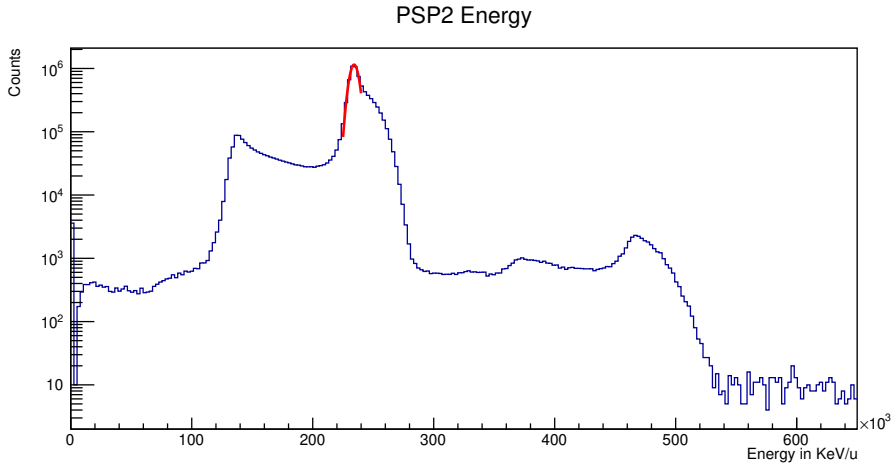

Figure B.1.: PSP2 energy spectrum. There is a noticeable peak in the energy just right of the peak that comes from radiation damage and pileup. Energy to the left comes from the readout of the electronics. Due to the tail and the shoulder, the peak is not Gaussian and difficult to apply a clean fit.

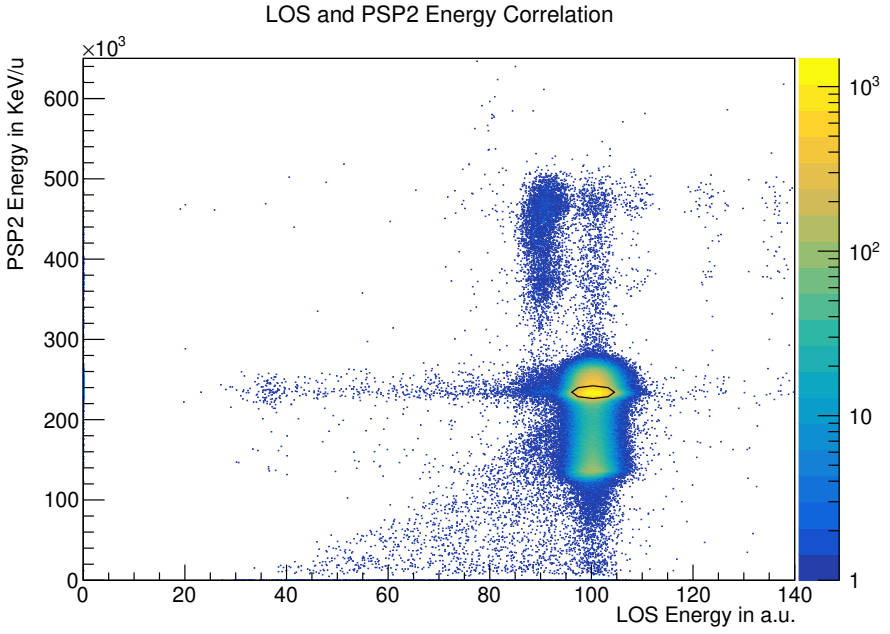

Figure B.2.: The correlated energies for LOS and PSP2 with the black ellipse representing a 2 sigma cut around the beam spot for each detector. It was later understood that this cut did not work because the bright arm below the beam spot should also be included in the count for the unreacted.

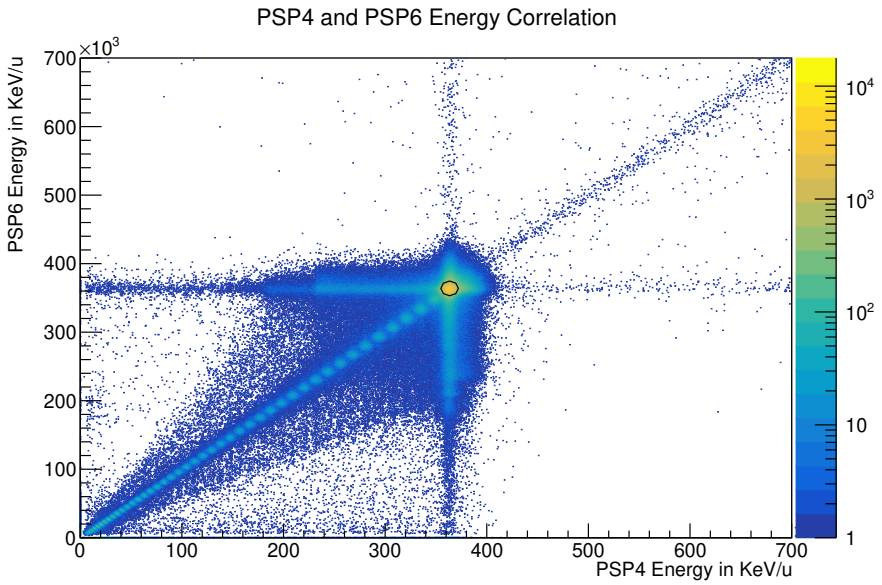

Figure B.3.: The correlated energies for PSP4 and PSP6 with the black ellipse representing a 2 sigma cut around the beam spot for each detector. It was later understood that this cut did not work because the bright arms coming from the beam spot in each detector should also be included in the count for the unreacted.

Investigations were then done into trying to reduce the low energy tail from the PSPs. An ”addback” procedure was attempted, where the total energy loss was calculated by adding energy deposits in neighboring strips together. Unfortunately, this did not yield the expected result; most events were shifted above the main energy peak, while the low energy tail was not reduced significantly, as can be seen in Fig. B.4. Again, this was determined to come from the response function of the electronics later.

An investigation into pileup in the PSPs was conducted to understand if this was influencing the cross sections. First, the energy loss value in the PSPs was analyzed in relation to to the time difference of all hits in the Mapped level of LOS. While the spectra did confirm pileup, a cut on the time difference did significantly reduce the shoulder. The information on how variables are defined and the mapping of the electronics are all found in so-called ”samplers”. So, the next step was to modify the sampler mapping at the ucesb level to include a second sampler that would allow access to the master start time in order to correlate hits from LOS. From this, variables that allow the calculation of the time from the previous event (tprev) and time to the next event (tnext) can be created, which would allow for the pileup to be cut away. This is still in progress.

It was also discovered there is no correlation between LOS and PSP hit multiplicity. With this knowledge, the next step was investigating multiple hits in the different strips and it was discovered

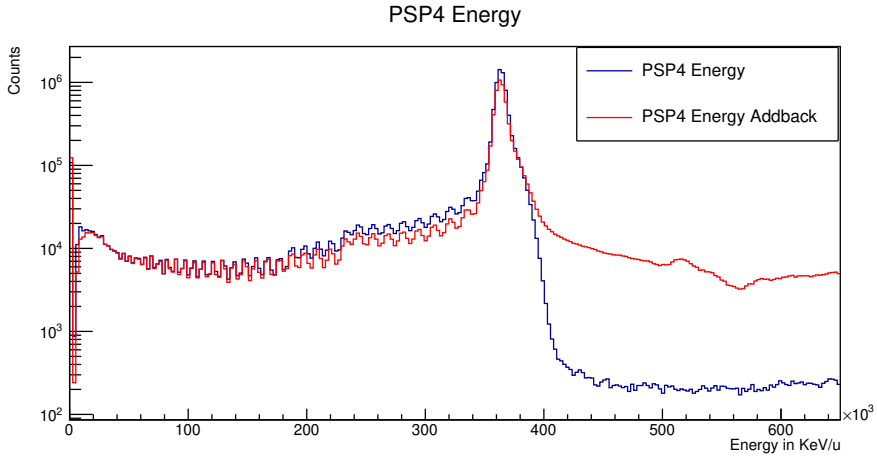

Figure B.4.: (Left) The energy for the front of PSP4 and (Right) the energy for the back of PSP4. The overlapping graphs show the maximum energy of each detector (blue) and the energy addback (red). It can be seen that the largest addback difference occurs at energies higher than the main peak and does not significantly reduce the lower energy tail.

that 15% of events have multiple hits at high energy in different strips. These issues were also found at the uscebs level, so it cannot be that it is a problem coming from the unpack stages of analysis.

The current status of the analysis using the PSPs is that there is certainly pileup in the detectors, but not as much as one might first think looking at the data. The discovery of the issues with the response function of the electronics allowed the use of the final method described in Ch. 5.2.2. Investigations to better understand pileup and the response function are still ongoing.

B.1.1. Alternative Analysis using the TOFD

The TOFD was the last detector of the s473 setup and was comprised of 4 separate planes. Since the TOFD experiences the most energy loss being last, it is less ideal to use for the charge-changing cross section. The cross sections were also calculated using TOFD data as a way to investigate systematics. The energy loss for the each individual plane of TOFD can been seen in Fig. B.5. The TOFD has to be calibrated very carefully, otherwise the resolution of the peaks is not enough to discern between the the beam, Z=50, and the fragments, Z=49 and 48, and therefore will not extract a completely unreacted value.

In order to extract an accurate value for the unreacted particles in the TOFD, it must be calibrated very precisely. The 4 different planes must also be calibrated separately as the particles will experience energy loss as it travels through the detector. The first attempts to extract an unreacted value from the TOFD were done using all 4 planes together.

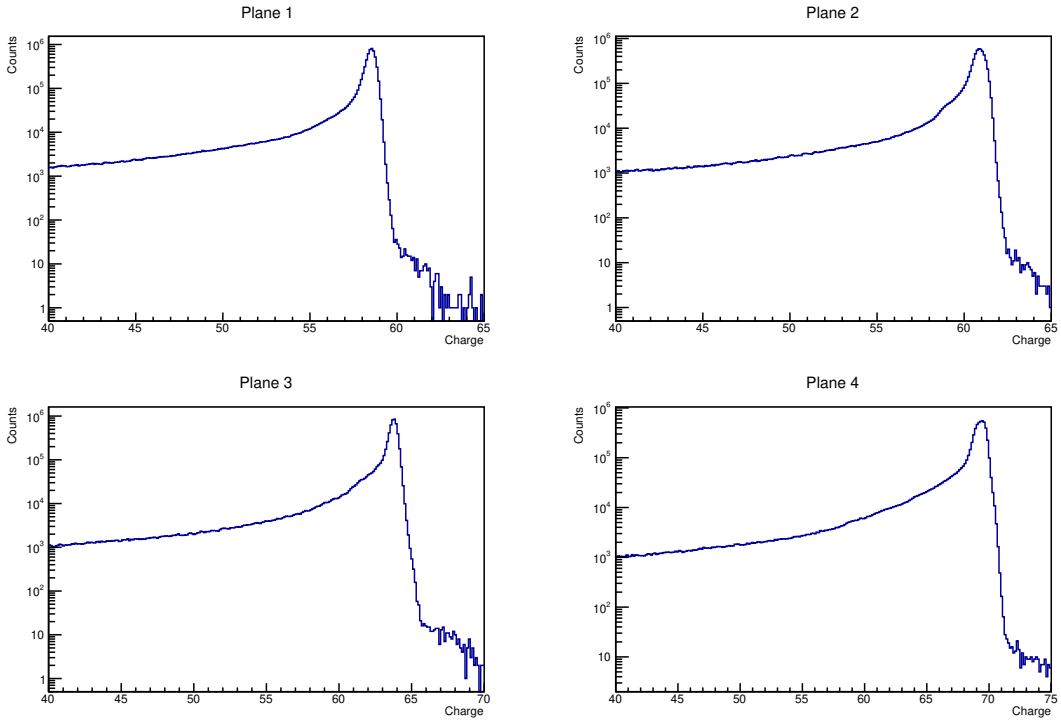

Figure B.5.: The energy spectrum for each individual plane of the TOFD with (Top Left) Plane 1, (Top Right) Plane 2, (Bottom Left) Plane 3, and (Bottom Right) Plane 4. It can be seen that the charge of the main peak moves to a lower value as the particle moves through the detector. It can also be seen that the main peak is not a uniform Gaussian because the resolution is not high enough to distinguish between the different fragments. Corrections to the calibration are ongoing to place all peaks at a charge of Z=50 and to improve the energy resolution.

This method discovered the energy loss peaks from each plane to be in different locations, as can be seen in Fig. B.5. The calibration is still ongoing for the energy loss using the time difference as the particles travel through the detector. Analysis was then continued using only one plane of the TOFD, plane 1 as it was the first plane hit. By looking at only one plane, there is clearly only one peak visible to place a Gaussian fit on, as can been seen in Fig. B.5. However, the resolution of the energy loss at the hit level is not high enough to distinguish between every isotope, i.e. the peak for Z=50 also may include fragments with Z=49 and Z=48. This also makes the peak a non-Gaussian shape and therefore challenging to fit. A method using a triple Gaussian peak was attempted.

As can be seen in Fig. B.6, there are fits to three peaks that bleed into the main unreacted peak. With this method, one can cut on only the Gaussian that fits the main peak to extract a number for the unreacted. Unfortunately due to the nature of how the cross section is calculated, very accurate values, meaning uncertainties need to be reduced to ≈1%, need to be extracted from the data. The TOFD calibration is ongoing to increase the resolution to achieve the accuracy needed.

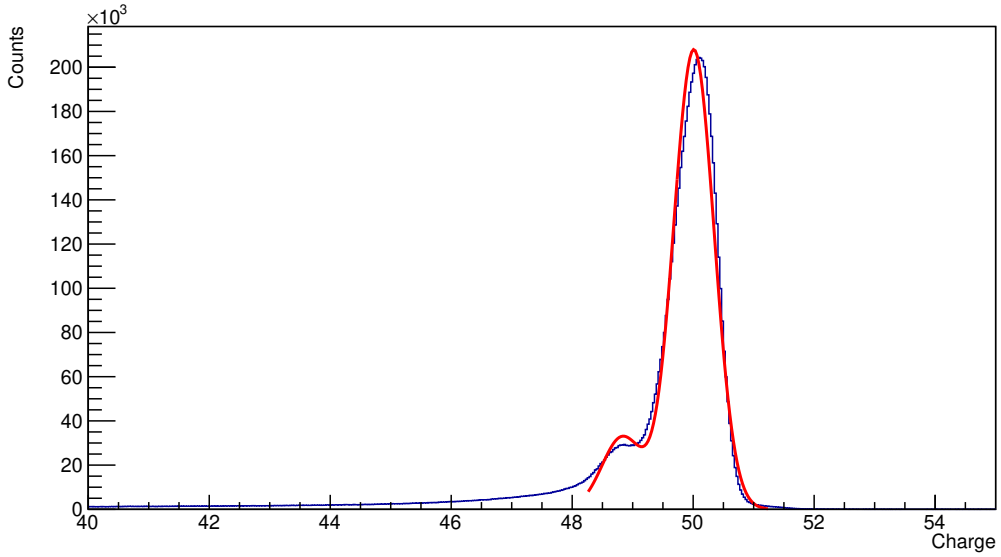

Figure B.6.: The energy resolution of the TOFD here is not high enough to distinguish between $Z = 48 - 50$, so three Gaussian's are fit onto the main peak. Once fit, the peak on Z=50 can be gated on to extract only the unreacted particles.

B.1.2. Alternative Analysis using Position Dependence

One final method to extract an accurate unreacted value was attempted by placing a cut on the incoming beam based on position of the beam spot. Due to high reaction probabilities in the TOFD, there was a possibility of a foreign object obstructing the path of the beam. To conclude if this was the case, 2D cuts were made on the position of the beam spot in the same way as described in Sec. B.1. Different size cuts were made to restrict which position of the beam made it to the TOFD, and then the reaction probabilities and cross sections were calculated again. The cross sections calculated from the extracted values did not change depending on the size of the cut on the beam spot, so it can be concluded there was not a foreign object obstructing the beam line.

List of Tables

List of Figures

Bibliography

[Abb+17] B. Abbott et al. “GW170817: observation of gravitational waves from a binary neutron star inspiral”. In: *Physical review letters* 119.16 (2017), p. 161101.

[Abr+12] S. Abrahamyan et al. “Measurement of the neutron radius of Pb 208 through parity violation in electron scattering”. In: *Physical review letters* 108.11 (2012), p. 112502.

[Abu+08] B. Abu-Ibrahim et al. “Reaction cross sections of carbon isotopes incident on a proton”. In: *Physical Review C* 77.3 (2008), p. 034607.

[Adr+05] P. Adrich et al. “Evidence for Pygmy and Giant Dipole Resonances in Sn 130 and Sn 132”. In: *Physical review letters* 95.13 (2005), p. 132501.

[Alv+14] H. Alvarez-Pol et al. “Performance analysis for the CALIFA Barrel calorimeter of the R3B experiment”. In: *Nuclear Instruments and Methods in Physics Research Section A: Accelerators, Spectrometers, Detectors and Associated Equipment* 767 (2014), pp. 453–466.

[AM13] I. Angeli and K. Marinova. “Table of experimental nuclear ground state charge radii: An update”. In: *Atomic Data and Nuclear Data Tables* 99.1 (2013), pp. 69–95.

[AHS24] P Arthuis, K Hebeler, and A Schwenk. “Neutron-rich nuclei and neutron skins from chiral low-resolution interactions”. In: *arXiv preprint arXiv:2401.06675* (2024).

[ATI] ATIMA. *ATIMA GSI*. `http://web-docs.gsi.de/~weick/atima/`. Accessed: 2023-08-02.

[Aum19] T. Aumann. “Low-energy dipole response of exotic nuclei”. In: *The European Physical Journal A* 55.12 (2019), pp. 1–14.

[AN13] T. Aumann and T. Nakamura. “The electric dipole response of exotic nuclei”. In: *Physica Scripta* 2013.T152 (2013), p. 014012.

[Aum+17] T. Aumann et al. “Peeling off neutron skins from neutron-rich nuclei: Constraints on the symmetry energy from neutron-removal cross sections”. In: *Physical review letters* 119.26 (2017), p. 262501.

[Bat+89] C. J. Batty et al. “Experimental methods for studying nuclear density distributions”. In: *Advances in Nuclear Physics*. Springer, 1989, pp. 1–188.

[BHR03] M. Bender, P. Heenen, and P. G. Reinhard. “Self-consistent mean-field models for nuclear structure”. In: *Reviews of Modern Physics* 75.1 (2003), p. 121.

[Ber11] D. Bertini. “R3BRoot, simulation and analysis framework for the R3B experiment at FAIR”. In: *Journal of Physics: Conference Series*. Vol. 331. 3. IOP Publishing. 2011, p. 032036.

[Ber+08] Denis Bertini et al. “The FAIR simulation and analysis framework”. In: *Journal of Physics: Conference Series*. Vol. 119. 3. IOP Publishing. 2008, p. 032011.

[Ber23] C. Bertulani. Private Communication. Jan. 2023.

[BB88] C. Bertulani and G. Baur. “Electromagnetic processes in relativistic heavy ion collisions”. In: *Physics Reports* 163.5-6 (1988), pp. 299–408.

[BD19] C. Bertulani and P. Danielewicz. *Introduction to nuclear reactions*. CRC Press, 2019.

[Bin+14] S. Binder et al. “Ab initio path to heavy nuclei”. In: *Physics Letters B* 736 (2014), pp. 119–123.

[Bor+21] K. Boretzky et al. “NeuLAND: The high-resolution neutron time-of-flight spectrometer for R3B at FAIR”. In: *Nuclear Instruments and Methods in Physics Research Section A: Accelerators, Spectrometers, Detectors and Associated Equipment* 1014 (2021), p. 165701.

[Bro00] A. Brown. “Neutron radii in nuclei and the neutron equation of state”. In: *Physical review letters* 85.25 (2000), p. 5296.

[Bro17] A. Brown. “Mirror charge radii and the neutron equation of state”. In: *Physical review letters* 119.12 (2017), p. 122502.

[Cab+20] P. Cabanelas et al. “Commissioning of the CALIFA Barrel Calorimeter of the R3B Experiment at FAIR”. In: *Journal of Physics: Conference Series*. Vol. 1667. 1. IOP Publishing. 2020, p. 012006.

[Cio+14] M. Ciobanu et al. “PADI, an ultrafast preamplifier-discriminator ASIC for time-of-flight measurements”. In: *IEEE Transactions on nuclear science* 61.2 (2014), pp. 1015–1023.

[CKH03] B. C. Clark, L. J. Kerr, and S. Hama. “Neutron densities from a global analysis of medium-energy proton-nucleus elastic scattering”. In: *Physical Review C* 67.5 (2003), p. 054605.

[DDD87] H. De Vries, C. W. De Jager, and C. De Vries. “Nuclear charge-density-distribution parameters from elastic electron scattering”. In: *Atomic data and nuclear data tables* 36.3 (1987), pp. 495–536.

[DG80] J. Dechargé and D. Gogny. “Hartree-Fock-Bogolyubov calculations with the D 1 effective interaction on spherical nuclei”. In: *Physical Review C* 21.4 (1980), p. 1568.

[dra] drasi. *R3B Acquisition and Detector Controls Group*. R3BAcquisitionandDetector-ControlsGroup.

[Dut+14] M. Dutra et al. “Relativistic mean-field hadronic models under nuclear matter constraints”. In: *Physical Review C* 90.5 (2014), p. 055203.

[feb] febex. *FebexSoftware Homepage*. https://www.gsi.de/en/work/research/experiment_electronics/data_processing/embedded_software/febexsoftware.

[Gan+14] S. Gandolfi et al. “The equation of state of neutron matter, symmetry energy and neutron star structure”. In: *The European Physical Journal A* 50 (2014), pp. 1–11.

[Gla59] R. J. Glauber. *Lectures in Theoretical Physics, Vol 1*. 1959.

[Gre+20] SK Greif et al. “Equation of state constraints from nuclear physics, neutron star masses, and future moment of inertia measurements”. In: *The Astrophysical Journal* 901.2 (2020), p. 155.

[Gro12] K. Grosse. *GSI Scientific Report 2012*. GSI, 2012.

[GSI] GSI. *GSI Helmholtzzentrum für Schwerionenforschung*. https://www.gsi.de/work/forschung/nustarenna/nustarenna_divisions/kernreaktionen/r3b_project_group/glad?no_cache=1. Accessed: 2022-06-30.

[HPY07] P. Haensel, A. Potekhin, and D. Yakovlev. *Neutron Stars 1*. Springer, 2007.

[HJ87] P. Hansen and B. Jonson. “The neutron halo of extremely neutron-rich nuclei”. In: *EPL (Europhysics Letters)* 4.4 (1987), p. 409.

[HJS49] O. Haxel, J. Jensen, and H. Suess. “On the” magic numbers” in nuclear structure”. In: *Physical Review* 75.11 (1949), p. 1766.

[HS10] K Hebeler and A Schwenk. “Chiral three-nucleon forces and neutron matter”. In: *Physical Review C* 82.1 (2010), p. 014314.

[Heb+13] K. Hebeler et al. “Equation of state and neutron star properties constrained by nuclear physics and observation”. In: *The Astrophysical Journal* 773.1 (2013), p. 11.

[Hei+22] M. Heil et al. “A new Time-of-flight detector for the R^3B setup”. In: *The European Physical Journal A* 58.12 (2022), pp. 1–19.

[Hor+07] W. Horiuchi et al. “Systematic analysis of reaction cross sections of carbon isotopes”. In: *Physical Review C* 75.4 (2007), p. 044607.

[Hor19] A. Horvat. “Evolution of the Dipole Response for Neutron-Rich Tin Isotopes 124Sn to 132Sn”. PhD thesis. 2019.

[HRB91] M. Hussein, R. A. Rego, and C. Bertulani. “Microscopic theory of the total reaction cross section and application to stable and exotic nuclei”. In: *Physics Reports* 201.5 (1991), pp. 279–334.

[Kan+16] R. Kanungo et al. “Proton Distribution Radii of C 12–19 Illuminate Features of Neutron Halos”. In: *Physical Review Letters* 117.10 (2016), p. 102501.

[Kli+07] A. Klimkiewicz et al. “Nuclear symmetry energy and neutron skins derived from pygmy dipole resonances”. In: *Physical Review C* 76.5 (2007), p. 051603.

[KSF97] S. Koranda, N. Stergioulas, and J. Friedman. “Upper limits set by causality on the rotation and mass of uniformly rotating relativistic stars”. In: *The Astrophysical Journal* 488.2 (1997), p. 799.

[KH88] K. Krane and D. Halliday. *Introductory nuclear physics*. Vol. 465. Wiley New York, 1988.

[Kra94] A. Krasnahorkay. “Excitation of the isovector GDR by inelastic {alpha}-scattering and the neutron skin of nuclei”. In: (1994).

[Lat12] J. Lattimer. “The nuclear equation of state and neutron star masses”. In: *Annual Review of Nuclear and Particle Science* 62 (2012), pp. 485–515.

[LP04] J. Lattimer and M. Prakash. “The physics of neutron stars”. In: *science* 304.5670 (2004), pp. 536–542.

[LS82] Enrico Lipparini and Sandro Stringari. “Volume and surface symmetry energy coefficients from photoabsorption cross sections”. In: *Physics Letters B* 112.6 (1982), pp. 421–424.

[LT22] W. G. Lynch and M. B. Tsang. “Decoding the density dependence of the nuclear symmetry energy”. In: *Physics Letters B* 830 (2022), p. 137098.

[ME11] Ruprecht Machleidt and David Rodrignez Entem. “Chiral effective field theory and nuclear forces”. In: *Physics Reports* 503.1 (2011), pp. 1–75.

[Mam+] J. Mammei et al. “Proposal to Jefferson Lab PAC 40”. In: *CREX: Parity-violating measurement of the weak charge distribution of 48Ca to 0.02 fm accuracy (unpublished)* ().

[May49] M. G. Mayer. “On closed shells in nuclei. II”. In: *Physical Review* 75.12 (1949), p. 1969.

[MBS] MBS. *Multi-Branch System*. `https://www.gsi.de/work/forschung/experimentelektronik/datenverarbeitung/datenerfassung/mbs`. Accessed: 2023-30-01.

[MNN90] W. D. Meyers, J. M. Nitschke, and E. B. Norman. *Proceedings of the First International Conference on Radioactive Nuclear Beams*. World Scientific Pub Co Inc, 1990.

[Mic15] Micron. *Micron Semiconductor Ltd. Design X5 PSD E/PSD E readout across the strip length, 3D Assembly.* Technical drawing A-4381 and A-4382 provided by the manufacturer together with the detector. 2015.

[NND] NNDC. *National Nuclear Data Center*. `https://www.nndc.bnl.gov/`. Accessed: 2022-08-15.

[OS21] A. Obertelli and H. Sagawa. *Modern Nuclear Physics: From Fundamentals to Frontiers*. Springer Nature, 2021.

[Off+91] E. Offermann et al. "Energy dependence of the form factor for elastic electron scattering from C 12". In: *Physical Review C* 44.3 (1991), p. 1096.

[OYS92] Y. Ogawa, K. Yabana, and Y. Suzuki. "Glauber model analysis of the fragmentation reaction cross sections of 11Li". In: *Nuclear Physics A* 543.4 (1992), pp. 722–750.

[Oza+01] A. Ozawa et al. "Measurements of interaction cross sections for light neutron-rich nuclei at relativistic energies and determination of effective matter radii". In: *Nuclear Physics A* 691.3-4 (2001), pp. 599–617.

[Pin+21] S. V. Pineda et al. "Charge Radius of Neutron-Deficient Ni 54 and Symmetry Energy Constraints Using the Difference in Mirror Pair Charge Radii". In: *Physical Review Letters* 127.18 (2021), p. 182503.

[R3B] R3B. *R3B Homepage*. `https://www.gsi.de/fair/experiments/NUSTAR/R3b.html`.

[Ray79] L. Ray. "Proton-nucleus total cross sections in the intermediate energy range". In: *Physical Review C* 20.5 (1979), p. 1857.

[Ree+21] B. Reed et al. "Implications of PREX-2 on the equation of state of neutron-rich matter". In: *Physical Review Letters* 126.17 (2021), p. 172503.

[Rei89] P. G. Reinhard. "The relativistic mean-field description of nuclei and nuclear dynamics". In: *Reports on Progress in Physics* 52.4 (1989), p. 439.

[Roc+11] X. Roca-Maza et al. "Neutron skin of Pb 208, nuclear symmetry energy, and the parity radius experiment". In: *Physical review letters* 106.25 (2011), p. 252501.

[Roc+13] X. Roca-Maza et al. "Electric dipole polarizability in 208 Pb: Insights from the droplet model". In: *Physical Review C* 88.2 (2013), p. 024316.

[Rod+20] JL Rodríguez-Sánchez et al. "Study of Δ excitations in medium-mass nuclei with peripheral heavy ion charge-exchange reactions". In: *Physics Letters B* 807 (2020), p. 135565.

[ROO] ROOT. *CERN ROOT data analysis framework*. `https://root.cern.ch/`.

[Ros+13] D. Rossi et al. “Measurement of the Dipole Polarizability of the Unstable Neutron-Rich Nucleus Ni 68”. In: *Physical review letters* 111.24 (2013), p. 242503.

[SH15] H. Sagawa and K. Hagino. “Theoretical models for exotic nuclei”. In: *The European Physical Journal A* 51.8 (2015), pp. 1–31.

[Sch17] F. Schindler. “Total reaction, charge-changing, and neutron-removal cross sections of the heavy, neutron-rich nuclei 124Sn, 128Sn, 132Sn, and 134Sn measured with large acceptance at R3B”. PhD thesis. 2017.

[Sch18] S. Scholl. *SiPM readout of fiber detectors with an ASIC based data aquisition system*. 2018.

[SMD19] Z. Sóti, J. Magill, and R. Dreher. “Karlsruhe Nuclide Chart–New 10th edition 2018”. In: *EPJ Nuclear Sciences & Technologies* 5 (2019), p. 6.

[SP16] P. Souder and K. D. Paschke. “Parity violation in electron scattering”. In: *Frontiers of Physics* 11.1 (2016), pp. 1–31.

[Sou+11] P. A. Souder et al. “PREX-II: Precision parity-violating measurement of the neutron skin of lead”. In: *Proposal for Jefferson Lab PAC* 38 (2011).

[SF06] P. Spiller and G. Franchetti. “The FAIR accelerator project at GSI”. In: *Nuclear Instruments and Methods in Physics Research Section A: Accelerators, Spectrometers, Detectors and Associated Equipment* 561.2 (2006), pp. 305–309.

[SR07] J. Stone and P. G. Reinhard. “The Skyrme interaction in finite nuclei and nuclear matter”. In: *Progress in particle and nuclear Physics* 58.2 (2007), pp. 587–657.

[Syn18] I. Syndikus. “Proton-Knockout Reactions from Neutron-Rich N Isotopes at R3B”. PhD thesis. 2018.

[Tak+09] M. Takechi et al. “Reaction cross sections at intermediate energies and Fermi-motion effect”. In: *Physical Review C* 79.6 (2009), p. 061601.

[Tam+11] A. Tamii et al. “Complete electric dipole response and the neutron skin in Pb 208”. In: *Physical review letters* 107.6 (2011), p. 062502.

[Tan+92] I. Tanihata et al. “Revelation of thick neutron skins in nuclei”. In: *Physics Letters B* 289.3-4 (1992), pp. 261–266.

[TDC] TDC. *Clock Time to Digital Converter*. `https://www.gsi.de/en/work/research/experiment_electronics/data_processing/embedded_software/clocktdcsoftware`. Accessed: 2023-02-02.

[TD19] V. Thakur and S. Dhiman. “A study of charge radii and neutron skin thickness near nuclear drip lines”. In: *Nuclear Physics A* 992 (2019), p. 121623.

[TCV08] Luca Trippa, Gianluca Colò, and Enrico Vigezzi. “Giant dipole resonance as a quantitative constraint on the symmetry energy”. In: *Physical Review C* 77.6 (2008), p. 061304.

[Tsa+12] M. B. Tsang et al. “Constraints on the symmetry energy and neutron skins from experiments and theory”. In: *Physical Review C* 86.1 (2012), p. 015803.

[Typ05] S. Typel. “Relativistic model for nuclear matter and atomic nuclei with momentum-dependent self-energies”. In: *Physical Review C* 71.6 (2005), p. 064301.

[Typ14] S. Typel. “Neutron skin thickness of heavy nuclei with α-particle correlations and the slope of the nuclear symmetry energy”. In: *Physical Review C* 89.6 (2014), p. 064321.

[TB01] S. Typel and A. Brown. “Neutron radii and the neutron equation of state in relativistic models”. In: *Physical Review C* 64.2 (2001), p. 027302.

[TW99] S. Typel and HH Wolter. “Relativistic mean field calculations with density-dependent meson-nucleon coupling”. In: *Nuclear Physics A* 656.3-4 (1999), pp. 331–364.

[Typ+10] S. Typel et al. “Composition and thermodynamics of nuclear matter with light clusters”. In: *Physical Review C* 81.1 (2010), p. 015803.

[UCE] UCESB. *unpack and check every single bit*. `http://fy.chalmers.se/~f96hajo/ucesb/`. Accessed: 2023-02-02.

[Ugu+] C. Ugur et al. *A compact readout system for the R3B High-Resolution Neutron Time-of-Flight Spectrometer (NeuLAND)*. `https://repository.gsi.de/record/183946/files/MU-NUSTAR-NR-14.pdf`. Accessed: 2023-02-02.

[VB72] D. Vautherin and D. Brink. “Hartree-Fock calculations with Skyrme’s interaction. I. Spherical nuclei”. In: *Physical Review C* 5.3 (1972), p. 626.

[Wal75] J. Walecka. “Equation of state for neutron matter at finite T in a relativistic mean-field theory”. In: *Physics Letters B* 59.2 (1975), pp. 109–112.

[Wat+16] A. L. Watts et al. “Colloquium: Measuring the neutron star equation of state using x-ray timing”. In: *Reviews of Modern Physics* 88.2 (2016), p. 021001.

[Web05] F. Weber. “Strange quark matter and compact stars”. In: *Progress in Particle and Nuclear Physics* 54.1 (2005), pp. 193–288.

[Yas+18] J Yasuda et al. “Extraction of the Landau-Migdal Parameter from the Gamow-Teller Giant Resonance in Sn 132”. In: *Physical review letters* 121.13 (2018), p. 132501.

[Zen+09] J. Zenihiro et al. “Neutron density distributions of^ 204,206,208 Pb observed via polarized proton elastic scattering”. In: *APS Meeting Abstracts*. Vol. 3. 2009, KC–009.

Acknowledgements

First, I would like to thank my advisor, Prof. Thomas Aumann for allowing me the opportunity to conduct research in his working group. I would also like to thank Prof. Alexandre Obertelli for accepting the position of my second advisor. I also would like thank to Dominic Rossi for being my mentor over the years of my PhD. Thank you for all of the guidance and sharing your expertise with me. I would also like to thank Carlos Bertulani, Achim Schwenk, and Pierre Arthuis for their theoretical inputs.

I want to thank Francesca Luoni, Bernhard Maaß, Andrea Horvat, and Dominic Rossi for reading over all or parts of my thesis and giving me such insightful feedback, and to Martin Baumann for German translations. Also thank you to Andrea Horvat, Johannes Simon, Deša Jelavić Malenica, and the other members of the R^3B Collaboration for their help with the calibration of detectors and analysis in s473.

I would also like to acknowledge the members of my working group. Firstly, my postdoc Andrea Horvat. Thank you for all of your patience with me and always being willing to sit with me until I understood my tasks. I will never forget the long hours working and laughing together, and of course our trips to Köln and Croatia. Also, cannot forget battling the experiments at GSI with Andrea Horvat and Sonja Storck-Dutine. Sonja Storck-Dutine, thank you for becoming my first real friend in Germany and for all of your help over the years, work or otherwise. I could not have asked for a better person to have sit at the desk next to me. I am grateful to Vadim Wagner for all his ”5 minute” fixes to my coding problems, whether it be at work or with the vpn. I would like to thank Hans Törnqvist, Valerii Panin, Matthias Holl, and Junki Tanaka for all of their valuable input to my analysis tools and understanding of electronics. Thank you to my office mates over the years Sonja Storck-Dutine, Vadim Wagner, Eleonora Kudaibergenova, Marco Knösel, and Julian Kahlbow for making being at the office a fun and comfortable experience. To Patrick van Beek for officially inditing me as a Darmstädter with my first Laternchen and always welcoming me into your home. And of course to Philipp Kuchenbrot, Nicolina Lilac, Meytal Duer, Martin Baumann, Michael Mathy, Christopher Lehr, Ina Syndikus, and Sebastian Heil for all the coffee breaks, trips to City Braustüb’l, and game nights over the years.

I would also like to thank my Ars Ludendi teammates for making me feel so welcome in Germany and becoming such close friends despite my lack of German skills. I also want to thank my parents and family for always supporting and pushing me to be the best I can be, even if it involves me moving across the world.

Erklärungen laut Promotionsordnung

§ 8 Abs. 1 lit. c PromO

Ich versichere hiermit, dass die elektronische Version meiner Dissertation mit der schriftlichen Version übereinstimmt.

§ 8 Abs. 1 lit. d PromO

Ich versichere hiermit, dass zu einem vorherigen Zeitpunkt noch keine Promotion versucht wurde. In diesem Fall sind nähere Angaben über Zeitpunkt, Hochschule, Dissertationsthema und Ergebnis dieses Versuchs mitzuteilen.

§ 9 Abs. 1 PromO

Ich versichere hiermit, dass die vorliegende Dissertation selbstständig und nur unter Verwendung der angegebenen Quellen verfasst wurde.

§ 9 Abs. 2 PromO

Die Arbeit hat bisher noch nicht zu Prüfungszwecken gedient.

Darmstadt, 11. April 2023

A. Falduto